Universidad Autónoma de Barcelona

Doctoral Thesis

Design, Development, and Modeling of a Compton Camera Tomographer Based on Room Temperature Solid State Pixel Detector

Author:
Yónatan Calderón

Directors:
Dr. Mokhtar Chmeissani
Dr. Machiel Kolstein

Tutor:
Dr. Pilar Casado

A thesis submitted in fulfilment of the requirements
for the degree of Doctor of Philosophy

in the

Physics Department

March 2014

"If you're going through hell, keep going."

Sir Winston Churchill

Acknowledgements

I would like to thank all the people who contributed to this work and made it possible thanks to their continuous support. In particular to:

- Dr. Mokhtar Chmeissani, my supervisor, for supporting this work and for allowing me to present it in international conferences.
- Dr. Machiel Kolstein, my other supervisor, for his corrections and for suffering from my terrible English.
- Dr. Gianluca de Lorenzo who has done some of the tools needed for the simulations.
- Jose Macias Montero for his support and helpful conversations.
- Gerard Ariño for sharing some of his knowledge on CdTe detectors.

I want to acknowledge all the other members and collaborators of the VIP group who made this work possible: Ekaterina Mikhaylova, Dilber Uzun, Carles Puigdengoles, and Ricardo Martinez. Also my thanks to the European Research Council (ERC) who funded this research through the Seventh Framework Programme (FP7).

Finally I want to thank my family and especially my parents, Andres and Carmen, for their effort and unconditional support. And my very special thanks goes to Patricia who has been at my side in my darkest hour.

Contents

List of Figures

List of Tables

Abbreviations

ET	**E**mission **T**omography
PET	**P**ositron **E**mission **T**omography
SPECT	**S**ingle **P**hoton **E**mission **C**omputerized **T**omography
CT	**C**omputerized **T**omography
PEM	**P**ositron **E**mission **M**ammography
VIP	**V**oxel **I**maging **P**ET
FOV	**F**ield-**O**f-**V**iew
LOR	**L**ine-**O**f-**R**esponse
ROR	**R**egion-**O**f-**R**esponse
LEHS	**L**ow **E**nergy **H**igh **S**ensitivity
LEAP	**L**ow **E**nergy **A**ll **P**urpose
MEAP	**M**edium **E**nergy **A**ll **P**urpose
HEAP	**H**igh **E**nergy **A**ll **P**urpose
PMT	**P**hoto**M**ultiplier **T**ube
UV	**U**ltra **V**iolet
SSD	**S**ilicon **S**trip **D**etector
CZT	**C**admium **Z**inc **T**elluride
FWHM	**F**ull **W**idth **H**alf **M**aximum
DSSSD	**D**oubled **S**ided **S**ilicon **S**trip **D**etector
ASIC	**A**pplication-**S**pecific **I**ntegrated **C**ircuit
PCB	**P**rinted **C**ircuit **B**oard
DAC	**D**igital-to-**A**nalog **C**onverter
ADC	**A**nalog-to-**D**igital **C**onverter
TDC	**T**ime-to-**D**igital **C**onverter
MC	**M**onte **C**arlo

HEP	**H**igh **E**nergy **P**hysics
LHC	**L**arge **H**adron **C**ollider
EEDL	**E**valuated **E**lectrons **D**ata **L**ibrary
EPDL	**E**valuated **P**hotons **D**ata **L**ibrary
FBP	**F**iltered **B**ack **P**rojection
BFP	**B**ack **P**rojection **F**iltering
ART	**A**lgebraic **R**econstruction **T**echnique
OE	**O**rigin **E**nsemble
EM	**E**xpectation **M**aximization
MLEM	**M**aximum **L**ikelihood **E**xpectation **M**aximization
OSEM	**O**rdered **S**ubset **E**xpectation **M**aximization
LM-OSEM	**L**ist **M**ode **O**rdered **S**ubset **E**xpectation **M**aximization
NEMA	**N**ational **E**lectrical **M**anufacturers **A**ssociation
CCP	**C**ompton-**C**ompton-**P**hotoelectric
PSF	**P**oint **S**pread **F**unction
MSE	**M**ean **S**quared **E**rror
DICOM	**D**igital **I**maging and **C**ommunications in **M**edicine

To Azahara who has been at my side in this journey and to my family that has made the journey possible.

Chapter 1

Introduction

Since the discovery of the X-rays in 1895 and their first medical application one year later[1], many different medical imaging techniques have been developed. Emission tomography is a branch of medical imaging that allows the doctors to track physiological processes in the patient. A radioactive compound called radiotracer is injected in the body of the patient. The radiotracer molecule is chosen to fulfill an specific task in the organism allowing to track a concrete physiological process. The two main emission tomography techniques are PET and SPECT.

In PET (Positron Emission Tomography) the injected radiotracer is a positron emitter. The emitted positron annihilates with an electron producing a pair of back-to-back gamma photons. The PET scanner (usually having a cylindrical shape) detects these photons pairs and reconstructs an image of the radiotracer concentration.

In SPECT (Single Photon Emission Computerized Tomography) a single gamma photon is emitted in each radioactive decay of the radiotracer compound. The SPECT system consists of (at least) one gamma camera. A gamma camera is composed by a mechanical collimator and a position sensitive photodetector. The mechanical collimator consists of a thick material with holes that only allow the passing of photons coming from a particular direction. The collimated photons are detected by the photodetector obtaining a projection of the radiotracer in the volume of the patient body. A three dimensional image of the radiotracer concentration in the patient body is obtained from the projections obtained in several directions.

SPECT is the most widely used emission tomography technique because of the large variety of available radiotracers, and the relative low cost when compared with PET. However, SPECT has intrinsic limitations due to the mechanical collimation: low efficiency as only a fraction of the gamma photons can pass through the collimator, an

inverse proportional relationship between the efficiency and the image resolution (the bigger the collimator holes the higher the efficiency but the lower the image resolution), and the camera must be rotated increasing exposure time.

The concept of Compton camera has been proposed[2] in order to overcome those limitations. A Compton camera consists of two detectors, called scatterer and absorber, working in coincidence. In a coincidence event the gamma photon (emitted by the radiotracer) reaches the scatterer and undergoes a Compton interaction, scattering into a certain angle. The scattered gamma reaches the absorber where it undergoes a photoelectric interaction and is absorbed. Using the positions of both interactions and the corresponding deposited energies, one can reconstruct a cone surface which contains the emission point of the gamma photon. With the cones reconstructed from several coincidences, an image of the activity in the patient body can be obtained.

The Compton camera has the potential to overcome all the intrinsic limitations of SPECT as: each gamma has a probability to be scattered and produce a coincidence event, the image resolution is not tied to the efficiency, and it is possible to obtain three dimensional images without moving the camera. However, the complexity of the image reconstruction and the limits in the detector technology have prevented the Compton camera concept to become a viable medical imaging system.

The VIP (Voxel Imaging PET) project proposes a novel detector design based on pixelated solid state (CdTe) technology to overcome the limitations of scintillator detectors used in PET. VIP features a modular design in which the basic element is the detector module unit. The module contains the solid state detectors which are segmented in millimeter size voxels. Thanks to a dedicated read-out chip developed within the project, each one of the voxels is an independent channel for the measurement of energy, position, and time of arrival of the detected gamma photons. The module detectors are stacked in order to form PET sectors. Putting several of these sectors together, leads to a seamless PET ring[3].

Although the VIP module has been designed for PET, the flexibility of the module design allows to explore other possible applications like PEM (Positron Emission Mammography) and Compton camera. In this thesis we will evaluate a Compton camera based on the VIP detector concept. The scattering and the absorber detectors will be made from the stacking of specially designed module units. Silicon will be used as detector material in the scatterer in order to maximize the Compton interaction probability for the incoming gamma photons. In the absorber, CdTe will be used as detector material in order to stop the gamma photons emerging from the scatterer. The excellent energy resolution of the solid state detectors combined with the millimeter size of the detector

voxels, result in a high accuracy in the reconstruction of the Compton cones that cannot be achieved with scintillator crystals.

In this thesis we will use Monte Carlo simulations in order to evaluate and model the proposed Compton camera. Two different image reconstruction algorithms will be used. The simulation will allow us to obtain the optimal geometrical parameters as well as the expected performance of the Compton camera in terms of detection efficiency and image resolution. A smaller FOV (Field-Of-View) prototype will be also evaluated.

Chapter 2

The Working Principles of a Compton Camera

This chapter is an overview of the role of the Compton camera in the medical imaging discipline and it also explains the working principles of such a scanner.

This chapter provides an overview of Single Photon Emission Computerized Tomography (SPECT) and its intrinsic limitations. We explain the concept of electronic collimation and how it can overcome the SPECT limitations. After that, we explain the interactions of gamma photons with matter. Finally, we explain what are the factors that can affect the angular resolution of a Compton camera.

2.1 Single Photon Emission Computerized Tomography

Emission tomography (ET) is a discipline in medical imaging that allows to track physiological processes in the organism. ET allows to gain insight into the functional behavior of the body in contrast with other techniques like X-Ray computed tomography (CT) which principally allows to image the body anatomy.

ET is a technique developed in the 1900s based on the discoveries of the chemist George de Hevesy[1], who stated that radioactive compounds injected in the body behave in the same way as the nonradioactive ones at physiological level. After the early experiments of Hevesy with plants, the idea was applied in the field of medical imaging as a result of the development of radiopharmaceutical compounds.

[1] In 1943 he was awarded the Nobel Prize in Chemistry.

These compounds, usually known as radiotracers, are composed of a molecule (the tracer) in which a radioactive atom (label) is embedded. The tracer molecules are chosen to fulfill a specific task in the organism: allowing to track a specific physiological process. An example of a radiotracer is ^{18}F-fluoredeoxyglucose (^{18}F-FDG) which allows to measure the glucose metabolism. In ^{18}F-FDG the FDG is the tracer molecule, which acts in an analog way to normal glucose, and ^{18}F is the label that allows to infer the FDG concentration and thus the glucose consumption.

FIGURE 2.1: A picture of the Symbia E, a SPECT commercialized by SIEMENS. (http://www.healthcare.siemens.com)

The radiotracers can be divided into two categories: single gamma emitters and positron emitters. These two kind of radiotracers are used respectively in one of the two main emission tomography techniques: Single Photon Emission Computerized Tomography (SPECT) and Positron Emission Tomography (PET). In the case of positron emitters, the positron annihilates with an electron producing a pair of back-to-back gamma photons[2]. The PET scanner (usually having a cylindrical shape) detects those photon pairs and reconstructs an image of the radiotracer density distribution. If both gamma photons are detected, and as they are emitted back-to-back, the origin point of the photons must be in the line connecting the interaction positions of the photons in the detectors. This line is usually called line of response (LOR). The single gamma emitters, on the

[2]The positron tends to lose all its kinetic energy through elastic scattering before the annihilation.

Radiotracer	Half-life	Gamma energies	Application
^{67}Ga citrate	3.26 h	141 keV	Infection or lymphoma detection.
^{111}In capromab pendetide	2.80 h	171 keV, 241 keV	Prostate cancer detection.
^{99m}Tc $TlCl$			Brain lymphoma detection.
^{99m}Tc sestamibi			Myocardial perfusion and parathyroid localization.
^{99m}Tc MDP	6.02 h	141 keV	Metastases or fracture detection.
^{99m}Tc HMPAO			Brain perfusion.
^{99m}Tc RBCs			Liver hemangioma detection.
^{99m}Tc sulfur colloid			Liver or spleen imaging.

TABLE 2.1: Some commonly used radiotracers for SPECT and their applications. Most of the members of the list share the same labeling isotope (^{99m}Tc) but have a different tracer compound. Those radiotracers are metabolized in different ways allowing to track different physiological functions.

other hand, produce a single photon in each decay. The SPECT scanner consists of one or more rotating gamma cameras that obtain a projection of the radiotracer density in each of the steps of their rotation. We will further discuss SPECT below.

Some of the used radio-isotopes in SPECT are ^{99m}Tc, ^{111}In, ^{67}Ga and ^{123}I. The most commonly used labeling isotope in SPECT is ^{99m}Tc as the decay rate and the energy of the emitted gammas are perfect for today gamma cameras, while it can be used to label a wide range of molecules. ^{99m}Tc has a half-life that is long enough to be produced and transported but short enough to be eliminated from the body of the patient in a short period of time. Different tracer molecules have been developed in order to track different physiological processes in the organism (see table 2.1).

The SPECT systems commonly used in today medical practice consist of one or two gamma cameras which rotate around the area of the human body that needs to be scanned. A gamma camera consists of a position sensitive photo-detector and a mechanical collimator. The concept was conceived in 1958 by the scientist Hal Anger at the University of California at Berkeley, and has not undergone substantial modifications since then. The Anger camera concept [4] is still predominantly used in SPECT.

The basic operation of a gamma camera consists of two stages. The gamma photon first passes the mechanical collimator. The collimator is made of a thick and high Z material (thick enough to stop the gamma photons to traverse it) with apertures that only allow gamma photons from a specific direction to pass. If the gamma photon passes the collimator it will enter a position sensitive detector. If the photon is successfully detected its interaction position and the energy deposit of the hit is recorded. With the collected information of a sufficient amount of detected photons a projection of the radiotracer density is obtained. One projection does not give enough information

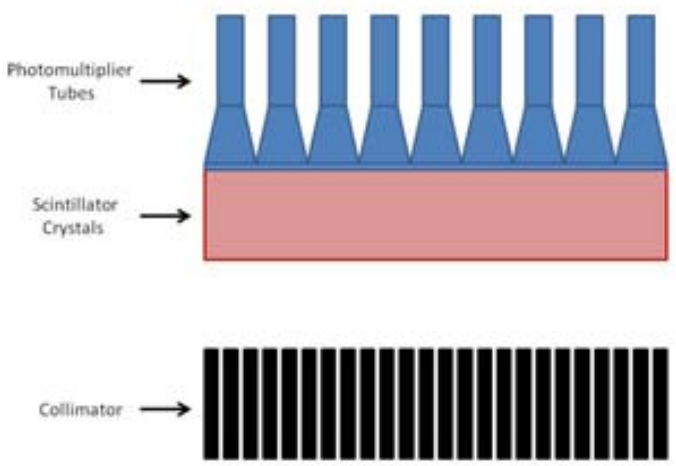

FIGURE 2.2: Schematic representation of a gamma camera based on scintillation crystals.

to reconstruct the radiotracer density in the body, hence the camera (or cameras) is rotated around the patient in order to obtain the tomographic image.

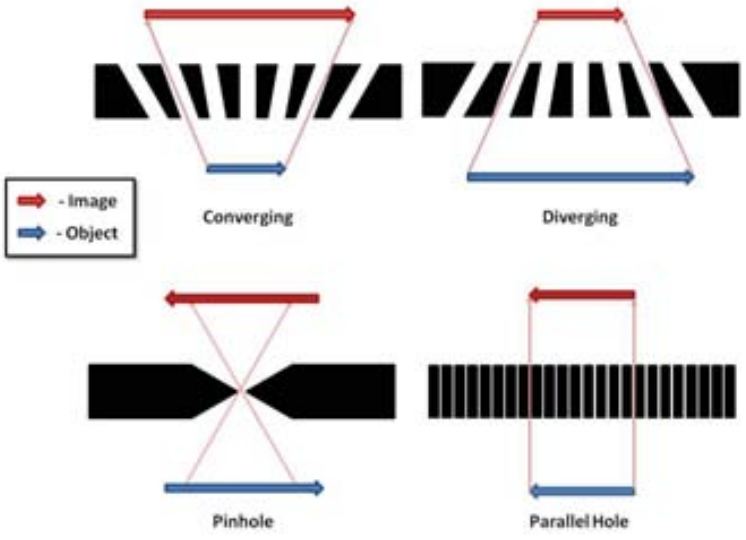

FIGURE 2.3: Schematic representation of four collimator types. Top left and right represent converging and diverging collimators respectively. Bottom left and right represent pinhole and parallel hole collimators.

The energy recorded when the gamma photons are detected is compared to the known original energy of the emitted photons. In this way the photons that undergo an interaction before reaching the detector (with the patient body or the passive camera material) can be rejected as scattered events.

Several types of collimators exist for different applications. One of the most versatile type is the parallel hole collimator. It consists of an array of parallel apertures through a thick material, usually an alloy of lead or more rarely tungsten. The collimator holes can also be different in shape. Hexagonal shape is the most commonly used because is the most efficient for reducing the passive area (but circle, square, and triangle collimators exist). The passive material blocks between the holes are called septa. Ideally only a photon traveling in the hole direction can pass through the collimator. In order to accomplish this the septal thickness between holes must be enough to stop the incoming gamma photon.

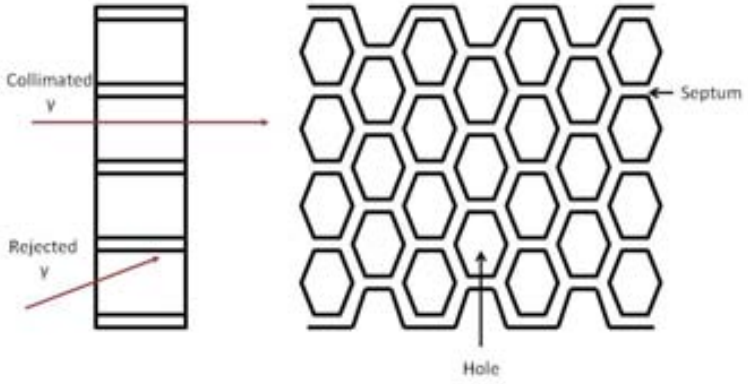

FIGURE 2.4: Schematic representation an hexagonal collimator.

For different gamma photons different alloys and septal thicknesses are used. In medical practice the collimators are classified in five categories depending on the energy of emission of the radiotracer and the trade-off between resolution and efficiency desired. The categories are LEHS (low energy, high sensitivity), LEHR (low energy, high resolution), LEAP (low energy, all purpose), MEAP (medium energy, all purpose), and HEAP (high energy, all purpose). The LE range goes from a few tens up to two hundred keV, ME range goes up to three hundred keV emissions, and HE range is for energies superiors to the three hundred keV.

Depending on the hole length and size the image resolution will change, as the error on the determination of the gamma direction depends on this sizes. As the hole aperture decreases the spatial resolution increases but the detection efficiency is reduced as less gamma photons are able to pass the collimator. As an example, the efficiency achieved by an scintillator based Gamma camera using a LEHS (Low Energy High Sensitivity)

collimator (hole diameter 2.54 mm) is ~ 0.56 cps/kBq, while with a LEHR collimator (hole diameter 1.11 mm) is ~ 0.1 cps/kBq. At the same time, the image resolution achieved with the LEHS is ~ 15.6 mm, while with the LEHR the image resolution is improved to ~ 7.5 mm[3].

The area that is being imaged, known as the Field of View (FOV), is directly proportional to the collimator area in the case of a parallel hole collimator. If the object is too big for the FOV of the camera a diverging hole collimator can be used. With a diverging hole collimator, the holes are not parallel but converge into a focal point, that in this case is behind the detector. With a diverging collimator the image of the object is reduced in size losing resolution but it is possible to reconstruct an image of the entire FOV with a single exposure. Diverging collimators are used for quick full body scans. Alternatively, if the focal point is behind the object then the collimator is called converging collimator. In this case the image is magnified yielding better resolution. The converging collimator are primary used for brain scanning.

The final type of collimation is the pinhole collimator. It consists of a single tiny hole that allows to map each object emission point into a point in the detector, producing an inverted image. The method works on the same principle as a camera obscura. The pinhole collimator is used to image small areas (like the heart). It can achieve high resolution (~ 6.2 mm with a hole diameter of 4 mm) but it has low efficiency (~ 0.05 cps/kBq).

Diverging, converging, and pinhole collimator types introduce distortions in the image that must be corrected during the image reconstruction requiring extra computational resources.

2.1.1 Scintillation Detectors.

The most commonly used detectors in commercially available gamma cameras today are scintillation crystals coupled to photo-multiplier tubes (PMTs). In a scintillation crystal (also called scintillator), some of the energy deposited in the interaction of a gamma photon with the crystal is transformed into visible and UV light. The most commonly used scintillator in SPECT is NaI(Ti) (thallium -doped sodium iodide). NaI(Ti) has an efficient response and a brighter signal than other scintillators in the low energy ranges typical of SPECT. The scintillator can be segmented but most commercial gamma cameras detectors include a single large area crystal.

[3]See http://usa.healthcare.siemens.com/siemens_hwem-hwem_ssxa_websites-context-root/wcm/idc/siemens_hwem-hwem_ssxa_websites-context-root/wcm/idc/groups/public/@us/documents/download/mdaw/nde2/~edisp/reju_spectct_spec_sheet-00304913.pdf

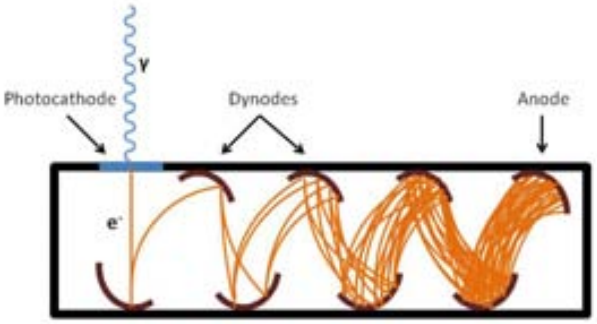

FIGURE 2.5: Schematic representation of a photomultiplier tube.

The scintillator is coupled to an array of PMTs that transforms the light into an electronic signal. The PMTs consist of a vacuum tube containing an anode and a cathode (usually called photocathode). In between the anode and the cathode there are several electrodes called dynodes. The photocathode absorbs 20 to 25 percent of the incoming light. Each time a photon gets absorbed, an atom gets ionized and a free photoelectron gets produced traveling toward the first dynode. This step is very important because if the electron does not reach the first dynode the initiation of the multiplication will not take place. Each time an electron hits a dynode, a secondary electron gets emitted amplifying the signal. The first dynode has the highest voltage in order to collect as many photoelectrons from the cathode as possible. The electrons travel from dynode to dynode growing in number until they reach the anode where the signal is collected.

Typically, the interaction of a gamma photon with a scintillator produces a signal into more than one PMT. The interaction point in the PMTs array is usually computed as the centroid of the PMT signals. The sum of the signal on the PMTs allows to compute the energy deposited by the gamma photon.

SPECT remains the most widely used nuclear medicine imaging technique because of its relative low cost when compared with other techniques like PET and the large amount of different radiotracers available for multiple applications. However, SPECT has intrinsic limitations deriving from the use of mechanical collimation:

- Only a small fraction of the emitted gammas ($\sim 0.02\%$ are detected with a LEAP collimator) can pass through the collimator resulting in an inherently low efficiency.

- The camera spatial resolution is tied with the collimator characteristics yielding an inverse proportional relationship between efficiency and spatial resolution.
- The collimator thickness must be adjusted to the gamma energy as more energetic gammas have increasing penetrating power. Therefore different collimator must be used for different gamma energies.
- The collimator provides one single projection of the source activity. The camera must be rotated to obtain projections from different angles which would increase the exposure time.

The low efficiency and the need to rotate the camera imposes a long acquisition time. This can affect the image quality as the patient will move during the data acquisition (breathing, heartbeat, etc...). The relation between the collimator characteristics, the efficiency, and the spatial resolution, impose a lower limit to the camera performance independently of the detector used. Finally, the fact that different collimators must be used for different energies makes it impossible to perform scans including multiple radiotracers in different energy ranges.

Advances have been made in recent years [5] in order to overcome or decrease these problems. The use of new collimation techniques like the multipinhole collimation[6], the development of new dedicated geometries, the improvements on the hardware and detector technology, and the use of new optimized image reconstruction algorithms, have allowed an increase of the system efficiency maintaining a high image spatial resolution. The use of solid state detectors instead of scintillation crystals improves the energy resolution and allows to reject scattered events more effectively. Iterative image reconstruction algorithms allows to include physical models, attenuation corrections, and detector specific calibrations, into the image reconstruction.

Examples of such developments are the HICAM[7, 8] project and the D-SPECT [9]. HICAM is a project whose purpose is to develop compact and high resolution gamma cameras for medical and research applications. The HICAM follows the same design of a conventional Anger camera but substitutes the PMT tubes by Silicon Strip Detectors (SSD). This allows HICAM to achieve an efficiency of 0.11 cps/kBq and an image spatial resolution of 2.5 mm at a distance of 4 cm. Two prototypes were built with 5×5 cm^2 and 10×10 cm^2 FOV. The D-SPECT features a different design optimized for cardiac imaging. The design is built with 9 detector columns, each one, containing its own collimator and pixelated cadmium zinc telluride (CZT) detector with pixel pitch of 2.5×2.5 mm^2. Thanks to the dedicated geometry, the energy resolution of the CZT detectors, and a specially optimized image reconstruction method, D-SPECT achieves an efficiency of 2.1 cps/kBq and an image spatial resolution of 3.9 mm.

The Compton camera concept has the potential to overcome the limits of SPECT systems. In the next section we will discuss the principles of Compton imaging and the limitations of such technique.

2.2 Principles of Electronic Collimation.

Mechanical collimation imposes intrinsic limitations to the camera performance. Only a small fraction of the emitted gammas can pass through the collimator resulting in an inherently low efficiency. The camera spatial resolution is tied with the collimator characteristics yielding an inverse proportionality relationship between efficiency and spatial resolution. Finally collimator thickness must be adjusted to the gamma energy as more energetic gammas have increasing penetrating power.

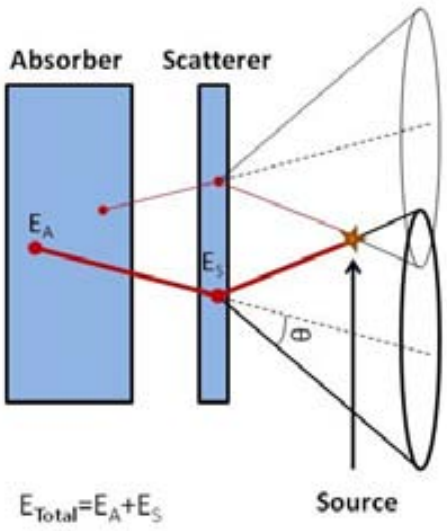

FIGURE 2.6: Schematic representation of electronic collimation. The incoming gamma photon undergoes a Compton interaction in the scatterer and a photoelectric absorption in the absorber. The Compton cone is reconstructed from the deposited energies and the interaction positions.

Electronic collimation was proposed [10] to overcome these limitations. In a Compton gamma camera the collimator is substituted with another photodetector capable to record the interaction position and the deposited energy of an interacting incoming gamma photon. The Compton camera consists of, at least, two detectors working in coincidence. In a coincidence event the gamma undergoes a Compton scattering in the first detector (the scatterer) and gets completely stopped through photoelectric absorption in the second detector (the absorber). Making use of the Compton kinematics one can calculate the scattering angle of the Compton interaction with the following formula:

$$\cos\theta = 1 - m_e c^2 \cdot [\frac{1}{E_\gamma - E_S} - \frac{1}{E_\gamma}]. \tag{2.1}$$

In the above formula θ is the scattering angle, m_e is the electron rest mass, E_γ is the incident gamma energy before the interaction, and E_S is the energy deposited in the scatterer during the interaction.

With the position of both scatterer and absorber interactions and the deposited energies one can reconstruct a cone. The source position is located somewhere on the cone surface. The intersection of the cones calculated from different gammas emitted from the same point gives an indication of the source location.

Electronic collimation has the potential to overcome the intrinsic limitations of SPECT as:

- It yields higher efficiency as every gamma photon reaching the camera has a probability to be scattered producing a coincidence event.
- The camera image resolution is not tied with the efficiency and depends only on the detectors involved.
- Since the Compton camera do not use mechanical collimation it can be used for a wider range of gamma energies and opens the door to imaging with multiple radiotracers with different energies simultaneously.
- The fact that each event is reconstructed as a cone and not as a line allows to reconstruct the 3D activity map directly without the need of moving the camera.

Compton cameras for ET applications come with their own challenges. As far as detector requirements are concerned, Compton imaging is more demanding than SPECT. Both high spatial and energy resolutions are required in order to reconstruct the Compton cone as precisely as possible. The image reconstruction is also challenging and more computationally demanding than for SPECT. Moreover, the physics of the processes involved (Compton scattering and photoelectric absorption) imposes also some limitations on the maximum image resolution that can be obtained (see section 2.2.2). Next generation solid state detectors and more powerful computers for image processing can, for the first time, allow the use of Compton camera in ET.

2.2.1 Interactions of Gamma Photons with Matter.

The coincidence events that the Compton camera aims to record consists of a Compton scattering followed by a photoelectric absorption. In this section we will explore these

two interactions and all the other possible interactions within the energy range of interest for nuclear medicine applications (keV to MeV range).

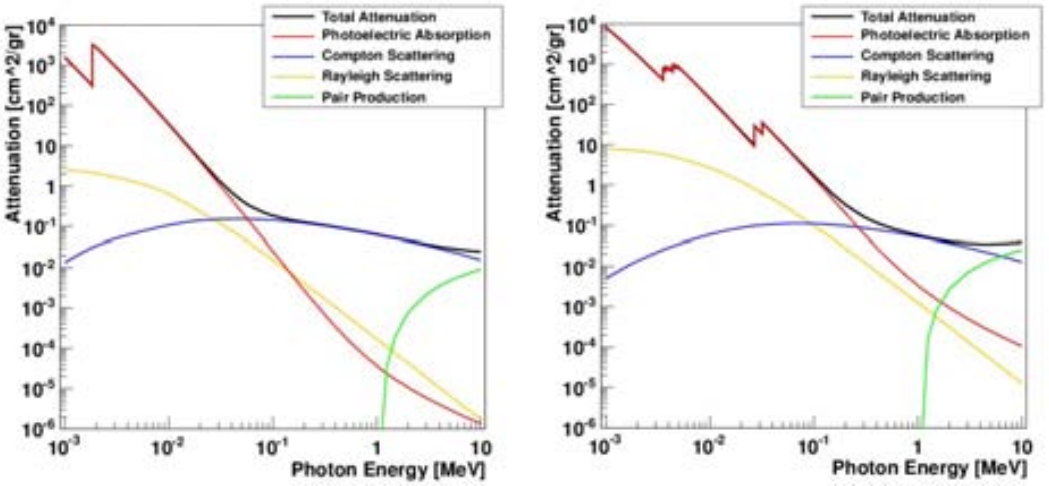

FIGURE 2.7: *Left:* linear attenuation coefficient and its contributions for Si. *Right:* linear attenuation coefficient and its contributions for CdTe. (Data obtained from the NIST XCOM: Photon Cross Sections Database)

The interaction probability of a gamma photon with a given material is characterized by the linear attenuation coefficient which is proportional to the total interaction cross section. If a beam containing I_0 photon is send towards a material of thickness x, the number of photons I that pass through the material is given by the Beer–Lambert law:

$$I = I_0 e^{-\mu x}, \tag{2.2}$$

where μ is the linear attenuation coefficient. The different possible interactions between the material and the photons contribute to the linear attenuation coefficient as the total cross section is just the sum of the cross sections corresponding to the different possible physical processes. In figure 2.7 we show the values of the mass attenuation coefficient (which is equal to the linear attenuation coefficient divided by the material density μ/ρ) in the case of Si and CdTe for different incident photon energies. The predominant interactions for gamma photons with energies up to 1 MeV are the Compton scattering and the photoelectric absorption. Coherent scattering (also known as Rayleigh scattering) is also possible in this energy range but less probable.

2.2.1.1 Compton Scattering.

In Compton scattering the gamma photon interacts with a loosely bound electron. As the energy of the gamma photon is much higher than the energy of the electron, we can

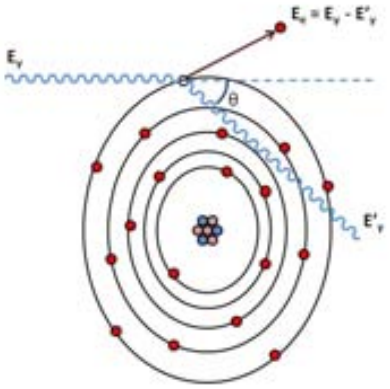

FIGURE 2.8: Schematic representation of the Compton interaction. The gamma photon interacts with a loosely bound electron ionizing the atom and scattering off, with an angle which depends on the energy transfer.

consider the electron as approximately free and at rest. In such conditions, the energy-momentum conservation forbids the photon to transfer all its energy to the electron. Therefore, only a fraction of the gamma photon energy is transferred to the electron which is expelled from the atom while the gamma photon scatters under a certain angle.

Under the approximation that the electron is at rest immediately before the interaction, the energy-momentum conservation establishes the following relation between the scattering angle and the gamma energy:

$$E'_\gamma = \frac{E_\gamma}{1 + \frac{E_\gamma}{m_e c^2}(1 - \cos\theta)}, \tag{2.3}$$

where E'_γ is the gamma photon energy immediately after the interaction. Equation 2.3 relates the scattering angle with the gamma energy and is the base of electronic collimation explained in the previous section.

After the scattering, the electron loses all its energy by interactions with the material. In the case of solid state detectors and ionization chambers this results into the creation of a cloud of electron-hole pairs proportional to the energy of the initial electron and, therefore, proportional to the gamma photon energy loss. These charge carriers move through the material if a bias voltage is applied, and produce a measurable intensity peak with an area proportional to the deposited charge[4].

The energy deposited $E_{Deposited}$ in the detector corresponds to the difference between the incidence gamma photon energy before and after the scattering $E_{Deposited} = E_\gamma - E'_\gamma$.

[4]See section 4.2.1 of chapter 4 for more details of signal processing in solid state detectors.

The possible values of $E_{Deposited}$ ranges from zero to the energy corresponding to a scattering angle of 180°. This maximum value of the deposited energy E_{Edge} is known as Compton edge and can be calculated from (2.3) for $\theta = \pi$ obtaining:

$$E_{Edge} = \frac{2E_\gamma^2}{m_e c^2 + 2E_\gamma}. \tag{2.4}$$

The value of the Compton edge and the correspondence between the deposited energy and the scattering angle is determined by the incident photon energy.

The differential cross section for the scattering of gamma photons with free electrons was first derived in 1928 by Oskar Klein and Yoshio Nishina [11] using quantum electrodynamics. The angular distribution of the scattered photon is known as the Klein-Nishina cross-section formula [12] and given by:

$$\frac{d\sigma}{d\Omega} = \frac{Zr_0^2}{2}\left(\frac{1+\cos^2\theta}{(1+\alpha(1-\cos\theta))^2}\right)\left(1+\frac{\alpha^2(1-\cos\theta)^2}{(1+\cos^2\theta)[1+\alpha(1-\cos\theta)]}\right), \tag{2.5}$$

where $\alpha = E_\gamma/m_e c^2$ and r_o is the classical electron radius. For 511 keV gamma photons the above cross section shows that forward scattering has very high probability, as shown in Fig. 2.9. The above expression reduces to the classical Thompson cross section at low photon energies.

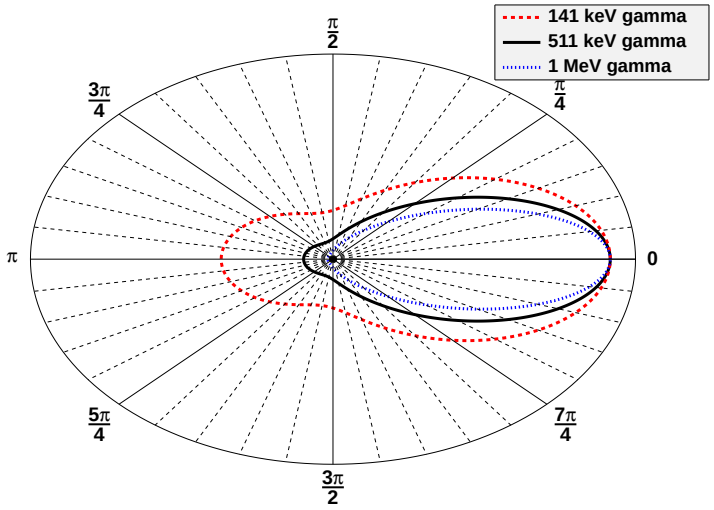

FIGURE 2.9: Angular distribution of Compton scattered 511 keV and 141 keV photons in Silicon, given by Klein-Nishina formula.

What has been stated earlier is valid assuming that the gamma interacts with an electron at rest. But this is an approximation. If the electron momentum is taken into account neither the angle-energy relations nor the Klein-Nishina formula (2.5) are completely valid. The electron pre-collision momentum creates a broadening in the energy spectrum

of the scattered photon which is known as the Doppler broadening effect. The distance traveled by the electron ejected from the atom is shorter than the spatial resolution of today's solid state detectors, making impossible to measure the energy and momentum of the electron in order to correct for this effect. This effect introduces an error on the calculated Compton scattering angle θ. We will discuss the Doppler broadening effect and how it affects the angular resolution of Compton cameras in section 2.2.2.3.

2.2.1.2 Photoelectric Absorption.

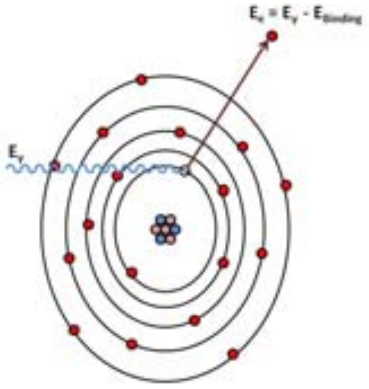

FIGURE 2.10: Schematic representation of the photoelectric interaction. The photon is absorbed by an electron which is expelled from the atom.

In a photoelectric absorption a gamma photon interacts with a bound electron of the inner shells (usually from the K-shell) of one of the atoms composing the material and is absorbed. A small amount of the photon energy is transferred to the atom as recoil in order to preserve momentum conservation. Most of the gamma photon energy goes to the electron as kinetic energy and some of it is used to overcome the electron binding energy. The atom is ionized in the process and the expelled electron is usually called photoelectron. The vacancy left by the photoelectron will be filled eventually by other electron of the material resulting into the emission of characteristic X-ray photons or Auger electrons. The energy of these extra photons or electrons depends on the energy shells structure of the atom involved and therefore on the material in which the interaction takes place.

The peaks in the mass attenuation that can be seen in figure 2.7 are known as absorption edges and corresponds to the energies of the K and L shells of the atoms. If the gamma energy is below one of these edge energies then the photon does not have enough energy to overcome the binding energy of this electron and the interaction is not possible.

The photoelectric absorption is more probable for low energy gammas (few keV) and becomes more important with increasing Z. Given the complexity of the process there is no analytic expression for the cross section. The contribution τ of the photoelectric absorption to the total mass attenuation coefficient μ/ρ can be approximated by the expression[12]:

$$\tau \sim \frac{Z^n}{E^{3.5}}, \tag{2.6}$$

where E is the energy of the incident gamma photon and Z is the atomic number of the atom in which the interaction takes place. The exponent n varies from 4 to 5 depending on the energy of the photon.

As in the Compton scattering, the photoelectron interacts with the material losing all its energy in the process. In the case of solid state detectors and ionization chambers most of the photoelectron energy is transferred to electrons of the valence band of the solid, resulting in the creation of a cloud of electron-hole pairs proportional to the photoelectron energy. The charge carriers cloud move under the influence of an applied bias voltage resulting in a measurable current.

High Z materials are prefered as absorbers for Compton imaging devices as they will have greater stopping power due to the increased photoelectric attenuation.

2.2.1.3 Other Interactions.

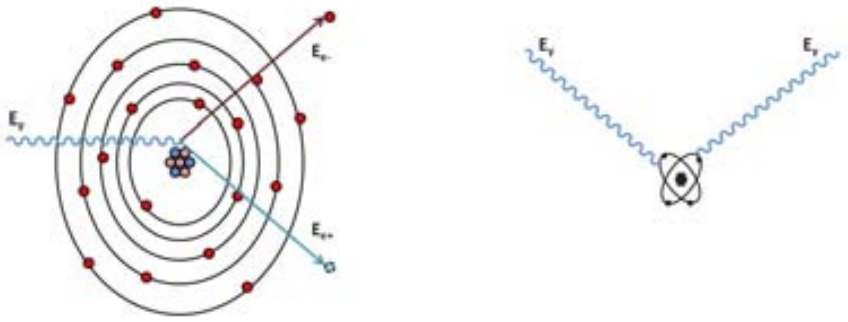

FIGURE 2.11: *Left:* Schematic representation of the pair production process. The photon disappears producing an electron-positron pair. *Right:* Schematic representation of the coherent scattering. The photon interacts with the whole atom.

Two other processes are relevant in the gamma photon interaction with matter: pair production and coherent scattering.

In a pair production process the gamma photon dissapears creating an electron-positron pair. Therefore the minimum energy required for the process is equal to twice the electron rest mass (1.02 MeV = 2 × 511 keV). The typical gamma energies used for nuclear medicine vary from few keV to one MeV, ruling out the pair production process for Compton camera. In the case of Compton camera for astrophysics applications (also known as Compton telescope), pair production must be considered as one of the backgrounds in the data.

If a gamma photon scatters after interacting with a strongly bound electron without ionizing the atom, then the equation (2.3) is still valid as long as m_e is replaced by the mass of the entire atom. In this process the atom is neither excited nor ionized and, thus, the photon does not deposit any energy in the detector. As all the scattered photons share the same energy, they are able to interfere in a coherent way, and because of this property the process is usually called coherent scattering (it is also named Rayleigh scattering after the British physicist Lord Rayleigh). The probability of coherent scattering increases with Z (as the number of bound electrons increases with Z) but is only significant (when compared with Compton scattering or photoelectric absorption) for low energy gamma photons (few keV).

The change on the direction of the gamma in coherent scattering is a concern in Compton imaging. If in a coincidence event (composed by a Compton scattering in the scatterer followed by a photoelectric absorption in the absorber) a coherent scattering happens along with the other interactions it will introduce an error in the reconstruction of the cone corresponding to this gamma.

2.2.2 Factors Affecting The Angular Resolution.

In a Compton camera for each coincidence event a cone is reconstructed (see figure 2.6). The precision of the reconstruction of the cone is what determines the image spatial resolution of the camera and, thus, its performance.

The errors on the cone reconstruction involve an uncertainty of the cone apex, direction, and opening angle, that can be quantified as an angular error. There are three factors which determine the angular resolution of the camera: the detector position resolution, the detector energy resolution, and the Doppler broadening effect. Considering each contribution Gaussian and independent, the three contributions add in quadrature to the total angular resolution of the detector

$$\Delta\theta^2 = \Delta\theta^2_{Geometry} + \Delta\theta^2_{Energy} + \Delta\theta^2_{Doppler}, \tag{2.7}$$

where $\Delta\theta_{Geometry}$ is the error corresponding to the detector position resolution, $\Delta\theta_{Energy}$ corresponds to the error introduced by the detector energy resolution, and $\Delta\theta_{Doppler}$ is the Doppler broadening effect contribution.

2.2.2.1 Detector Energy Resolution.

The aperture angle of the reconstructed cone corresponding to a coincidence event is computed using Eq. 2.1. The deposited energy of at least one[5] of the two interactions is needed for this calculation, provided that the original gamma energy is known. Any error in the energy value coming from the detector will therefore affect the value of the Compton angle.

If ΔE is the error on the energy value obtained from the chosen detector, we can propagate the error through Eq. 2.1 obtaining:

$$\Delta\theta_{Energy} = \frac{(1+\alpha(1-\cos\theta))^2}{\alpha E_\gamma \sin\theta}\Delta E, \tag{2.8}$$

where E_γ is the known energy of the emitted photon, and $\alpha = \frac{E_\gamma}{m_e c^2}$.

There are three contributions to the error ΔE in the energy measurements (FWHM) in a semiconductor detector [14, 15, 16]:

$$\Delta E = \sqrt{\Delta E^2_{Fano} + \Delta E^2_{Electronics} + \Delta E^2_{Trapping}}. \tag{2.9}$$

The first contribution ΔE_{Fano} comes from statistical fluctuations in the charge carrier formation (see Chapter 4, section 4.2.1) and can be expressed as [17]:

$$\Delta E_{Fano} = 2.35 \cdot \sqrt{\epsilon \cdot F \cdot E}, \tag{2.10}$$

where ϵ is the energy required to create a charge carrier pair and F, called the Fano factor, is a dimensionless number which depends on the detector material (0.115 for Silicon and 0.11 for CdTe) .

The second contribution $\Delta E_{Electronics}$ corresponds to the noise introduced by the readout electronics that processes the detector signals. This contribution is fixed for all the energies.

[5] It has been shown by Clinthorne [13] that it is preferred to use the energy of both detector hits for the Compton angle computation to minimize the effect of the energy resolution of the detectors on the calculation of the angle. We will use only the energy deposited in the scatterer as Doppler broadening error dominates over the energy resolution contribution.

The third contribution $\Delta E_{Trapping}$ is due to impurities and defects in the semiconductor crystal that can trap the charge carriers as they move towards the detector electrodes. This contribution is strongly dependent on the the type of semiconductor used.

The energy resolution R of the detector is defined [12] as the FWHM of the photo-peak divided by its height. Assuming that the photo-peak has Gaussian shape, the energy resolution corresponds to:

$$R = \frac{\Delta E}{E}. \tag{2.11}$$

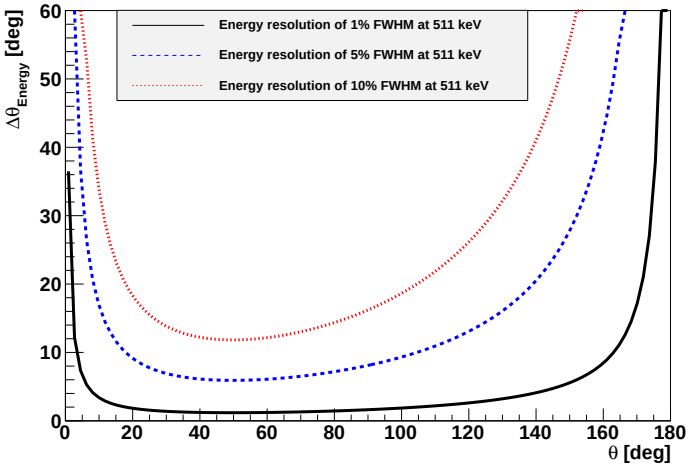

FIGURE 2.12: Contribution of the detector energy resolution to the angular error for different values of the energy resolution.

The detector energy resolution contribution to the angular error according to Eq. 2.8 and 2.12, is show in Fig. 2.12. The three curves correspond to different values of the energy resolution $\Delta E/E$ on the 511 keV photo-peak. The effects of the detector energy resolution are included into the Monte Carlo simulation of the Compton camera as will be explained in chapter 4, section 4.2.1.

2.2.2.2 Detector Spatial Resolution.

The detector spatial resolution is determined entirely by its geometry. In the case of pixelated solid state detectors, the voxel size determines the angular error contribution. If the charge cloud produced by the interaction is completely contained in a single voxel then its center is taken as the interaction point. On the other hand, if the charge cloud is spread across several voxels, due to the charge sharing effect, then the interaction point is the centroid position of the charge distribution. Either way the voxel size introduces an error on the interaction point which depends on the voxel dimensions.

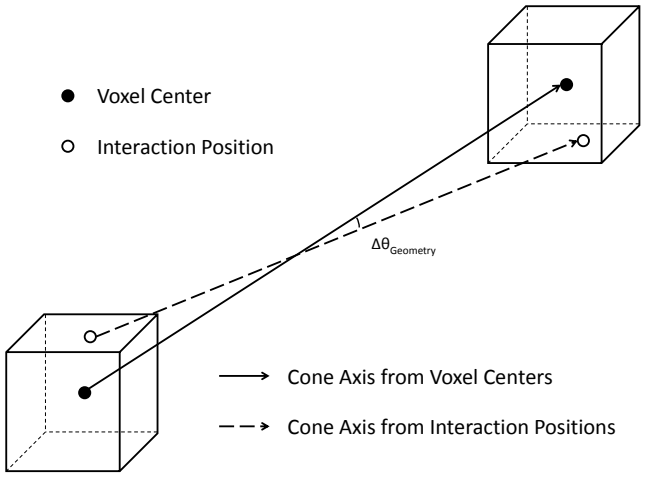

FIGURE 2.13: Effect of the voxel size on the angular error. The difference between the voxel centers and the real interaction position results in an angular error $\Delta\theta_{Geometry}$.

In the case of the Compton camera, this limited precision results in a parallax error in the cone direction which is calculated from the scatterer and the absorber interaction points. This error does not depend only on the voxel sizes but also on the scatterer to absorber distance too. With increasing distance between the scatterer and the absorber the parallax error reduces.

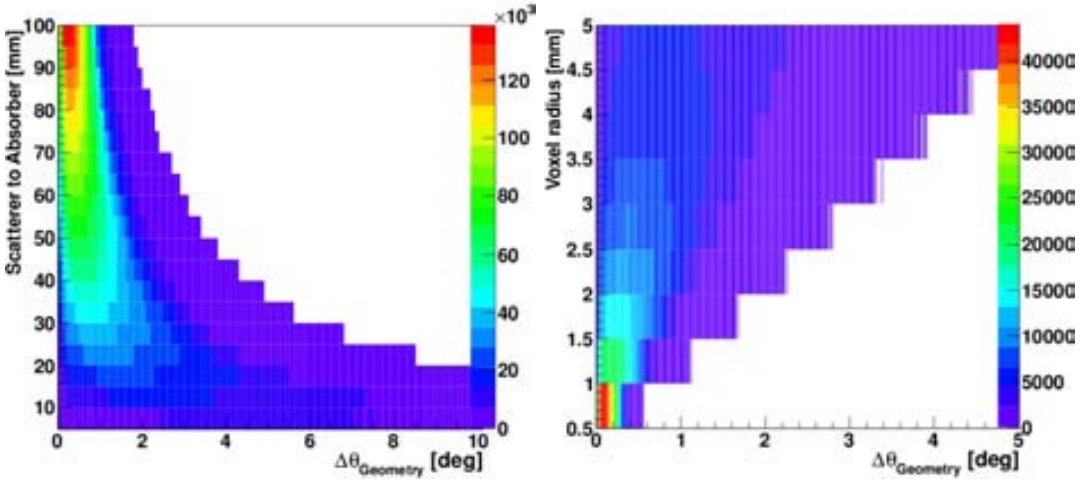

FIGURE 2.14: *Left:* effect of distance on $\Delta\theta_{Geometry}$, assuming a 1.5 mm radius spherical voxel. *Right:* effect of voxel radius on $\Delta\theta_{Geometry}$, assuming a distance between the scatterer and the absorber of 10 cm.

In order to characterize $\Delta\theta_{Geometry}$ we assume a uniform probability of interaction inside each one of the voxels and, for simplicity, a spherical voxel shape. This simple model allows us to provide upper limits for $\Delta\theta_{Geometry}$. Fig. 2.14 shows the effect of the two model parameters, i.e., the distance between the voxels and the voxel radius.

The full effect of the geometry on the image spatial resolution through the geometrical angular error is included in the analysis in the Monte-Carlo simulation as the complete geometry of the detector is simulated and taken into account in the event reconstruction.

2.2.2.3 Doppler Broadening Effect.

The Doppler broadening effect imposes an inherent limitation on the angular resolution of any Compton camera for nuclear medicine applications. All the equations shown in section 2.2.1.1 were valid under the assumption that the interaction happens with an electron at rest. In general the interaction takes place with a bound, moving electron. The momentum of the electron results in a broadening of the gamma spectrum lines given by Eq. 2.3 and this leads to an error on the computation of the Compton scattering angle θ. The equation that accounts for the electron movement is [18]:

$$p_z = -mc\frac{E_\gamma - E'_\gamma - E_\gamma E'_\gamma \frac{1-\cos\theta}{mc^2}}{\sqrt{(E_\gamma)^2 + (E'_\gamma)^2 - 2E_\gamma E'_\gamma \cos\theta}}, \tag{2.12}$$

where p_z is the electron momentum, before the interaction, projected upon the gamma momentum transfer vector. This equation reduces exactly to Eq. 2.3 taking $p_z = 0$.

The angular distribution is also affected by the electron motion and the Klein-Nishina cross-section must be modified giving the following expression [18]:

$$\frac{d^2\sigma}{d\Omega dE'_\gamma} = \frac{mr_0^2}{2E_\gamma}\left(\frac{E'}{E_\gamma} + \frac{E_\gamma}{E'} - \sin^2\theta\right)\frac{E'_\gamma}{\sqrt{(E_\gamma)^2 + (E'_\gamma)^2 - 2E_\gamma E'_\gamma \cos\theta}} J(p_z), \tag{2.13}$$

where E' is the Compton energy calculated from θ (through Eq. 2.3), and $J(p_z)$, known as Compton profile, is the electron momentum distribution on the material. The value of the Compton profiles are important as they give insight of the electron movement in the atom. They have been calculated using the Hartree-Fock method and tabulated [19].

The typical angular error introduced by Doppler broadening in Si is around 3° for 511 keV gammas scattering in angles between 20 and 80 degrees [20]. In our analysis the Doppler broadening effect is included in the Monte-Carlo simulation (as implemented in Geant4).

2.3 State of the Art Compton Cameras.

As stated earlier, the Compton camera has the potential to overcome the intrinsic limitations of traditional SPECT systems. When compared to SPECT, the Compton camera yields higher efficiency without having to sacrifice image resolution, direct 3D images without having to move the detector are possible, and (if the detectors have enough energy resolution) multiple radiotracers with different energies can be used simultaneously.

However, a combination of technological limitations and technical challenges have prevented Compton cameras to become a suitable alternative to SPECT in today medical practice. As have been discussed in the previous section, in order to reconstruct the Compton cones with enough precision a high spatial resolution and, simultaneously, a high energy resolution is required for all the detectors. The scintillation crystals usually used in SPECT cannot fulfill these requirements. But even if the detector requirements were met, the image reconstruction from the Compton cones is a complex and challenging problem by itself. The complexity of the image reconstruction problem imposes higher computational power requirements than for SPECT, making some algorithms impossible to implement with the current computer processing power. As a result of all these difficulties, more than 30 years after the Compton camera was proposed for its use in nuclear medicine [10] there is still no commercially available Compton camera for medical applications.

Although the Compton camera has not been able to become a suitable replacement for SPECT, it has found applications in homeland security [21] and astronomy. The Compton telescope (COMPTEL) [22, 23] was part of the Compton Gamma Ray Observatory (CGRO) of NASA. CGRO was an space observatory set in earth orbit, for the detection of gamma radiation from the keV up to the GeV range. It was operative from 1991 to 2000 and included several experiments and detectors, being COMPTEL one of them.

There has been a resurgence in the research related to Compton cameras in recent years. The development in solid state detectors allows for the first time to fulfill the requirements of Compton imaging for medical applications. A Compton camera prototype using Doubled Sided Silicon Strip Detectors (DSSSD) and pixelated CdTe has been reported [24]. The prototype achieved a resolving power better than 3 mm for a 364 keV ^{131}I source at a distance of 30 mm of the detectors. The image spatial resolution achieved with point-like sources was 6 mm at a distance of 30 mm from the detectors and 18 mm at 150 mm distance. Images of extended sources and with a rat was also performed. The simultaneous Compton imaging of multiple radiotracers of different emission energies has also been shown [25] by a Compton camera prototype based on germanium detectors.

Another application in nuclear medicine of the Compton camera that has been researched in the recent years is the beam tracking during hadron beam therapy. In hadron beam therapy a tumor is bombarded with a beam of massive particles (usually protons). The stopping power of a given tissue versus the penetrating length has a peak (known as Bragg peak) which depends on the energy of the incident particles. This allows to focus the treatment in the tumor minimizing the damage on the healthy tissue. Hadron beam therapy requires a precise tracking of the beam interaction with the body in order to assure that the Bragg peak is in the tumor area. The monitoring of the beam is performed through the detection of secondary particles emitted as a result of the interaction of the beam particles with the nucleus belonging to the atoms of the patient tissues. Compton cameras based on semiconductors have been proposed as a beam tracker [26] because of their high efficiency which allows to perform in vivo imaging.

In the following chapter we will describe a novel modular solid state detector design, originally developed for PET, but the design can be modified to be used for Compton camera. The solid state detectors allow to achieve the energy resolution and spatial resolution required by Compton imaging. The increased performance of today computers and the improvements in the field of image reconstruction allow for the first time to obtain image resolutions comparable to SPECT while having an increased efficiency.

Chapter 3

Voxel Imaging PET Pathfinder Project

A Compton camera designed for medical imaging application has stronger requirements for the detector elements used than that for the Anger camera used in SPECT. In a traditional SPECT system the spatial resolution of the gamma camera is limited by the collimator. The energy resolution of the detectors is only used to discard scattered events[1]. In the case of the Compton camera, the reconstruction of the Compton cone from the coincidence events involves both the impact points and the deposited energies of the interactions. Thus high precision in the measurement of both parameters is needed.

The scintillator crystals coupled to PMTs usually used for conventional gamma cameras (see chapter 2), cannot fulfill the demanding requirements of a Compton camera for medical imaging. Although the scintillators can be segmented in the x-y plane parallel to the PMT array, they cannot be further segmented in the direction perpendicular to the PMT array (the typical size of a LSO crystal segment is $4 \times 4 \times 10$ mm^3). Also the energy resolution of scintillators (above 10% FWHM for 511 keV photons) is not enough to compute the Compton angle with sufficient precision.

Room temperature solid-state semiconductor material, like CdTe, allows to overcome the limitations of conventional scintillators. This material can be pixelated to create arrays of millimeter size voxels and it can achieve excellent energy resolution[27] (less than 1% FWHM for 511 keV photons).

In this chapter we discuss the novel detector design proposed by the VIP pathfinder project, first in the context of PET (the purpose for which it was conceived), and then in the context of Compton camera.

[1] i.e., events that lost some of its energy in an interaction previous to the detection.

3.1 State-of-the-Art PET scanners and the VIP proposal.

PET scanners are widely used both in regular medical practice as well as for preclinical research with small animals. The development of radiotracers like ^{18}F-fluoredeoxyglucose (^{18}F-FDG) allows to track the glucose metabolism with applications in oncology (detection of cancer metastases) and neurology (mapping brain physiology). PET scanners yield high efficiency and high image spatial resolution and can be combined with other techniques like CT or MRI to obtain complementary information about the density of the structures scanned.

A PET scanner is composed by position sensitive detectors surrounding the patient, usually in a ring shape. The positron emitted by the radioactive isotope travels through the human tissue losing its kinetic energy by Coulomb interactions with the material electrons. When most of the positron kinetic energy is lost it can interact with an electron of the material to form an hydrogen-like unstable state called positronium [28]. The positronium quickly decays because of the annihilation of the electron and the positron producing a pair of 511 keV back-to-back gamma photons (i.e., emitted at an angle of 180° relative to each other). The purpose of the PET scanner is to detect this photon pairs (true PET events). The interaction positions of the detected gamma photon pair is used to reconstruct a line, known as Line-of-Response (LOR), on which the origin emission point of the photons is located. Standard emission tomography image reconstruction techniques allow to obtain the image of the radiotracer distribution.

The movement of the positron before the annihilation creates an smearing in the reconstructed image imposing a lower physical limit in the resolution that can be achieved by PET. The distance traveled by the positron depends on its initial kinetic energy and, thus, on the radiotracer employed. In the case of ^{18}F-FDG the mean distance traveled in the human tissue is ∼0.6 mm[29]. Moreover, fluctuations in the positron momentum before the annihilation result in a noncolinearity of the emitted photon pair, introducing an angular uncertainty ∼0.23°[30] on the 180° angle.

While the intrinsic physical limitations impose a lower bound on the image spatial resolution, the driving factor of the image quality of a PET scanner is the performance of the detectors involved. The precision on the reconstruction of the LOR determines the quality of the images reconstructed. As shown in figure 3.1 a pair of coincident interactions can be wrongly identified as a PET event. The two main contributions to these false coincidences are the scattered and the random events. In a scattered event one (or both) of the gamma photons suffer a scattering with the body before reaching the detectors resulting in a wrong LOR. As the energy of the emitted photon is known the scattered events can be rejected by comparing the measured energy of the detected

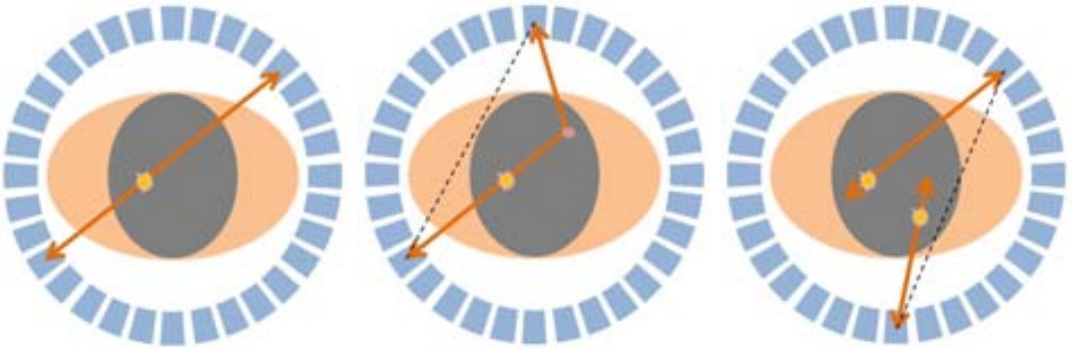

FIGURE 3.1: *Left:* schematic representation of a true PET coincidence. *Center:* schematic representation of an scattered event. *Right:* schematic representation of a random event.

gamma photons with the energy of the original photon (i.e. 511 keV). The random events occur when two gamma photon pairs are emitted simultaneously (within the time precision of the detectors), and only two of the four gammas are detected which will be wrongly identified as a PET event. The rate of random coincidences in a PET scanner is proportional to $2\tau A^2$ [31], where A is the injected activity and τ is the time window in which two detected gamma photons are considered to be simultaneous (τ depends on the time resultion of the detectors composing the PET scanner). The number of random events grow according to the previous relation up to the point in which the detectors begins to saturate due to the pile-up effect [12].

The state-of-the-art PET scanners used in clinical practice and preclinical research are (almost unanimously) based on scintillation crystals coupled to either PMTs, avalanche photo-diodes (APD), or silicon photo-multipliers (SiPM). The intrinsic performance and size of the scintillation crystals limits the image quality and the efficiency that can be achieved with the PET scanners, resulting in an image resolution above the physical limit discussed above. The scintillation crystals used in PET usually have a parallelepiped shape with a millimeter size pixel pitch and a thickness of tens of millimeters. The crystals are arranged in planar matrices which are put together to form a PET ring. The use of scintillator imposes limitations to the PET performance as:

- The parallelepiped shape of the crystal makes it impossible to build a seamless ring. The gamma photons can traverse the crack between the crystals arrays resulting in a loss efficiency.
- The thickness of the scintillation crystals introduces an error in the radial position of the interaction. This result into a parallax error in the reconstructed LOR and, therefore, in a poorer image resolution.

- The energy resolution of the scintillation crystals is limited to $\sim$ 10% making impossible to reject most of the scattered events which can constitute up to 50% of the detected coincidences.

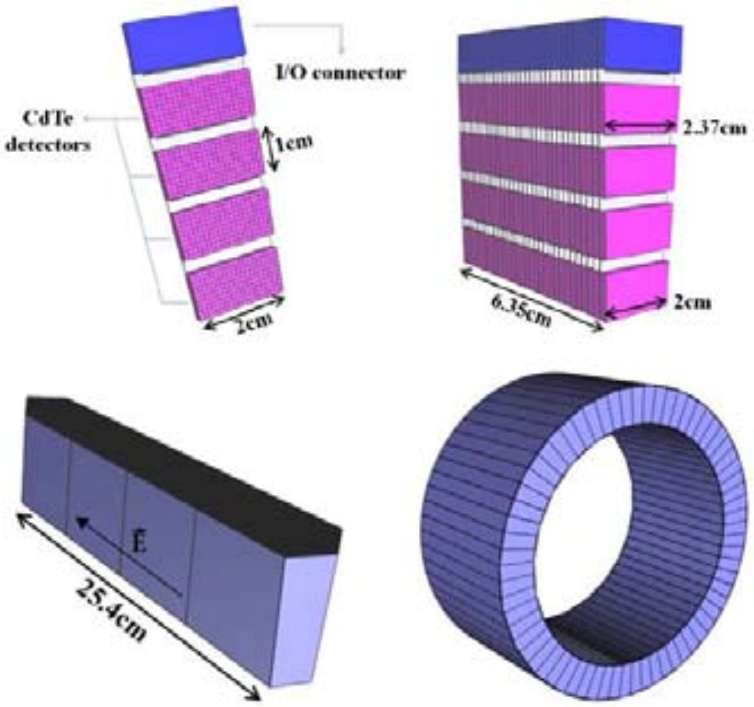

FIGURE 3.2: VIP PET design [32]. *Top left:* a single module unit containing the CdTe pixelated detectors bump-bounded to the readout ASIC and both mounted over on a PCB kapton layer. *Top right:* an stack of 30 module units forming a block is shown. *Bottom left:* a PET sector formed by the stacking of four blocks. *Bottom right:* a seamless PET ring made from trapezoidal PET sectors. [32]

The VIP pathfinder project proposes [32] a novel detector design using pixelated solid-state technology (CdTe) instead of scintillator crystal in order to overcome the limitations of scintillator based PET scanners. The design of the PET based on the VIP module detectors (described below) can achieve:

- The CdTe crystals can be segmented into millimeter size voxels. The VIP module design allows to create high density 3D arrays of such voxels. This results into a millimeter precision on the photon impact point and a consequent reduction of the parallax error.

- The CdTe detector can achieve an excellent energy resolution of less than 1% FWHM for 511 keV photons (see section 3.4). This allows the user to identify and reject the scattered events making the PET virtually immune to this noise contribution.

- The CdTe crystals can be cut in a trapezoidal shape allowing to make a seamless PET ring. The efficiency of the scanner is increased as there are no cracks in the PET ring from which the photons can escape.

- The VIP is designed in such a way that the electric field inside the CdTe crystals is parallel to the magnetic field of an MRI scanner. As a consequence the magnetic field will have no effect on the performance of the detector making the PET compatible with MRI.

VIP features a modular design (see figure 3.2) in which the basic element is the detector module unit (that we will call just *module* from now on). The module contains four CdTe crystals of 10×20 mm^2 size and 2 mm thickness. Each of the CdTe crystals is electronically pixelated into 200 voxels with a volume of $1\times1\times2$ mm^3. The voxels are connected to a dedicated ASIC through the bump-bonding technique. The ASIC, called VIP-PIX, has been developed within the project in order to provide a complete and independent signal processing for each one of the voxels (see section 3.3). The ASIC together with the CdTe crystal is mounted on a kapton printed circuit board. In order to reduce the passive material, both the ASIC and the kapton are thinned down to a 50 μm thickness.

The module is the building block from which the PET scanner is made. As shown in figure 3.2, in order to obtain the PET ring, 30 modules are stacked to form a module block, then four blocks are stacked to form a PET sector, and finally 66 sectors are put together to form a ring. In this way a seamless PET scanner with ∼6.3 million channels and a density of ∼450 voxels/mm^3 is made. The inner radius of the PET is 42 cm and the outer radius is 54 cm with a length of 25.4 cm. The stopping power provided by the 4 cm of CdTe corresponds to ∼70% probability of absorption for the 511 keV gamma photons and this translates into ∼50% detection probability of gamma photon pairs produced from a positron annihilation. The performance of the VIP scanner has been evaluated through Monte Carlo simulations[32, 33, 34]. In figure 3.3 we show the reconstructed image of the Derenzo phantom (see chapter 6, section 6.6 for a detailed description of the phantom) using the VIP PET scanner. The small rods with 1mm diameter are clearly distinguished. The FBP algorithm is used to reconstruct the image.

The flexibility of the modular design of VIP allows to explore other possible applications of the module detector unit. One of this applications is Positron Emission Mammography (PEM). The most common design of PEM consists of two arrays of scintillation crystals mounted into two parallel paddles to immobilize the breast during the scan. The two detector arrays move along the paddles collecting coincidences in the same way as a PET scanner. Using the VIP modules instead of scintillation crystals will result into

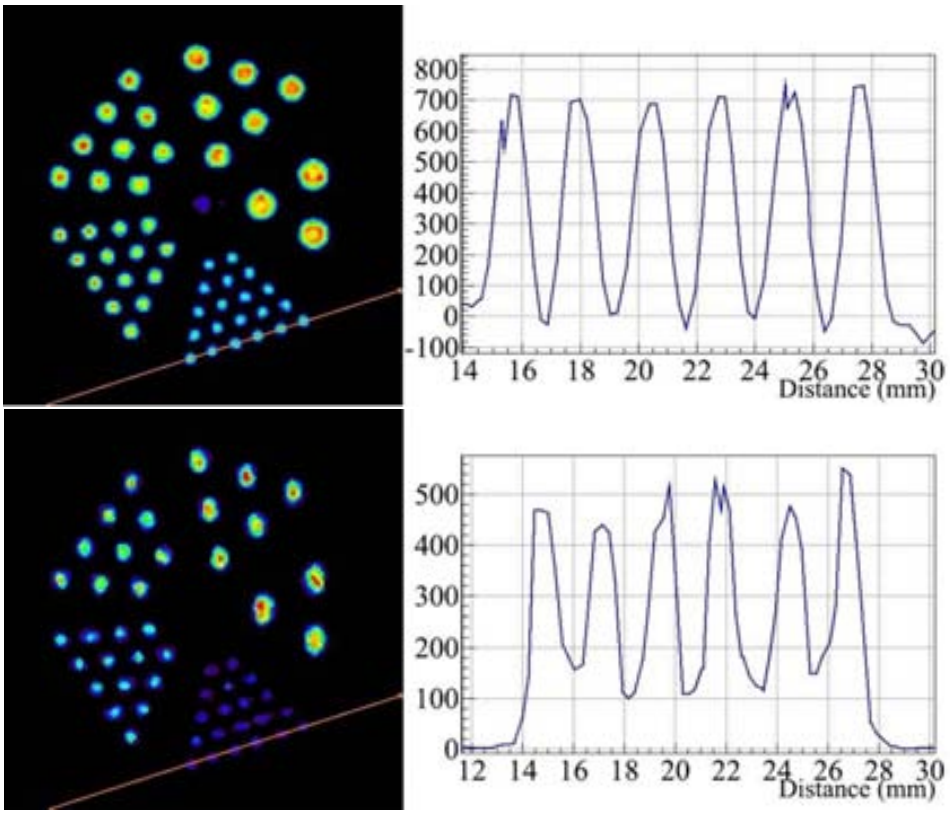

FIGURE 3.3: Reconstructed images of the Derenzo phantom (see chapter 6, section 6.6 for a detailed description) with the VIP PET (top) and the VIP PEM (bottom) scanners. The line profiles of the 1 mm diameter rods is also shown. The images are reconstructed using the FBP algorithm in the case of PET and the OE algorithm in the case of PEM (see chapter 5 for a description of these algorithms). [33]

an improvement of the image quality in PEM for the same reasons stated before for PET. The performance of a proposed PEM scanner based on the VIP module has been evaluated through Monte Carlo simulations[35]. In figure 3.3 we show the reconstructed image of the Derenzo phantom using the VIP PEM scanner. The small rods with 1mm diameter are clearly distinguished. The OE algorithm is used to reconstruct the image.

In this thesis we will explore the application of the technology developed within the VIP pathfinder project to make a Compton camera tomographer. In the next section we will describe in detail the two module design proposed to build the scatterer and the absorber detectors that compose the Compton camera.

3.2 VIP Compton Camera.

Following the same concept explained in section 3.1, the scatterer and the absorber detectors composing the VIP Compton camera are made from the stacking of detector

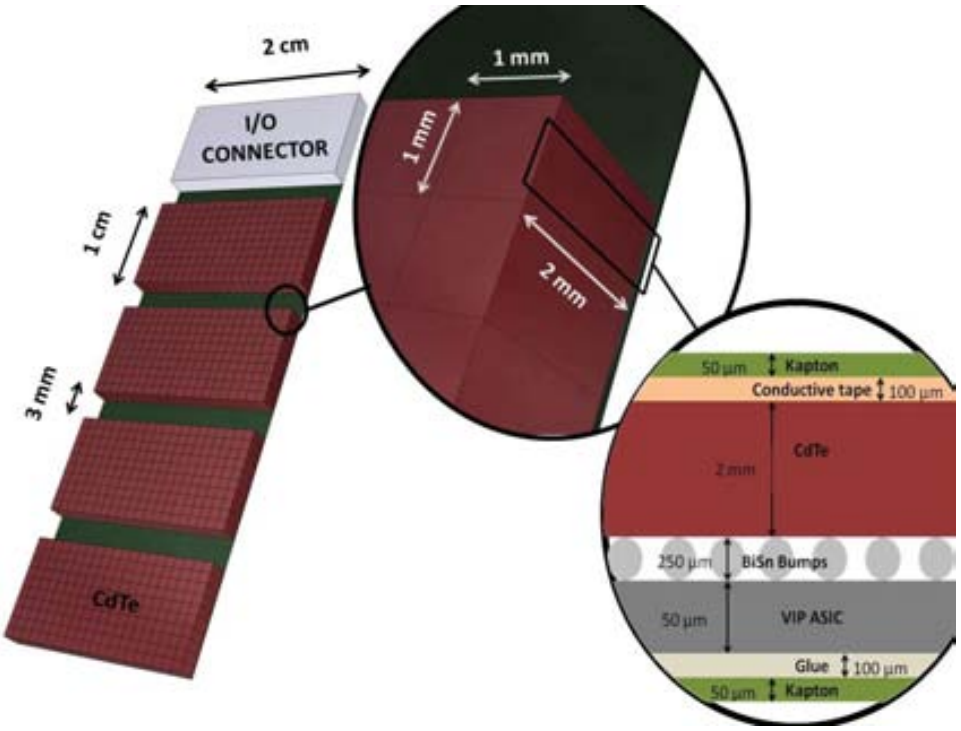

FIGURE 3.4: The absorber module consisting of four $10 \times 20 \times 2$ mm^3 CdTe crystals bound-bounded to the VIP read-out ASIC which is mounted over a PCB kapton layer. The voxel size is $1 \times 1 \times 2$ mm^3.

module units (that we will call *modules* from now on). The detector material for the absorber is chosen to be CdTe for its excellent energy resolution (see section 3.4) and its high photoelectric cross section (due to its high Z). In the case of the scatterer, silicon has been chosen because of its high cross section for Compton scattering and its good energy resolution. The distribution of the Si crystals and the connectors in the scatterer module is different with respect to the absorber detector in order to minimize the passive material in the trajectory of the gamma photons.

The absorber module (see figure 3.4) is rectangular and holds four $10 \times 20 \times 2$ mm^3 pixelated CdTe crystals. Each of the CdTe crystals is connected to a read-out ASIC through a matrix of 10×20 electrodes made of 250 μm diameter BiSn bumps. As a result each CdTe crystal is segmented into 10×20 voxels of $1 \times 1 \times 2$ mm^3 volume. During production, the wafer containing the ASICs is thinned down to a 50 μm thickness in order to minimize the passive material in the path of the gamma photons. The read-out ASIC is designed in such a way that each one of these electrodes are coupled to a fully integrated signal processing microchip and constitutes a completely independent detector for the deposited energy, position and arrival time of the photons. The ASIC (with the CdTe crystal on top bonded to the ASIC through the solder bumps) is glued on a 225 μm thick kapton PCB through a 100 μm thick conductive glue layer, which

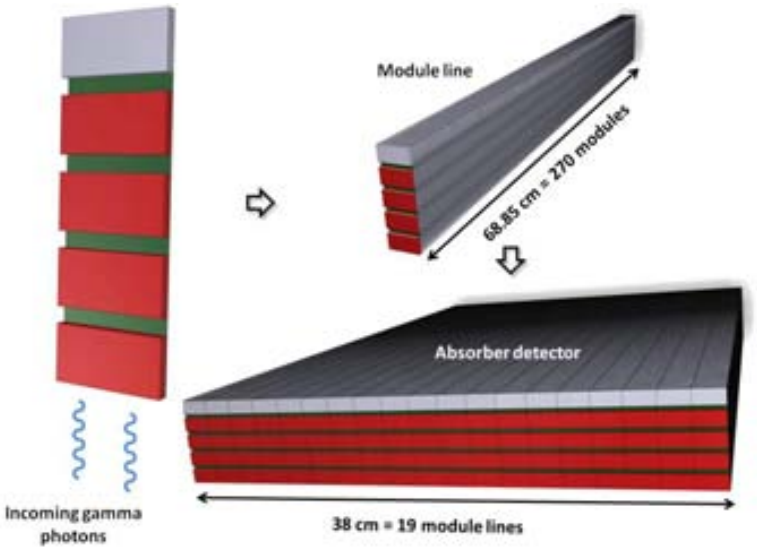

FIGURE 3.5: Absorber detector made from the stacking of module units. 270 absorber modules are stacked forming a line of 20 mm × 40 mm × 540 mm. 19 lines are stacked in order to build the absorber.

also serves as a common ground reference to all the chips. The kapton PCB contains the bus that carry the data from the ASICs to the external electronics.

In order to build the absorber detector 270 unit modules are stacked forming a *module line* (see figure 3.5). 19 module lines together form a parallelepiped absorber detector with a FOV of 540 × 380 mm^2 and a depth of 40 mm. The FOV size has been chosen in order to be comparable to gamma cameras found in commercially available SPECT systems.

The scatterer module (see figure 3.6) has a rectangular shape holding 19 Silicon (Si) crystals with sizes 10 × 10 × 2 mm. The Si crystals are put together to form a 190 × 10 × 2 mm unique crystal. In the same way as the absorber detector each one of the Si crystals is bump bonded to a read-out ASIC through an array of 10 × 10 conductive glue bumps with 15 μm diameter . In this way the Si is segmented in the same way as the CdTe of the absorber, creating voxels of 1 × 1 × 2 mm^3. The ASICs are mounted on a 50 μm PCB kapton layer as in the case of the absorber module.

To build the scatterer detector two mirrored scatterer modules are put together forming a single unit of 38 cm long. 270 of these units are stacked to form a scatterer slice consisting of a parallelepiped with sizes 540 × 380 × 1 cm^3. The scatterer depth can be adjusted in steps of 1 cm by adding slices. The optimal scatterer thickness depends on the energy of the gamma photon emitted by the source.

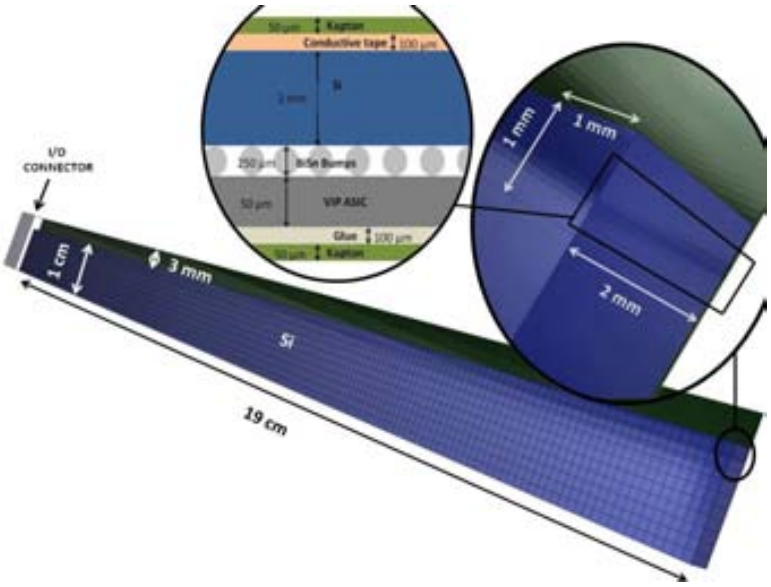

FIGURE 3.6: The scatterer module consisting of 19 $10 \times 10 \times 2$ mm^3 Si crystals bump bonded to the VIP read-out ASIC which is mounted over a PCB kapton layer. The voxel size is $1 \times 1 \times 2$ mm^3.

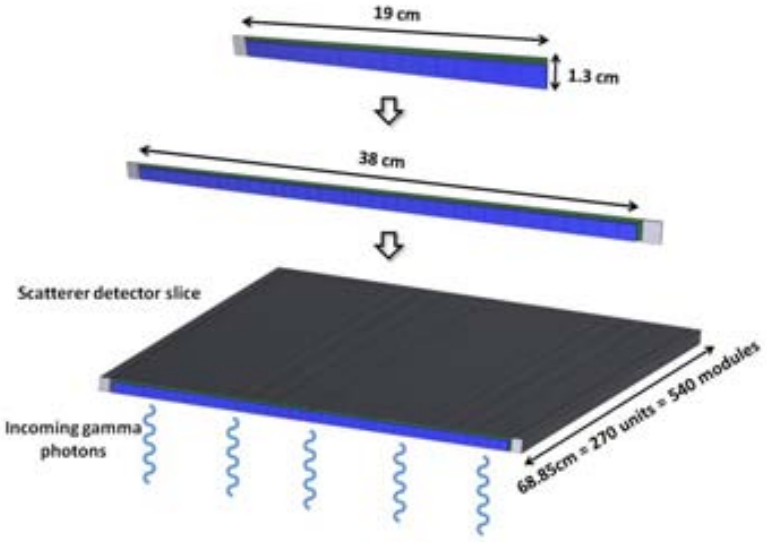

FIGURE 3.7: Scatterer detector slice build from the stacking of modules. Several slices can be put together in order to obtain different scatterer thicknesses.

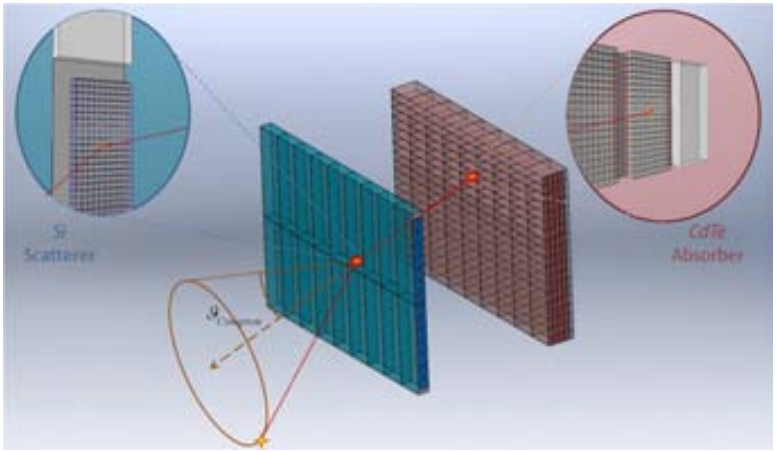

FIGURE 3.8: Schematic image of the VIP Compton camera design.

The Compton camera tomographer is composed by the scatterer and absorber detectors as shown in figure 3.8. In section 6.1 of chapter 6 the different parameters of the geometry of the camera (scatterer thickness, absorber thickness, and scatterer to absorber distance) will be optimized through Monte Carlo simulations.

In the next section we will provide an overview of the ASIC developed to read out the detectors.

3.3 VIP Read-Out ASIC.

The VIP read-out ASIC (named VIP-PIX) is being designed and developed within the VIP project to be integrated in the module detector discussed in the previous section. This ASIC design provides a *smart pixel* solution to the detector as each of the voxels in which the solid-state detector is segmented, has its own independent read-out electronics.

The VIP-PIX is designed to fulfill the requirements imposed by the CdTe detectors and medical imaging applications. Its most important features are:

- VIP-PIX provides a low noise read-out for the energy and timing measurements of every channel.
- The ASIC is thinned in order to reduce the passive material in which the gamma photons can scatter.
- Each channel has its own fully integrated signal processing electronics in order to provide the deposited energy and the timestamp information.

- Given the high number of channels to read in the full Compton camera (more than 6 million) the power consumption of the ASIC is also minimized.

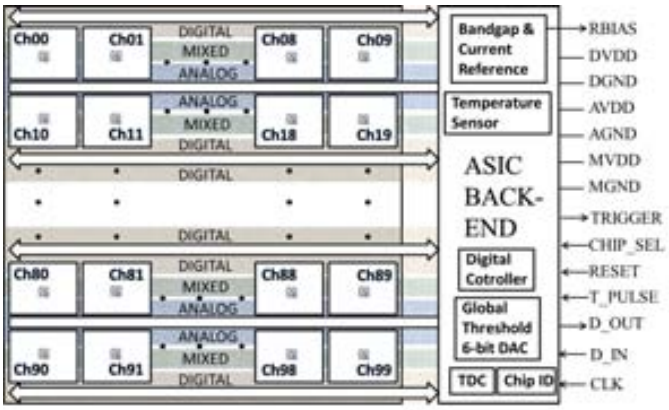

FIGURE 3.9: VIP-PIX architecture. The ASIC is divided in two zones: The front-end, containing a 2D array of independent pixel electronics for the 10 × 10 pixels, and the back-end electronics. [36]

The ASIC, with an area of 10 × 12 mm^2, can be divided into two regions (see figure 3.9): the front-end electronics, with an area of 10 × 10 mm^2, and the back-end electronics, with an area of 10 × 2 mm^2. The front-end electronics consists of a 2D array of independent pixel electronics for the signal processing of the 10 × 10 pixels that each ASIC can manage. The back-end controls the pixel electronics and the overall ASIC functions. It includes voltage reference DACs, a temperature sensor, a time to digital converter (TDC), the chip ID circuit, and the digital controller that manages the pixel electronics and the data flow between the array and the FPGA controller. During the production, the wafers containing the ASICs will be thinned down to 50 μm thickness in order to minimize the ASIC volume and thus the passive material in the module.

As shown in figure 3.10, the pixel electronics feature a charge sensitive amplifier, a shaping amplifier, a peak-and-detect circuit, a 10 bits analog-to-digital converter (ADC), and an integral discriminator, in an area of 0.5×0.7 mm^2. The pulses coming from the energy depositions in the solid-state detector are integrated by the charge sensitive amplifier. The voltage output goes in parallel to two different lines one for the energy measurement and the other for the trigger implementation and the timing measurement.

To measure the deposited energy the output of the preamplifier is fed into a shaping amplifier which transforms the voltage step into a voltage pulse, filtering noise in the process. The shaped signal goes then to a peak-and-detect circuit that detects its maximum value and holds it. The output of the shaper is then digitalized by the 10 bits ADC providing the energy value with an intrinsic resolution limit of 0.5 keV for a dynamic range of 511 keV.

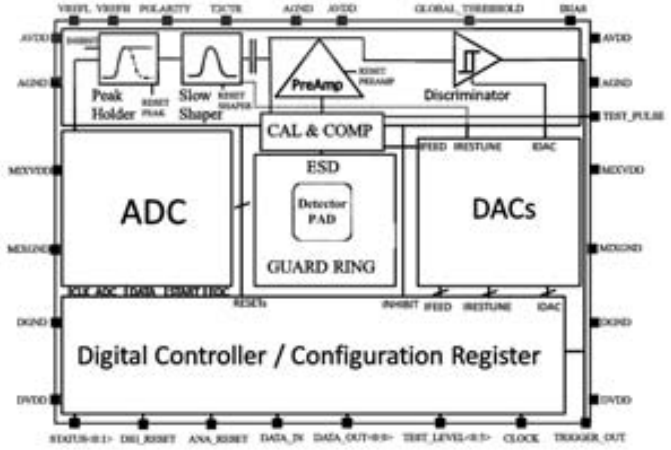

FIGURE 3.10: Architecture of the read-out pixel electronics [36]. Each pixel have its own charge sensitive amplifier, shaper, peak-and-hold circuit and a 10 bits ADC. The trigger is provided by an integral discriminator. [36]

The pixel self-trigger is implemented through an integral discriminator which sends a signal when the charge sensitive amplifier output is higher than a certain threshold. The discriminator output also serves as input to the back-end TDC in order to provide the timestamp measurement with respect to a global time reference (provided by a common 40 MHz clock) on the electronics external to the ASIC.

VIP-PIX can work with positive or negative input signals. Prototypes to test the different elements of the ASIC has been made and the results have been reported[36, 36]. With a power consumption of 200 μW/channel, the measured electronic noise for positive polarity was 98 e^- RMS and for negative polarity was 107 e^- RMS. The time jitter of the discriminator was below 10 ns for energy depositions above 20 keV. The final version of VIP-PIX which has 100 channels, will be ready in 2014.

In section 4.2 of chapter 4 we will describe the signal processing electronics for semiconductor detectors (like CdTe) and its implementation on the Monte Carlo simulation of the VIP Compton camera.

3.4 CdTe Energy and Time Resolution Characterization.

In order to assess the performance of the CdTe detectors involved in the various scanners proposed by the VIP project, various laboratory tests have been conducted within the project.

To test the energy resolution and the timing response of the detectors, a pair of CdTe Schottky diodes developed by ACRORAD[2] has been characterized. The detectors have a volume of 4 × 4 × 2 mm^3. The cathode is made of Pt while the anode is made of Au/Ti/Al [37].

The setup features both detectors working in coincidence for timing response tests. In each of the detectors the signal is integrated through an AMPTEK A250[3] charge sensitive amplifier. The output of the charge sensitive amplifier goes in parallel to two lines. In one of them the signal goes to an AMPTEK A275[4] shaper which output goes to a peak sensing VME module CAEN V758N[5]. The peak sensing module measures the signal maximum within a 4 μs time gate. The other line contains the integral discriminator LeCroy 821[6] which implements the trigger threshold and allow the measurement of the timestamp. This scheme of signal processing mimics at functional level the signal processing of the pixel electronics in the VIP-PIX ASIC described in the previous section.

The spectroscopy data is obtained for ^{57}Co and ^{22}Na. The most probable energy of emission of gamma photons for ^{57}Co is 122 keV which is comparable to the emission energy of ^{99m}Tc, one of the most used SPECT radiotracers. ^{22}Na, on the other hand, is a positron emitter producing 511 keV gamma photons from the annihilation of positrons and electrons. These two energies are representative of the low and high energy limits of the Compton camera operation. The data is taken at low temperature ($\sim$ -8°C) and room temperature. The detectors are cooled down (for the low temperature measure) in a fridge where nitrogen gas is flushed in order to keep the humidity below 20% avoiding condensation on the detectors. The data taking time is limited to 15 minutes, after this time, the detector bias is ramped down to 0 V for at least 30 seconds. This process ensures to avoid the effects of polarization in the detector crystals.

The obtained FWHM for the 122 keV photopeak of the ^{57}Co at room temperature is 3.7 keV which corresponds to an energy resolution of 3.03 %. In order to avoid high leakage current when operating the detector at -8°C, the bias voltage was increased to 1000 V/mm from the 500 V/mm used in the room temperature measure. Under this conditions the FWHM was reduced down to 3.2 keV which is equivalent to a 2.62% energy resolution. In the case of ^{22}Na (see figure 3.11), the room temperature measurement of the 511 keV photopeak FWHM is 8 keV which corresponds to an energy resolution of 1.57 %. The bias voltage used for the room temperature measure was 500 V/mm. When

[2] http://www.acrorad.co.jp/us/
[3] http://www.amptek.com/a250.html
[4] http://www.amptek.com/a275.html
[5] http://www.caen.it/csite/CaenProd.jsp?idmod=285&parent=11
[6] http://www-esd.fnal.gov/esd/catalog/main/lcrynim/821-spec.htm

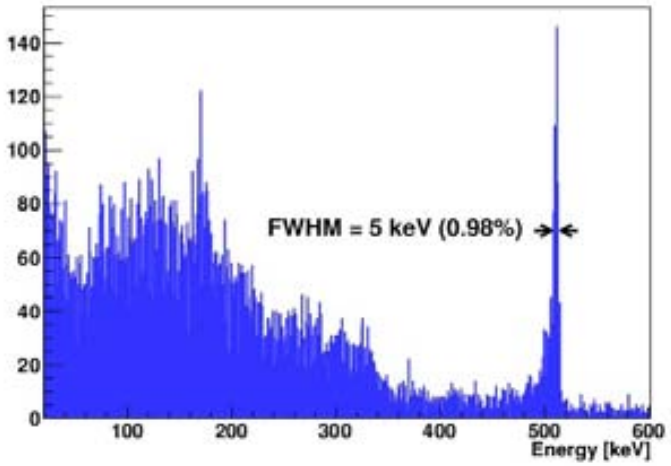

FIGURE 3.11: Spectroscopy of a ^{22}Na source obtained from the CdTe detectors. Detector operated at -7°C and 900 V/mm. [38]

cooled down to -7°C and with and increased bias of 900 V/mm the FWHM reduces to 5 keV which is equivalent to a resolution of 0.98%.

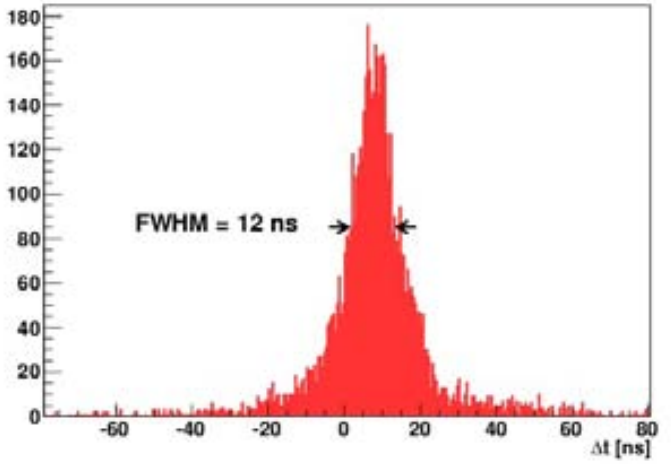

FIGURE 3.12: Measurements of the timing response of the CdTe detectors operated in coincidence PET-like mode. [38]

For the timing response measurements, two detectors described are setup face-to-face with a positron emitter source place between them. The ^{22}Na positron emitter is used to provide the back-to-back photons. The time difference of the simultaneous energy depositions is measured. This provides a lower limit for the detector timing response in the Compton camera case. The FWHM of the time difference between the two detectors is 12 ns (see figure 3.12).

The obtained energy resolution shows how the solid-state detectors improve the resolution with respect to the scintillation crystals used in SPECT gamma cameras. These results have been published[27, 38] and have been used as input for our simulation software, as explained in chapter 4.

Chapter 4

Monte-Carlo Simulation

The Monte Carlo (MC) method consists of the simulation of a system by the repeated random sampling of its inputs according to the known statistical behavior of the system. MC applications are used extensively in biology, chemistry, artificial intelligence, finance, business, etc. MC methods are especially important in physics as they allow to predict the expected result of an experiment based on an underlying theory.

In the field of nuclear medicine physics, MC methods are useful for the evaluation and modelization of novel detectors and scanners. In this thesis MC is the tool used to evaluate the Compton camera design as proposed by the VIP pathfinder project (see chapter 3). The simulation is performed in two steps. In the first step, described in section 4.1, all the physical processes happening in the camera are simulated and stored. In the second step, described in section 4.2, the stored data is processed in order to simulate the detector response and the data acquisition process.

4.1 Geant4-based Architecture for Medicine Oriented Simulations.

Geant4[39] is a MC software for the simulation of particle interactions with matter. Geant4 is completely written in the C++ programing language and in order to use it, at least some knowledge and experience with C++ is required. The users must create the simulation writing their own C++ code that includes the tools provided by Geant4. Every change in the system geometry, or in any other parameter of the simulation requires a modification of the C++ source code and posterior compilation. In order to perform the simulations in a more flexible and easy-to-use way, several frameworks have been developed. As examples we can find OSCAR[40, 41], ATHENA[42], or GIGA[43]

in the high energy physics field, MULASSIS[44] and GRAS[45] for space physics and GATE[46] in medical physics.

In case of the VIP pathfinder project, we need to simulate different types of nuclear medicine imaging scanners: PET, PEM, and Compton camera. Specifically we need to model and evaluate (using MC simulation) the conceptual design of the pixelated solid state detectors of VIP. The simulation framework we choose must allow us to do quick modifications in the geometry in a simple way and, at the same time, to go deep into the physics taking place in the detectors. For these reasons we use GAMOS[47].

4.1.1 GAMOS Overview.

GAMOS provides a framework to perform GEANT4 simulations using a simple scripting language and at the same time it features plug-in technology which allows the user to add his/her specific functions. The user must create two files: the input file (with file extension .in) and the geometry file (with file extension .geom). The input file contains the simulation configuration including the number of generated events, the source (type, energy, spatial distribution, decay time, ...), the physics included, the geometry to use, and the hit-sensitive detectors. The geometry file contains the information regarding the materials and the structure of the scanner.

To understand how GEANT4 performs the simulation we have to define the following concepts:

- *run:* set of events sharing the same geometry and physics.
- *event:* set of tracks that include particles created by the primary generator and the secondary tracks created because of the particle interactions with matter.
- *track:* information of the particle as it moves trough the geometry. It contains the initial and current state of the particle.
- *step:* information of the change of a track as the particle travels through the geometry. Contains the initial and final positions and the changes in energy, time of flight, etc.

The entire evolution of a particle track is split up in steps. In each step, the progress of a track is updated. The progress of the track can consist of a physical interaction with the current material or a change of geometry volume.

To start with GAMOS, the user has to define the geometry. In GAMOS this is done with a scripting language that allows to define parameters, materials and logical volumes. The

parameters are user defined variables which can be used anywhere in the geometry. The materials can be predefined ones or created as a combination of single atoms. The logical volumes consist of geometrical volumes (prism, sphere, cylinder, and other geometric structures defined in GAMOS) which contain given materials.

The volumes can be placed in the simulation one by one or in an automatic parametrized way. This allow to simulate detectors composed of independent voxels by placing the array of voxels into a mother volume.

As an example the following script creates a *CdTe* cube of 1 mm side in the center of the simulation world:

```
:MIXT CdTe 5.85 2
G4_Cd 0.468355
G4_Te 0.531645

:ROTM RM0 0.  0.  0.

:P CUBE_SIZE 1.0*mm
:P WORLD_SIZE 100*cm

:VOLU world BOX $WORLD_SIZE $WORLD_SIZE $WORLD_SIZE G4_AIR

:VOLU cube_of_CdTe BOX
$CUBE_SIZE/2
$CUBE_SIZE/2
$CUBE_SIZE/2
CdTe

:PLACE cube_of_CdTe 1 world RM0 0.  0.  0.
```

The material of the volumes is included in the simulation of the generated particles interaction with matter, which we will discuss below. In the previous example the *CdTe* is defined as a mixture of two components (Cadmium and Tellurium) with a density of 5.85 gr/cm^3 and with a proportion of *Cd* of 46.8355% and of *Te* of 53.1645%. Two parameters: "CUBE_SIZE" and "WORLD_SIZE", are defined, and used to specify the size of the "world" and "cube_of_CdTe" logical volumes. The rotation matrix "RM0" is defined to establish the orientation of the logical volume "cube_of_CdTe" when it is placed into the "world" volume.

Once the geometry is defined the simulation is set-up through the input file (with file extension .in) linking the geometry file and defining the physics lists to use, the hit-sensitive detectors, and the particles generated. The hit-sensitive detectors consist of the designated logical volumes of the geometry in which the interactions of particles and matter will be recorded, i.e., the active material of the simulated detector.

Moreover, users can create their own C++ code and use it together with GAMOS to perform tasks not included in the standard package. These *user actions* can be easily integrated with GAMOS and called from the input file.

In the following we are going to show an example of an input file:

```
/gamos/setParam GmGeometryFromText:FileName CdTe_cube.geom
/gamos/geometry GmGeometryFromText

/gamos/physicsList GmEMPhysics
/gamos/GmPhysics/addPhysics gamma-lowener
/gamos/GmPhysics/addPhysics electron-lowener
/gamos/generator GmGenerator

/run/initialize

/gamos/SD/assocSD2LogVol GmSDSimple Absorber cube_of_CdTe

/gamos/setParam GmHitSDTTreeUA:DataList TrackID InitialProcess FinalProcess
/gamos/userAction GmSDTTreeUA

/gamos/generator/addSingleParticleSource source gamma 511*keV
/gamos/generator/positionDist source GmGenerDistPositionPoint 0.  0.  -5.
/gamos/generator/timeDist source GmGenerDistTimeDecay 1.E5*becquerel

/run/beamOn 100
```

In the first two lines of the previous example the geometry of the simulation is established by specifying the geometry file to use. The next lines determine the physics list for the generator.

The GAMOS generator creates the simulated particles according to the user specifications. These specifications include the particle type and the distributions of energy, time, position, and direction. The energy distributions allow to fix one single energy for the

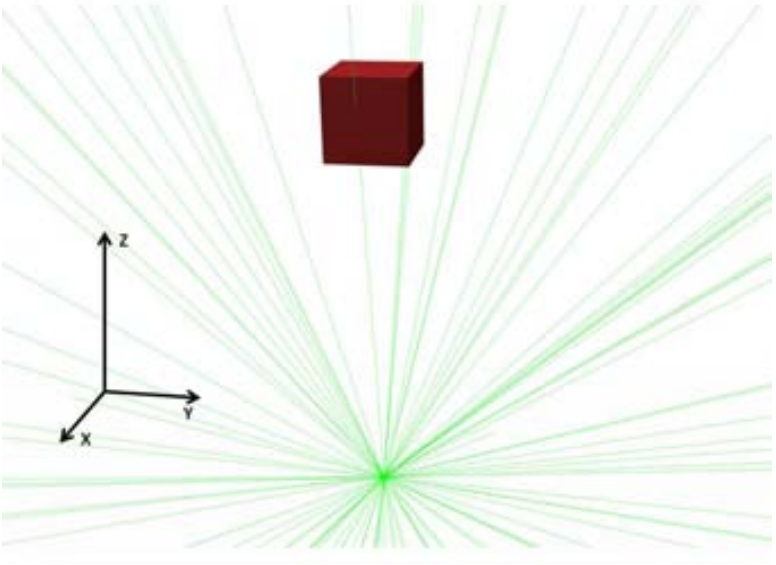

FIGURE 4.1: Visualization of the GAMOS siumlation example. The red cube corresponds to the CdTe cube and the green lines are the tracks of the hundred 511 keV gamma photons.

generated particles or generate them according to a specific energy spectrum. The time distributions allow, for instance, to fix a decay rate according to a given activity. The position distribution lets the user create the particles in a specific point or distribute the emissions in a volume. Finally, the direction distribution allows to limit the 4π emission to a fraction of the solid angle. When choosing the particle type the user can create a single particle (e.g. a photon), or a radio-isotope (e.g. ^{18}F). In the case of PET, in which the back-to-back gamma photons come from the annihilation of a positron and an electron, this last feature is especially useful as it allows to include in the simulation the physical limit to the image spatial resolution imposed by the motion of the positron.

GEANT4 provides two separated physics list categories for electromagnetic interactions[48]: the standard and the low energy lists. The standard lists[49] are specifically designed for High Energy Physics (HEP) applications (in the energy range of 1 keV to 10 PeV). They are used for MC simulations in the experiments of the Large Hadron Collider[50] (LHC) in CERN. The low energy physics lists extends the energy range down to the eV range. They are especially useful for medical MC simulations as they include the low energy effects for electrons and photons. The low energy physics lists for photons and electrons are based on the EEDL (Evaluated Electrons Data Library) [51] and the EPDL97 (Evaluated Photons Data Library) [52] respectively. In the Compton camera case these lists allow us to include the Doppler broadening effect (See chapter 2) as the Compton profiles are included in the Compton cross section of EPDL97.

Once the physics list is chosen, the generator is initialized and the logical volume

"cube_of_CdTe" is associated with the "Absorber" hit-sensitive detector for the recording of the energy depositions caused by the interactions of the crossing gammas. The next lines define a user action which consists of an independent C++ code made by the user and integrated with GAMOS. In this case it is invoking a user action developed to record the data coming from the hit-sensitive detector. We explain this user action with detail in the next section. Finally the last lines ask the generator to create a hundred 511 keV gammas at -5 mm in the Z direction of the world volume and with a time distribution given by a decay rate determined by an activity of 10^5 Bq.

These examples summarize the way in which the simulations are performed within the GAMOS framework. First, in the geometry file, one defines the geometry of the detector and the environment. Then, in the input file, one selects the physics to be included, the particles to be generated, the hit-sensitive detectors associated with logical volumes, and the user actions (if any) to be performed.

In the next section we will explain the "GmSDTTreeUA" user action which has been developed for the recording of data coming from hit-sensitive detectors into `ROOT` Trees. This user action has now been included into the 4.0 release of GAMOS.

4.1.2 Data Recording in ROOT Trees.

In order to perform in-depth analysis of the physics processes taking place in the detectors as well as to implement the detector response into the simulation we created "GmSDTTreeUA". This *user action* allows to record all the information selected by the user in `ROOT` Trees.

`ROOT`[53] is an object-oriented framework for data analysis developed at *CERN*. It allows to handle and analyze large amounts of data featuring useful C++ classes. GEANT4 and GAMOS have already integrated some `ROOT` utilities to do histograms, and other functions. One of the powerful C++ classes featured in `ROOT` is the TTree class.

The TTree class is designed to store large amount of objects of the same class. It is optimized to reduce disk space and increase access speed to the stored data. A TTree can hold any kind of data that can be constructed in C++. Its structure consists of a set of *branches* each one consisting of a list of *leafs* which contains the stored data.

In the case of "GmSDTTreeUA" each of the branches corresponds to a *hit*. A hit consists of an energy deposition inside the volume of a hit-sensitive detector. The information recorded in the leafs corresponding to each hit can be set by the user. All the physical processes from the first interaction vertex to the subsequent interactions inside the volume (due to the primary generated or secondary produced particle) can be recorded

into the TTree. In GEANT4, a hit is defined when a track deposits energy inside the logical volume associated with the hit-sensitive detector.

For our simulation the relevant information needed consists of:

- *detector ID:* which identifies the voxel in which the hit takes place.
- *interaction point:* corresponding to the center of the voxel in which the hit occurs.
- *time stamp:* defined as the moment in which the first vertex of the interaction happens.
- *deposited energy:* which includes all the energy of the interactions that composes the hit.

This minimum information can be extended with the detailed sequence of interactions and particle types that composes the hit for classification purposes.

The TTree produced by "GmSDTTreeUA" is stored in a list of files to be processed offline. In this way several analyses can be performed over the stored data without having to redo the simulation. These files serve as input for the code developed to simulate the detector response and the event selection. This code is described in the next section.

4.2 Data Acquisition Simulation and Event Selection Method.

GAMOS simulates the camera geometry and the emitted particles together with its interactions with matter, but this is just a part of what an experimental situation involves. A real detector comes with its own characteristics depending on the materials, design, electronics, etc. Moreover, when the data is acquired an event selection logic must be implemented. In order to simulate accurately the behavior of the detector, all these factors must be considered and implemented.

This section will give an overview of the signal processing involved in the read-out of semiconductor detectors. Next, it will explain how the detector response is implemented in the simulation software. Finally, the event selection logic will be explained.

4.2.1 Signal Processing in Semiconductor Detectors.

In our simulation we will focus on solid state detectors. These detectors consist of semiconductor diodes connected to a bias voltage. Like in a gas ionization chamber[54],

the incident photon ionizes the material (through one of the interactions explained in chapter 2) creating a cloud of N electron-hole pairs proportional to the deposited energy, E, of the interaction

$$N = \frac{E}{\epsilon_i}, \tag{4.1}$$

where ϵ_i is the ionization energy of the material ($\sim$ 3.6 eV for Si and $\sim$ 4.4 eV for $CdTe$ [14]). This equation is not exactly correct. Some of the energy deposited in the detector is dissipated as lattice excitations (i.e., phonons). Therefore, the number N of charge carriers generated have an intrinsic statistical fluctuation. This results in a physical limit to the detector energy resolution which is quantified by the Fano factor (see chapter 2). Moreover, the lifetime of the charge carriers in the detector is limited as holes and electrons can recombine. Impurities in the detector crystal can act as traps delaying the drift of the charge carrier or acting as recombination centers. This effect known as *trapping*, will introduce an additional source of uncertainty in the energy measure given by the detector; as some of the produced charge carriers will be lost.

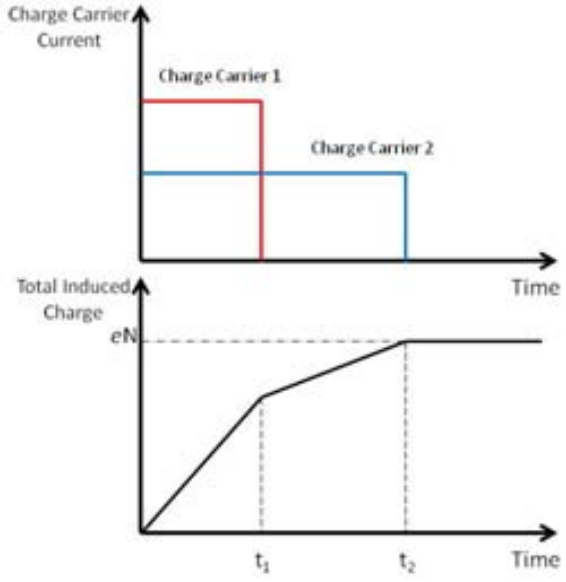

FIGURE 4.2: In the top an schematic idealization of the currents induced by the electrons and holes is shown. The total induced charge versus time is shown below.

The bias voltage applied to the detector, creates an electric field inside the material which forces the charge carriers to drift to the electrode with opposite polarity. The velocity of the electrons and holes inside the detector is constant, given by the following formula:

$$\overrightarrow{v} = \mu \overrightarrow{E}, \tag{4.2}$$

where $\overrightarrow{v}$ is the charge carrier velocity, $\overrightarrow{E}$ is the electric field, and μ is the mobility.

The electrons and holes have different mobilities μ_e and μ_h and therefore different drift velocities v_e and v_h. These mobilities depend on the material, but electrons move faster than holes as they are less bound to the atoms of the material. The time spend by the charge carrier in order to reach its corresponding electrode is determined, for a given material, by the impact point along the direction defined by the electrodes and the electric field intensity in the material.

The shape of the deposited charge over time will depend on the time spend by each of the charge carrier types to reach the electrodes. An idealize scheme of the signal shape is shown in figure 4.2. The *charge collection time* corresponds to the time needed to collect all the deposited charge eN.

From the use of terms like charge collection one might think that the signal in the detectors is produced when the charge carriers arrive to the electrode. If this were true there would be a delay between the energy deposition and the beginning of the signal. However, such delay does not exist. The signal in the electrodes begins as soon as the charge carriers start their drift. The charge is induced by the motion of the charge carriers towards the electrodes. The induced charge by a given charge cloud configuration and for a given detector geometry, can be calculated through the Shockley-Ramo theorem[55, 56].

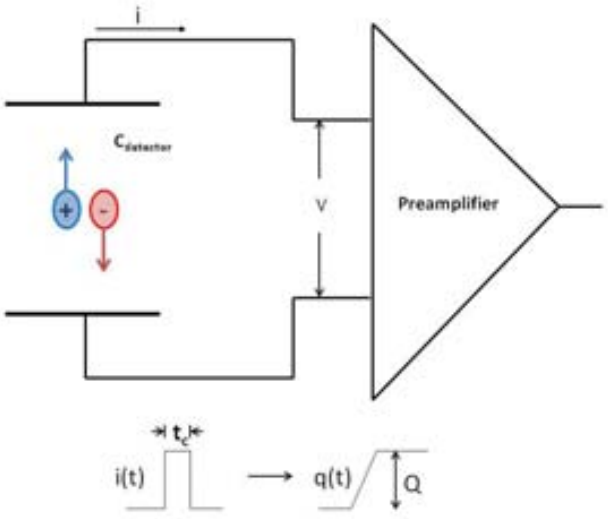

FIGURE 4.3: First step of the signal processing. The interacting gamma generates a electron-hole cloud that induces a current peak. The signal is sent to the charge sensitive amplifier that transforms it into a voltage step.

In order to read out this signal the detector is connected to a *charge sensitive amplifier* which integrates the intensity pulse producing a voltage step with a height proportional to the deposited charge (See figure 4.4). The signal passes then through a *shaping amplifier* which transforms the voltage step-like shape into a voltage pulse with a height proportional to the generated charge and, therefore, to the deposited energy. The measure of the energy is performed by digitalizing the signal with an Analog-to-Digital Converter (ADC) that provides the height of the peak.

If the charge collection time (which corresponds to the rise time of the preamplifier signal) is larger that the shaping time, then the amplitude of the shaped signal will be lower than the preamplifier signal. The difference between these two signal, called ballistic deficit [12], will result in an error on the measurement of the deposited energy. The uncertainty on the energy value will depend on the electronic noise, the precision of the ADC, and the ballistic deficit.

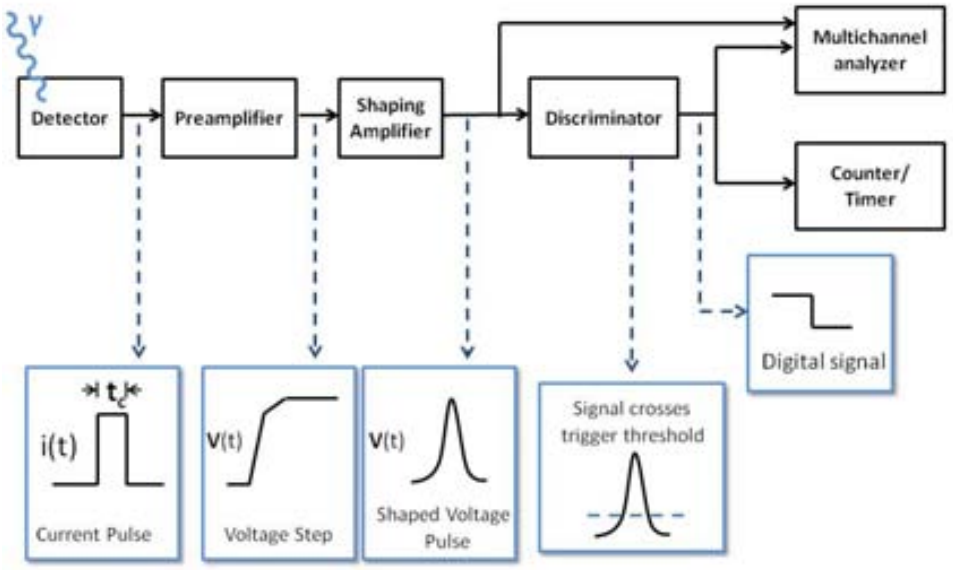

FIGURE 4.4: Generic signal processing scheme for semiconductor detectors.

In the case in which two or more detectors are operated in coincidence mode (like in PET or Compton camera), the time at which the interaction takes place is needed in order to establish if two or more energy depositions are in coincidence. To obtain the timing of a given interaction (as well as to reject noise events) a *trigger* (also called time pick-off unit) is implemented. It consists of a *discriminator* that allows the signal processing to continue if the signal is higher than a fixed voltage level (i.e., the trigger threshold)

and inhibits it otherwise. The position of the discriminator in the signal processing electronics depends on the concrete design of the detector read-out. The time at which the signal passes the discrimination level is recorded as the *time stamp* of the energy deposition.

The precision of the time stamp determines the minimum time in which two consecutive energy depositions in a given detector can be distinguished. Random noise in the signal feed in the discriminator affects the moment in which the signal crosses the trigger introducing an uncertainty in the value of the time stamp known as time jitter. The maximum count rate in the detector (i.e., the number of detected events per time unit) also is determined by the precision of the time stamp. The timing precision of the detectors is important for the Compton camera. The identification of coincidence events will depend on the timing precision, as well as the maximum activity that the tomographer can sustain before saturation.

4.2.2 Detector Response Simulation and Coincidence Event Selection.

The VIP scanners (PET, PEM and Compton camera) are made from the stacking of voxelized detectors. Each of the voxels that compose the resulting 3D array have its own integrated read-out, i.e., each voxel behaves effectively as an independent detector[1]. In order to model the response of the voxels that compose the detector we must first define some concepts:

- *Trigger hit:* energy deposition contained in a single detector voxel and above the trigger threshold. The trigger hit contains the information of the center position of the detector voxel, the deposited energy, and the time of the interaction.
- *Measuring Time:* time in which the voxel is processing a trigger hit. During this time the voxel is still responsive and will record any other energy deposition taking place, adding it to the energy of the original hit.
- *Dead Time:* time period after measuring time in which the voxel is finishing the processing of the trigger hit and preparing itself for the next trigger. During dead time the voxel is unresponsive and all energy depositions during this time will be lost (this is defined by G. Knoll[12] as *non-paralizable dead time*).

The data acquisition process begins with the activation of a voxel by a trigger hit. The time stamp of the trigger hit marks the beginning of the application of the measuring time, i.e., any other energy deposition in this same voxel is added to the energy of the

[1]This is not true in the case of the Compton camera prototype discussed in chapter 7.

original trigger hit. When the measuring time is over the dead time begins. During the dead time any energy deposition in the same voxel is not processed and thus lost. After this process takes place the time stamp, position, and energy of the resulting *hit* is recorded.

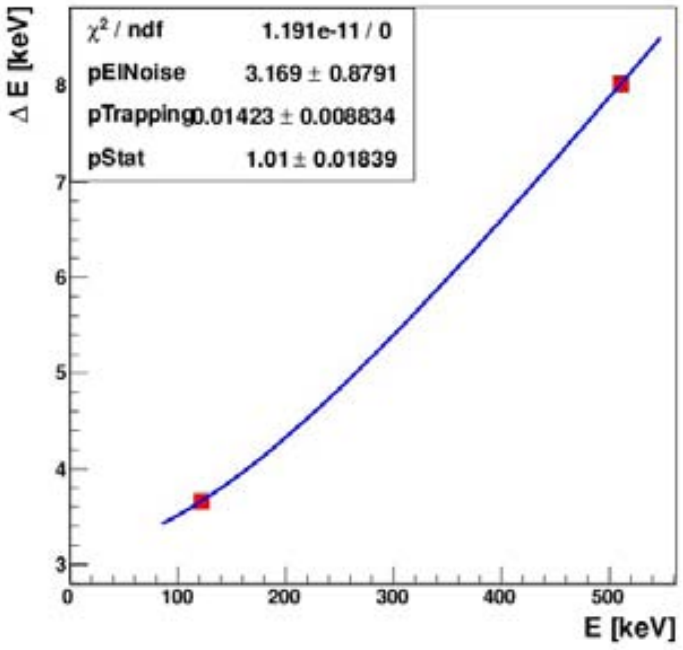

FIGURE 4.5: Function fit for the modeling of the energy resolution response of the CdTe detectors.

The energies of the hits are smeared with a factor to account for the detectors energy resolution. As explained in chapter 2, section 2.2.2.1, there are three contributions to the error ΔE of the measured energy. The error ΔE on the energy measure depends on the deposited energy and, therefore, a different smearing factor must be applied to each hit according to its energy.

In the case of the CdTe detectors the measured energy resolutions for ^{57}Co and ^{22}Na (see chapter 3, section 3.4) are fitted by the function:

$$f(E) = \sqrt{p_{stat} \cdot (2.335^2 \cdot \epsilon \cdot F \cdot E) + p_{noise}^2 + (p_{trapping} \cdot E)^2}. \tag{4.3}$$

The obtained values from the fit (see figure 4.3) are: $p_{stat} = 1.01 \pm 0.02$, $p_{noise} = 3.2 \pm 1.3$ keV, and $p_{trapping} = 1.4\% \pm 0.5\%$.

In the case of the Silicon detectors the theoretical values [17] for the Fano factor $F_{Si} = 0.115$ and $\epsilon_{Si} = 3.63eV$ are used. The contribution from the readout electronic is

supossed to be equal as is the case of CdTe (3.2 keV) and the contribution due to trapping is neglected.

The output of the above process is a list of time ordered hits from which the coincidence events must be identified. In a coincidence event, in the case of the Compton camera, the gamma photon emitted by the source travels through both the scatterer and the absorber detectors; undergoing a Compton interaction in the scatterer and a photoelectric absorption in the absorber. These two events happen simultaneously[2].

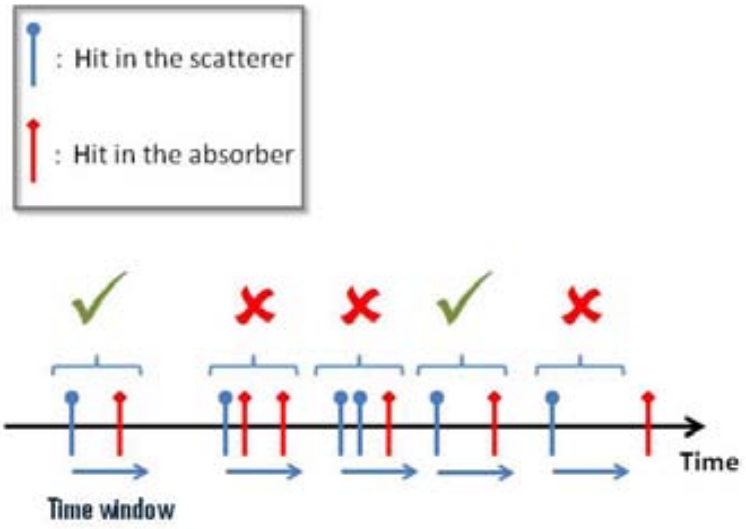

FIGURE 4.6: Scheme of the coincidence event selection method.

In order to identify a coincidence event, one must consider the difference between the time stamps of the two energy depositions. This difference should be negligible, but given the limited timing precision of the detectors its value will be randomly distributed around zero. The width of this distribution defines the *coincidence time window* which consists of the maximum time between the time stamps belonging to the energy depositions that compose a coincidence event.

[2]The time difference between the two events is far below the precision of any solid state detector. Scintillator detectors with enough timing precision to distinguish the two events do exist.

The algorithm we propose to select the coincidence events from the list of hits provided by the detector, consists of opening a coincidence time window for each scatterer hit in the list. The hits inside this time window are considered. Only in the case that there is a single absorber hit inside the window, the two hits are considered as a potential coincidence event. Finally, the hits are identified as a coincidence event and recorded for the image reconstruction, if the combined energy of the two energy depositions equals the original emission energy with an acceptance tolerance given by the detector energy resolution.

The maximum source activity that the Compton camera can sustain depends on the coincidence time window. As the source activity increases, the time between the coincidence events[3] get reduced. If the time between coincidence events is below the coincidence time window, all the hits will be rejected according to the coincidence event selection. In this case the camera is completely saturated. It is important to notice that the maximum source activity for which the camera is still not in saturated mode depends on the timing resolution of the detectors. It is this timing resolution that determines the coincidence time window and thus the maximum activity.

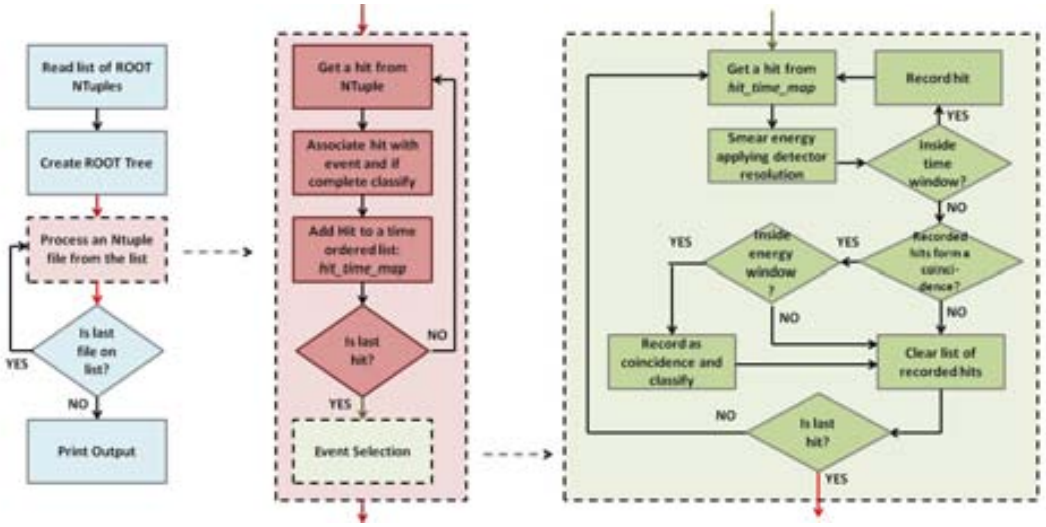

FIGURE 4.7: Flow chart corresponding to the data acquisition and event selection code that reads and processes ROOT files.

In our simulation all the physical data of the interactions inside the detectors is simulated by GAMOS and recorded into ROOT Trees (see section 4.1.2). In order to model the data acquisition and the event selection we process the data recorded on ROOT TTree using our own C++ code. First, the code loops over all the data recorded in the TTree applying the measuring and dead time window and saving the survivor hits in a time ordered list

[3]Defined by the time stamp of the scatterer energy deposition.

that we call *hit_time_map*. This first step is intended to mimic the data acquisition in the real detector.

Once the filtered data is in the *hit_time_map* the event selection takes place. The code goes through the events of the time ordered list looking for pairs of hits inside the coincidence time window according to the coincidence event selection algorithm described above. The resulting list of coincidences is recorded into a text file, ready for the image reconstruction.

In the next chapter we will explain how this list of coincidence events can be used to reconstruct the activity density of the source.

Chapter 5

Image Reconstruction.

Image reconstruction in Compton camera tomographers is a challenging task. Since the concept of Compton camera was first proposed in 1974 [2], Compton imaging has been one of the main issues to solve. The complexity of the image reconstruction, together with the computational requirements for the implementation of the image reconstruction methods, constitute some of the main reasons that prevented Compton cameras to become a suitable substitute for SPECT in current clinical practice.

This chapter gives a comprehensive overview of the different methods of image reconstruction developed for Compton imaging. We begin stating the problem that the reconstruction method must solve. Then we will describe the analytic and iterative methods proposed, and their implementation for Compton cameras made from pixelated detectors with a large number of channels.

5.1 Definition of the Problem.

The data that the Compton camera provides consist of a list of coincidence events (as explained in chapter 3). Each coincidence consists of a pair of interactions, one occurring in the scatterer, and the other in the absorber. For each coincidence event we can construct a vector $\mathbf{y}$ containing the coincidence information, i.e., the positions ($\mathbf{d}_1$, $\mathbf{d}_2$) and deposited energy (E_1, E_2) of each interaction $\mathbf{y} = \{\mathbf{d}_1, E_1, \mathbf{d}_2, E_2\}$. We can define the projection data $p(\mathbf{y})$ as the number of coincidence events sharing the same $\mathbf{y}$ vector. This projection data is generated by the gamma photons emitted by the source when they interact with the camera. If $\mathbf{x}$ is a point belonguing to the source, we can define the activity density $f(\mathbf{x})$ as the number of emitted gamma photons from the point $\mathbf{x}$ per unit time. The reconstruction of the source image consists of obtaining the

activity density $f(\mathbf{x})$ from the projection data $p(\mathbf{y})$ provided by the camera. From now on we will use image as a synonym of activity density.

The process of obtaining an estimation of the image $f(\mathbf{x})$ from the projection data $p(\mathbf{y})$ is called *back-projection* or *deconvolution*. The inverse process consisting of obtaining an estimation of the projection data from an estimation of the image is refered as *forward-projection*.

In order to obtain the image from the projection data several approaches exist. We can classify them in two categories: the analytic and the iterative methods.

The analytic methods intent to reconstruct the image directly by solving the equations that relate the projected data with the image (see section 5.2). The iterative methods use statistical algorithms in order to perform the reconstruction (see section 5.3). The most important challenge for both kind of methods is the computational power needed.

Although Anger cameras and Compton cameras are SPECT technologies, there are important differences in the data produced by the two. This makes the direct application of analytic imaging reconstruction techniques developed for Anger camera based SPECT systems imposible. The search for analytic reconstruction methods for Compton cameras is important to gain insight in the nature of the image reconstruction problem. In the analytic methods the projection data is understood as a convolution of the image with an integral kernel [57] which depends on the coincidence event probability. If we define $h(\mathbf{y}, \mathbf{x})$ as the conditional probability of a photon emitted from $\mathbf{x}$ to produce a coincidence event with vector $\mathbf{y}$, then the projected data and the image are related by the following integral equation:

$$p(\mathbf{y}) = \int_X h(\mathbf{y}, \mathbf{x}) f(\mathbf{x}) d\mathbf{x} = (\mathcal{H}f)(\mathbf{y}), \tag{5.1}$$

where X is the whole image space. The projection data is therefore the result of applying the convolution operator $\mathcal{H}$ with kernel $h(\mathbf{y}, \mathbf{x})$ to the image f($\mathbf{x}$). The aim of the analytic image reconstruction methods is the development of expressions for $h(\mathbf{y}, \mathbf{x})$ that allow the calculation of the inverse operator $\mathcal{H}^{-1}$ to perform the deconvolution and obtain $f(\mathbf{x})$.

The iterative methods can be applied with few modifications to all kind of nuclear medicine scanners like PET, PEM, SPECT and Compton camera. These methods are based on statistical iterative algorithms that converge to the most probable configuration of the image given the projection data. If the image and detector space are segmented into voxels, one can approximate equation (5.1) by the following vector equation:

$$\mathbf{p} = \mathbf{H}\mathbf{f}^T. \tag{5.2}$$

Now $\mathbf{f}$ and $\mathbf{p}$ are vector whose elements g_i and f_j are the values corresponding to the i-th and j-th bins in their respective spaces. In this approximation the linear operator $\mathcal{H}$ becomes the matrix H, which is usually refered as projection or transition matrix.

This discrete approach allows to simplify the reconstruction problem and is especially useful for pixel detectors in which the data regarding the interaction position is already given in a segmented way. In the case of Compton camera each of the components of $\mathbf{p}$ consists of the number of recorded coincidence events with a given combination of a particular bin in the scatterer detector, a particular bin in the absorber detector, and a given scattering angle. The equation (5.2) allow the implementation of statistical algorithms (like expectation maximization) to provide an estimation of the $\mathbf{f}$ values.

5.2 Analytic Methods.

As has been explained in the previous section the nature of the data collected in SPECT, PET and PEM system is different than the data that Compton cameras provide. In a SPECT system the emission point of each of the detected gamma photon is bound to be on a line[1] known as *Line Of Response* (LOR) and the same is true for the detected back-to-back photons in the PET and PEM case. On the other hand, in a Compton camera the emission point of each gamma photon producing a coincidence event can only be determined to be on a conic surface, that is called *Region Of Response* (ROR). This intrinsic difference prevents the straight forward application of the analytic image reconstruction methods developed for SPECT, PET and PEM to Compton camera scanners.

We begin this section by describing the foundations of the analytic image reconstruction for SPECT (which is formally identical in PET and PEM) and the most used reconstruction method: the filtered back-projection. After this we explain a back-projection image reconstruction method for Compton cameras and finally the research developments towards an analytic image reconstruction method for Compton imaging.

5.2.1 Overview of Analytic Image Reconstruction in SPECT.

In an Anger camera the detected photons have been previously collimated mechanically by a thick material with apertures that only allow the pass of photons coming from a specific direction. In this way we have a LOR for each gamma photon where the distribution of the LORs depends on the collimator characteristics. The most usual case

[1] Assuming that the photons do not undergo any interaction before reaching the detector.

is the parallel hole collimator in which the gammas are collimated along parallel lines, perpendicular to the detector surface. The data collected by the Anger camera consist of projections of the source activity into the detector plane.

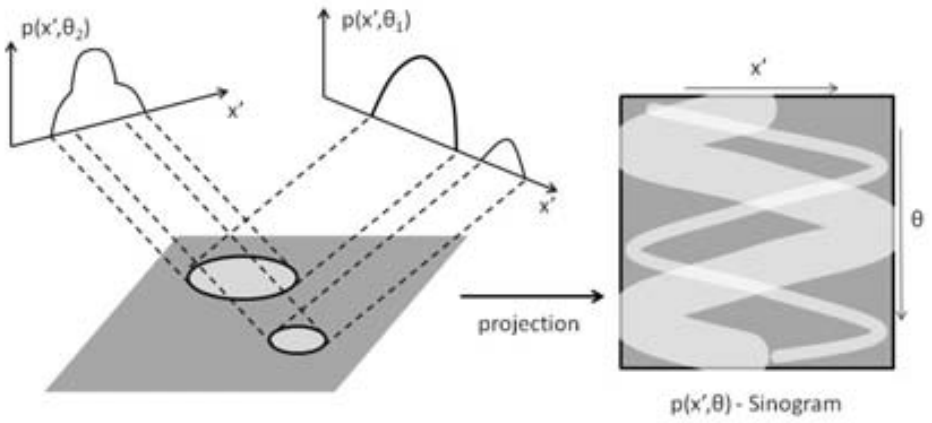

FIGURE 5.1: The projections at different θ angles are obtained by integrating along parallel LORs. A sinogram consists of the representation of the projections $p(x', \theta)$ on the $x' - \theta$ plane.

For a given position of the Anger camera with respect to the source, the projection (also called ray sum, line integral, and Radom transform) is obtained by the sum along the directions perpendicular to the collimator surface of the detected gamma photons. Restricting ourselves to the 2D case[2], we can define $f(x, y)$ as the source activity in a given point. The projection of $f(x, y)$ for a given angle θ (with respect to the x-y axis) is defined mathematically by

$$\begin{aligned} p(x', \theta) &= \int_{-\infty}^{+\infty} \int_{-\infty}^{+\infty} f(x, y)\delta(x\cos\theta + y\sin\theta - s)dxdy \\ &= \int_{-\infty}^{+\infty} f(x'\cos\theta - y'\sin\theta, x'\sin\theta + y'\cos\theta)dy', \end{aligned} \tag{5.3}$$

where the (x', y') coordinates are obtained from a counter-clockwise rotation of the x-y axis through an angle θ. The concept is illustrated in figure 5.1 where a representation of the projection of a point in the x'-θ plane is shown. As can be easily proven the

[2]The 3D case can be obtained by applying the methods discussed below to the different planes of the image. Direct 3D methods do exist but they are out of the scope of this thesis.

Radon transform of a point is a sinusoidal function in the x'-θ plane. For this reason such representation is called sinogram.

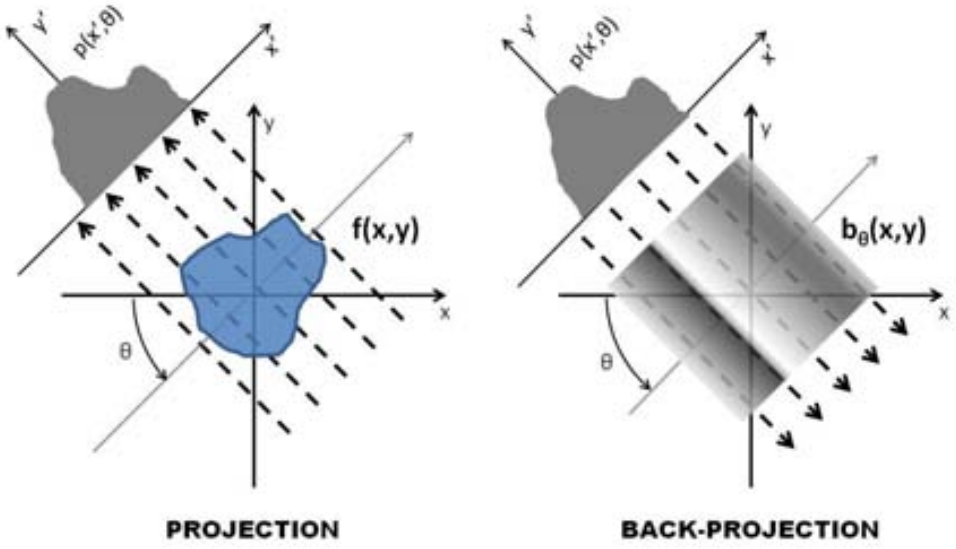

FIGURE 5.2: Illustration of the projection and back-projection concepts. *Left:* The projection of the image in one direction is obtained by the sum along the directions perpendicular to the collimator surface of the detected gamma photons. *Right:* The back-projection consists of assigning the projection values to the points of the image space.

As the Anger camera of a SPECT system is rotated, a projection $p(x', \theta)$ is obtained for each one of the camera positions. Hence, the SPECT system projects the source activity map $f(x, y)$ along various angles, with projections $p(x', \theta)$ (i.e., forward-projection). The purpose of the image reconstruction is then to inverse this projection (i.e., back-projection) in order to obtain the image $f(x, y)$ of the activity.

A straightforward back-projection method consists of assigning, for each direction θ, the projected values to all the points of the image space. We define $b_\theta(x, y)$ as the image resulting from the back-projection of $p(x', \theta)$ for a single θ angle. Each projection $b_\theta(x, y)$ can be viewed as a single band along one particular direction, as shown in figure 5.2. This is the same as taking the single value for $p(x', \theta)$ for all bins in y' of $b_\theta(x', y')$, and can be described as:

$$b_\theta(x, y) = p(x', \theta) \; \forall y'. \tag{5.4}$$

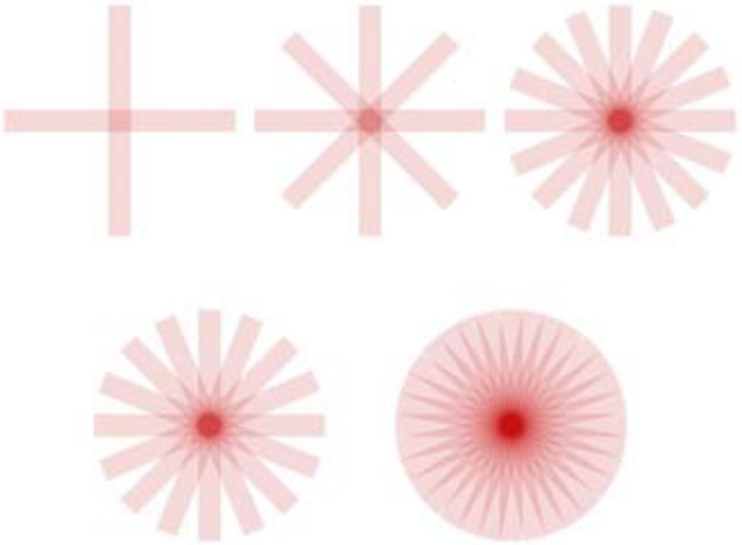

FIGURE 5.3: Images of a disk reconstructed through the sum of different back-projections $b_\theta(x, y)$. The first image is reconstructed with two back-projections and the successive images increase this number by a factor of two. The resulting image of the point is blurred as no filter is applied.

The back-projected image $b(x, y)$ is obtained by the sum of the back-projections in all directions:

$$b(x, y) = \int_0^\pi d\theta b_\theta(x, y) = \int_0^\pi d\theta p(x', \theta). \tag{5.5}$$

This is illustrated in figure 5.3, where the image of a disk is reconstructed by the addition of an increasing number of back-projections $b_\theta(x, y)$. It is important to note that the back-projection $b_\theta(x, y)$ is not the inverse of the projection $p(x', \theta)$, i.e., the image $f(x, y)$ is not obtained by the sum of the back-projections. As can be seen in figure 5.3, the resulting image $b(x, y)$ is a blurred version of the original.

The relation between the projections and the image is established by a mathematical theorem, usually called *Central Slice Theorem*, which states that the Fourier transform of a given projection is equal to a central slice perpendicular to the projection direction of the Fourier transform of the image (see figure 5.4). The Central Slice Theorem is the foundation of tomographic imaging in PET, SPECT, and PEM. A proof of the theorem in two dimensions can be found in appendix A.

In order to study the relation between the back-projected image and the image itself we must compute its Fourier transform[3] to take advantage of the Central Slice Theorem. By computing the Fourier transform of $b_\theta(x, y)$ and using equation (5.4) we can obtain

[3]We will use the following notation for the Fourier transform: $F(\omega_x, \omega_y) = \mathcal{F}_2\{f(x, y)\}$ is defined as the two dimensional Fourier transform of $f(x, y)$.

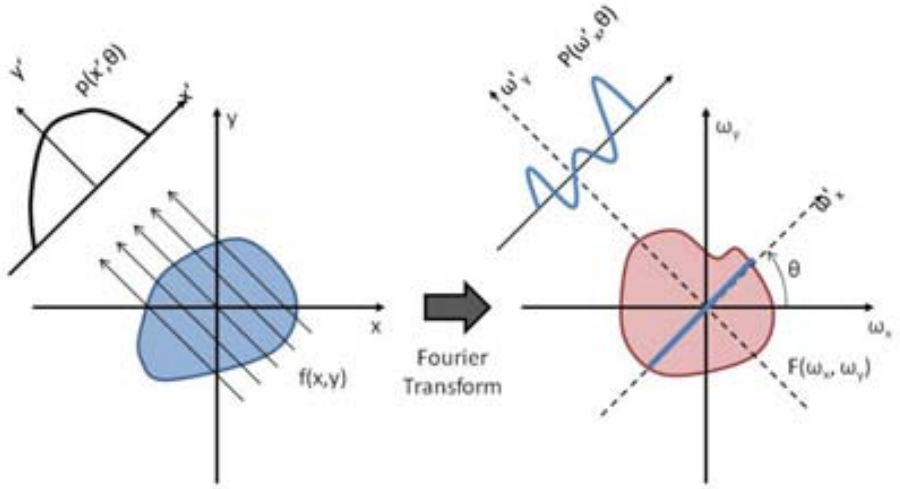

FIGURE 5.4: Illustration of the Central Slice Theorem in two dimensions. The Fourier transform of the projection is equal to a central slice perpendicular to the projection direction of the Fourier transform of the image.

the following relation:

$$\begin{aligned} B_\theta(\omega_x, \omega_y) &= \int_{-\infty}^{+\infty} \int_{-\infty}^{+\infty} b_\theta(x,y) e^{-i2\pi\omega_x x} e^{-i2\pi\omega_y y} dx dy \\ &= \int_{-\infty}^{+\infty} \int_{-\infty}^{+\infty} p(x',\theta) e^{-i2\pi\omega'_x x'} e^{-i2\pi\omega'_y y'} dx' dy' \\ &= \int_{-\infty}^{+\infty} p(x',\theta) e^{-i2\pi\omega'_x x'} \delta(\omega'_y) dx' \\ &= P(\omega'_x, \theta)\delta(\omega'_y), \end{aligned} \tag{5.6}$$

where we used the definition of the Dirac delta function: $\delta(x) = \int_{-\infty}^{+\infty} e^{-i2\pi\omega x} dw$.

Applying the Central Slice Theorem on equation (5.6) we obtain:

$$B_\theta(\omega_x, \omega_y) = F(\omega_x, \omega_y)\delta(\omega'_y). \tag{5.7}$$

The meaning of this equation is that the back-projection in a given direction only has information of the central slice perpendicular to the projection direction. This result is an expected consequence of the Central Slice theorem.

If we expand the Dirac delta function[4] and integrate over the θ we obtain the important result:

$$B(\omega_x, \omega_y) = \frac{F(\omega_x, \omega_y)}{\omega}, \tag{5.8}$$

where $\omega = \sqrt{w_x^2 + w_y^2}$.

Equation (5.8) establishes that the Fourier transform of the back-projection image is equal to the Fourier transform of the image weighted by the inverse distance to the origin. Therefore, the image $f(x, y)$ can be obtained by *filtering* the Fourier transform of the back-projection image $B(\omega_x, \omega_y)$ with the conic filter ω and then computing the inverse Fourier transform, i.e.,

$$f(x, y) = \mathcal{F}_2^{-1}\{\omega B(\omega_x, \omega_y)\}. \tag{5.9}$$

This method is known as back-projection filtering (BFP) as the projection data is first back-projected and then filtered in the Fourier space in order to obtain the image. BFP involves 2D Fourier transforms, a more computationally efficient alternative can be obtained by inverting the order of the filtering and the back-projection.

5.2.1.1 Filtered Back-Projection Algorithm.

Filtered Back-Projection (FBP) is the most commonly used analytical image reconstruction method in SPECT, PET, and PEM scanners. In FBP the image is obtained as the sum of filtered projections for all the θ directions. As in the case of BFP, the filter (a ramp filter in this case) is applied in the Fourier space. The filtered projection $p^F(x', \theta)$ is obtained by inverse Fourier transform according to

$$p^F(x', \theta) = \mathcal{F}_1^{-1}\{|\omega_x'| P(\omega_x', \theta)\}. \tag{5.10}$$

The back-projection of the filtered projections is equal to the image

$$f(x, y) = \int_0^{\pi} p^F(x', \theta) d\theta. \tag{5.11}$$

Equation (5.11) can be derived in a more direct way by calculating the Fourier transform of the image $f(x, y)$ using polar coordinates in the Fourier space ($\{\omega_r, \omega_\phi\}$ rather than

[4] We use the identity $\delta(f(x)) = \sum_i \frac{\delta(x - x_i)}{|f'(x)|} \; \forall x_i | f(x_i) = 0$.

$\{\omega_x, \omega_y\}$):

$$f(x,y) = \int_0^{2\pi} \int_0^{\infty} F(\omega_r, \omega_\phi) e^{i2\pi\omega_r(x\cos\omega_\phi + y\sin\omega_\phi)} \omega_r d\omega_r d\omega_\phi. \tag{5.12}$$

By using the relation $F(\omega_r, \omega_\phi + \pi) = F(-\omega_r, \omega_\phi)$ and exchanging $\omega_r d\omega_r$ by $|\omega_r| d\omega_r$ we can change the range of the integrals obtaining

$$f(x,y) = \int_0^{\pi} \int_{-\infty}^{+\infty} F(\omega_r, \omega_\phi) e^{i2\pi\omega_r(x\cos\omega_\phi + y\sin\omega_\phi)} |\omega_r| d\omega_r d\omega_\phi. \tag{5.13}$$

By realizing that $\omega_r = \omega'_x$, $x' = x\cos\omega_\phi + y\sin\omega_\phi$, and by using of the Central Slice Theorem, we finally obtain:

$$f(x,y) = \int_0^{\pi} \int_{-\infty}^{+\infty} |\omega'_x| P(\omega'_x, \theta) e^{i2\pi\omega'_x x'} d\omega'_x d\theta. \tag{5.14}$$

The FBP image reconstruction method can be summarized in the following steps:

1. Compute the Fourier transform of each projection.
2. Apply a ramp filter $|\omega'_x|$ to the projections in Fourier space.
3. Calculate the filtered projection $p^F(x', \theta)$ by inverse Fourier transform.
4. Obtain the image as the back-projection of the filtered projections for all the θ directions.

FBP involves the computation of 1D Fourier transforms making it a more efficient method from a computational point of view than BFP (where 2D Fourier transforms must be performed).

5.2.2 Back-Projection of Cones from Compton Camera Data.

Simple back-projection of Compton cones calculated from the coincidence events is the simplest aproach to the Compton imaging problem. Assuming that the energy deposition in the scatterer is due to a Compton interaction, one can use the Compton kinematics (see chapter 2) to reconstruct a cone surface on which the source location lies. If two gammas emitted from the same point produce each a coincidence event, the two corresponding cones will intersect in the emission point of the photons.

A method of back-projection imaging consists of the segmentation of the source space into voxels and the computation of the number of cones intersecting each of them.

However, this method will construct blurred images, given that the cones that intersect in the emission point will also contribute to the voxels around it. In figure 5.5 we show the image resulting from the back-projection of four cones in a segmented 2D plane.

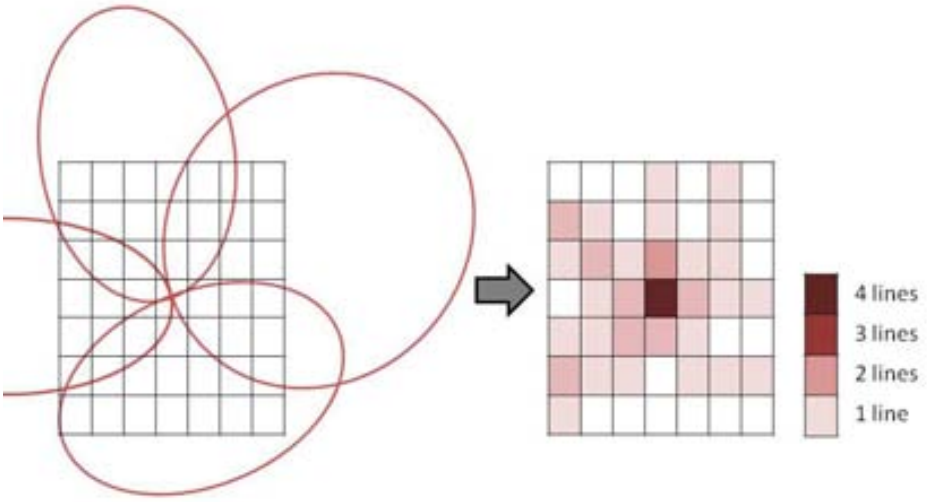

FIGURE 5.5: 2D image of a point-like source reconstructed through the back-projection of four cones into the image plane.

The computation of the intersection of a cone surface with a 3D segmented space is a complex problem by itself. We will outline in the following the method proposed by Wilderman[58] for the back-projection of cones on a segmented 2D image plane. The 3D case can be obtained by applying the method to each individual plane of the image space.

The intersection of a cone with a plane is an ellipse. If the plane is perpendicular to the z axis and located on $z = z_0$, the ellipsis must fulfill the following relation:

$$[n_x(x-x_S)+n_y(y-y_S)+n_z(z_0-z_S)]^2 = \cos^2\theta\cdot[(x-x_s)^2+(y-y_s)^2+(z_0-z_s)^2]. \quad (5.15)$$

Here, (x_S, y_S, z_S) corresponds to the coordinates of the Compton interaction in the scatterer, θ to the Compton scattering angle, and (n_x, n_y, n_z) to the coordinates of a unit vector along the cone axis direction.

The first step in the method consists of the computation of the intersections of the ellipsis with the edges of the segmented image space. The number of intersections can

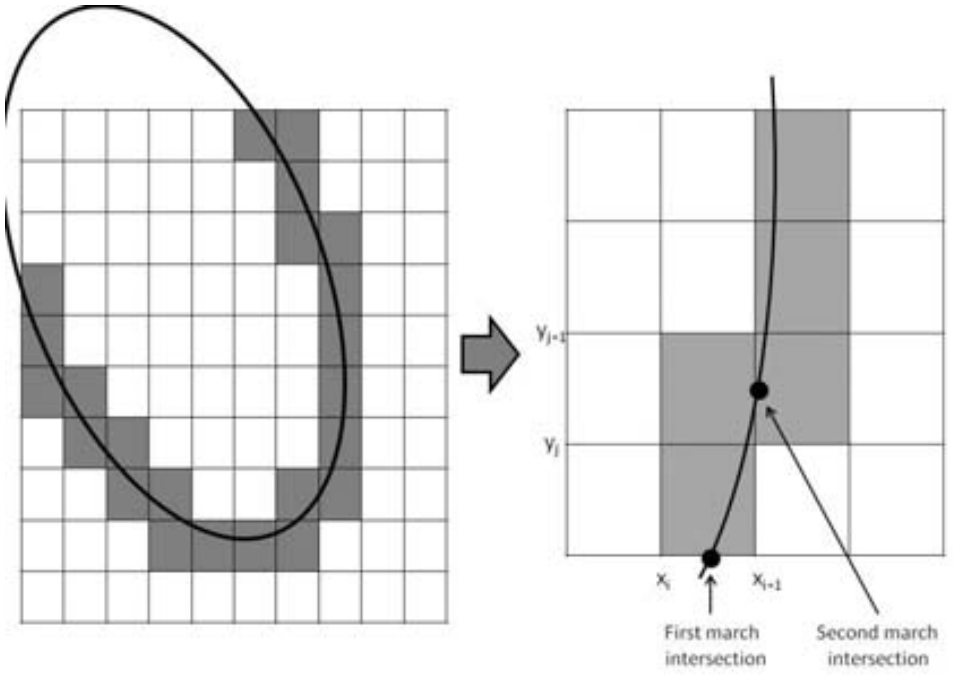

FIGURE 5.6: Illustration of the marching method.

be either 0,2,4,6 or 8 which will result into a full ellipsis or 1, 2, 3 or 4 arcs crossing the image plane respectively. Wilderman [58] classifies these cases into 6 possible scenarios.

Rules are specified to *march* through the arcs identifying the pixels that are crossed. To illustrate this (see figure 5.6), consider the following example: we begin the march from an intersection with one of the edges corresponding to the x axis. If the intersection point is between x_i and x_{i+1}, then we look for the intersections of the arc with the grid lines defined by x_i and x_{i+1}. If, for instance, the arc intersects the line x_{i+1} in a point between the y_j and the y_{j+1} then it must cross all the pixels from the edge until y_{j+1}, in between x_i and x_{i+1}.

By the application of this method to each slice in z of the image one can identify all voxels belonging to a back-projected cone surface. This list can be used later for some iterative methods as explained in section 5.3.

5.2.3 Analytic reconstruction methods for Compton Cameras.

For SPECT, PET and PEM scanners we have shown that there are analytic image reconstruction methods which allow to solve the reconstruction problem in a relatively simple and computationally efficient way. This is not true for Compton cameras. Since

the original proposal of the Compton camera, various analytic image reconstruction methods have been suggested.

In 1994 Cree and Bones[59] gave a solution to the 3D source image reconstruction for a special geometry, consisting of two parallel detectors with a parallel hole mechanical collimator in between. The collimator is included in order to allow the pass of only the photons orthogonal to the scatterer plane. To recover the full 3D source distribution through this method, all scattering angles must be used; thus an infinite detector is needed.

More recently Basko[60] first, and Parra[61] later, propose two similar methods. In both methods each scatterer detector element is at the center of a spherical absorber detector. If we define the angular projections as the number of photons that arrive to the scatterer element from a given direction and undergo scattering in a given angle, then under the previous assumption the angular projections can be expanded into a series of spherical harmonics. Each of the two methods propose different schemes in order to recover the image from the angular projections. We will not explain in detail these methods as they are difficult to implement for a Compton camera with large number of channels. Some of the problems of the implementation are:

1. An image must be reconstructed for each scatterer element. This makes the methods more resource demanding as the number of elements increases and, thus, the method is impossible to implement for a large number of scatterer elements.

2. There is no computationally efficient method for the inversion of the angular projection expansion.

3. The assumptions made for the expansion to be valid are not fulfilled by the voxels in the scatterer. As the scatterer detector is supossed to have an infinite size.

Iterative methods are more computationally efficient and can be easily adjusted to the particularities of the detectors as explained in section 5.3.

5.3 Iterative Methods.

Iterative methods use statistical algorithms in order to give, in each iteration, an estimation of the image of the real source activity distribution. They are of general application (with few modifications) to all emission tomography scanners, can be easily adjusted to the particularities of the detectors, and impose no restrictions to the scanner geometry.

In the case of Compton cameras, iterative methods become the only viable alternative to a simple back-projection of cones. The main drawback of these methods is the need of high computational power. This situation will prevent some of the methods to be applied to Compton cameras with large number of channels. Nevertheless solutions have been proposed to speed up (Ordered Subset approach) and reduce the computation resources consumed (List Mode methods).

All the methods that we will describe in the following begin with a segmentation of both the imaging space and the projection data. As explained in section 5.1 this implies that the convolution equation (5.1) becomes the vector equation (5.2), which is a system of linear equations. The segmentation of projection data adapts perfectly to the detectors that we will discuss as they are already segmented into pixels.

In the following sections we will give an overview of the most commonly used iterative methods for Compton cameras with emphasis on the ones that have been implemented for the analysis presented in this thesis.

5.3.1 Algebraic Reconstruction Technique.

The Algebraic Reconstruction Technique (ART) was first proposed by the Polish mathematician Stefan Kaczmarz [62] to solve systems of linear equations. Later it was rediscovered by Gordon[63] to solve the image reconstruction problem in Electron Microscopy and X-Ray photography.

ART begins with an initial guess of the image: $\hat{\mathbf{f}}$. Then equation (5.2) is used to forward-project the image in order to obtain an estimation of the projection data $\hat{\mathbf{p}}$. The estimation of the projection data $\hat{\mathbf{p}}$ is then compared with the real projection data $\mathbf{p}$ and used to update the image estimation. The process continues until the desired level of convergence is achieved.

The update of the image estimation $\hat{\mathbf{f}}$ depends of the implementation of ART. In the additive implementation the update is performed by adding the difference $\Delta = \mathbf{p} - \hat{\mathbf{p}}$ to the image estimation, with a weighting factor given by the projection matrix $\mathbf{H}$. This is realized through the formula:

$$\hat{f}_i^{k+1} = \hat{f}_i^k + \frac{\sum_j H_{ij}\Delta_j^k}{\sum_{i,j} H_{ij}}. \tag{5.16}$$

Where $\hat{f}_i^k$ is the i-th component of the image estimation for the k-th iteration, Δ_j^k is the j-th component of the difference between estimated and real projections for the k-th iteration, and H_{ij} is the i-th row and j-th column element of the projection matrix. As

the values of f_i are constrained to be positive the above formula must be modified giving

$$\hat{f}_i^{k+1} = max[0, \hat{f}_i^k + \frac{\sum_j H_{ij}\Delta_j^k}{\sum_{i,j} H_{ij}}]. \tag{5.17}$$

ART is a very intuitive method but is not suited for an implementation in Compton cameras with large number of channels. The size of the projection matrix, the image vector, and the projection data vector is too big to be handled by today computers.

5.3.2 Origin Ensemble Algorithm.

The Origin Ensemble algorithm[5] (OE) is a novel image reconstruction method initially proposed by Sitek[64], and further developed for its application in Compton cameras by Andreyev[65].

In OE the image is defined as an ensemble of emission points. In each iteration OE gives an estimation of the origin point of each of the emitted gamma photons of the coincidence event sample. The ensemble state in the k-th iteration is defined by the vector Y_k, which consists of the estimation of the 3D positions of the emission origin points of the photons producing the coincidence events. Each of the emission points composing Y are bound to lie on their corresponding RORs. In the case of the Compton camera the ROR corresponds to the back-projected cone surface.

For the initialization of the algorithm, Y_0 is obtained by picking random positions L_0 on the conic surfaces of all events. The next iterative procedure is applied to each of the coincidence events:

1. A new location L_{k+1} is randomly selected on the cone surface.
2. L_{k+1} is accepted to be the origin point for this photon for the iteration $k+1$ with probability P. The acceptance probability P is obtained by the comparison of the origin point density, D_{k+1} at the new location, with the density D_k at the old location:
$$P(Y_k \to Y_{k+1}) = min[1, \frac{D_{k+1}+1}{D_k}] \tag{5.18}$$
3. If L_{k+1} is accepted, then it is recorded in Y_{k+1} as the new origin estimation for this photon and the density matrix D is updated accordingly. If it is rejected then the old location L_k is kept instead.

[5] Originally known as Stochastic Origin Ensemble algorithm.

In our implementation for the Compton camera, for each iteration, the random positions in the cones are obtained following these steps:

1. Compute a random vector along a cone pointing along the z-axis with an aperture angle equal to the back-projected cone corresponding to the given coincidence event.
2. Rotate the cone (and the vector) into the direction of the Compton cone and shift the cone apex position to the corresponding position of the Compton cone.
3. Compute a random position along the line defined by the vector.

The only constraint to the random position obtained is that it must be inside the image FOV.

The Doppler broadening effect together with the detectors finite, spatial and energy, resolution (see section 2.2.2), will prevent OE to fully converge to the real source location. The Compton cones corresponding to a unique emission point will not intersect in this point because of the angular error in the back-projected cones. A *resolution recovery* mechanism has been proposed [66] in order to incorporate the angular errors into OE. The mechanism consists of giving to each cone surface a thickness which will depend on the angular error of cone, and hence more locations will be accepted as candidates for the photon origin.

OE is straightforward to implement for any emission tomography scanner and converges relatively fast compared with other iterative methods. We have implemented OE in our simulation and tested its performance for PET[67], and Compton camera based on VIP detectors [33, 68]. OE will be one of the image reconstruction methods used in chapters 6 and 7.

5.3.3 Expectation Maximization Methods.

The Expectation Maximization algorithm (EM) is an iterative statistical method which allows to find, for a given statistical model, the parameters which have maximum likelihood probability. Although is has been used by many authors to solve specific problems, the method was first explained and named by Dempster in 1977[69].

In EM the parameters Θ of a statistical model are estimated from a set of observed data X, when a set of unobserved data Z is present. The *likelihood function* of such a statistical model $L(\Theta; X, Z)$ is defined as the conditional probability of obtaining the data $\{X, Z\}$ given the parameters Θ, i.e., $L(\Theta; X, Z) = p(X, Z|\Theta)$. The objective of

EM is to maximize the *marginal likelihood function* $L(\Theta; X) = \sum_Z L(\Theta; X, Z)$, i.e., the conditional probability of Θ given X.

EM begins with an initial estimation of the parameters: $\hat{\Theta}_0$. In each iteration a new set of $\hat{\Theta}_k$ values is obtained by the following two step iterative process:

- **Expectation step (E-step):** Compute the function $Q(\Theta|\hat{\Theta}_k)$:

$$Q(\Theta|\hat{\Theta}_k) = E_{\hat{\Theta}_k|X}[\log L(\Theta; X, Z)], \tag{5.19}$$

  which is the expectation value of the log-likelihood function for the estimated values $\hat{\Theta}_k$, given the observed data X.

- **Maximization step (M-step):** Find the value that maximizes $Q(\Theta|\hat{\Theta}_k)$ and use it as the parameters estimation for the next iteration, i.e.,

$$\hat{\Theta}_{k+1} = \arg_\Theta \max Q(\Theta|\hat{\Theta}_k). \tag{5.20}$$

Rather than a concrete recipe, EM provides a method to construct algorithms in order to solve specific problems of parameter estimation. Some of the most successful iterative reconstruction techniques in emission tomography are based on EM. In the following sections we will describe some of these methods for the particular case of Compton imaging.

5.3.3.1 Maximum Likelihood Expectation Maximization.

The emission of a gamma photon from a radioactive source is a random process. The activity density of each of the image voxels f_j has to be understood as the mean value of the number of emitted gamma photon. As a consequence the projection data components p_i are also random variables. The image reconstruction problem can thus be seen as an statistical parameter estimation problem. The objective is the estimation of the f_j parameters given the projection data p_i, and the unknown real number of emitted photons from each voxel. It is in this context that EM can be applied to solve the image reconstruction problem.

Each of the projection data elements p_i follow a Poisson distribution. The probability of observing p_i coincidence events for a given combination i of scatterer and absorber voxels, is given by

$$P(p_i|\mathbf{f}) = \frac{\bar{p}_i^{p_i}}{p_i!} e^{-\bar{p}_i}, \tag{5.21}$$

where $\bar{p}_i$ is the mean value of detected coincidence events in the i-th combination.

If the scatterer and absorber voxel combinations are independent between them, we can write the likelihood function $L(\mathbf{f};\mathbf{p})$ as

$$L(\mathbf{f};\mathbf{p}) = \prod_i \frac{\bar{p}_i^{p_i}}{p_i!} e^{-\bar{p}_i}. \tag{5.22}$$

The Maximum Likelihood Expectation Maximization (MLEM) algorithm uses the EM method in order to provide an iterative solution to the problem of finding the f_i values that maximizes (5.22). The algorithm, proposed by Shepp[70], consists of the application of the following iterative formula:

$$f_j^{k+1} = \frac{f_j^k}{\sum_i^N H_{ij}} \sum_i^N \frac{p_i H_{ij}}{\sum_l H_{il} f_l^k}, \tag{5.23}$$

where j is a given image bin and k index refers to the iteration, and N is the number of measurement bins.

The algorithm starts with an initial estimation of the image $\mathbf{f}^0$. The recursive equation (5.23) is repeated for each iteration. The method defined by the above formula is of general application in ET. But, while in PET or SPECT scanner the sums over i are sums over bins, in the case of the Compton camera each i represents a possible combination of scatterer and absorber voxels.

The transition matrix H_{ij} is defined as the probability that a gamma photon emitted from the source voxel j produce a coincidence event simbolicaly represented by i. Therefore $\mathbf{H}$ contains all the physics happening in the scanner, the effects of the electronics, and the characteristic of the detectors used. The transition matrix can be obtained by direct measurement of the real scanner, MC simulation or by a theoretical model.

Due to the complexity of the modelization of $\mathbf{H}$ in the case of Compton cameras, Wilderman[71] proposed an approximation for H_{ij} in order to reduce the computational resources needed to implement MLEM. In this approach a perfect angular resolution and a uniform sensitivity is assumed for the detectors. As a consequence the possible emission locations in the image space are reduced to the voxels which are intersected by the back-projected cone of the corresponding coincidence event. The elements of the transition matrix are approximated to be proportional to the area of the cone surface that crosses the image voxel[6].

Like in the case of ART (see 5.3.1) the MLEM method for Compton cameras described above would require an unrealistic large computer memory. In the following sections

[6] If a 2D approach is taken, a line integral over the part of the ellipsis that crosses the image pixel must be calculated instead.

we will explain some of the developments achieved in order to increment MLEM speed (Ordered Subset Expectation Maximization method) and the computational power requirements (List Mode).

5.3.3.2 Ordered Subset Expectation Maximization.

The *Ordered Subset Expectation Maximization* (OSEM) was proposed by Hudson[72] in order to accelerate the convergence of the MLEM algorithm. In OSEM the projection data is divided in ordered subsets. Each subset consists of a partition of the projection data according to a criteria fixed by the algorithm user. The criteria provide the ordering rule for the subsets. For each iteration the MLEM algorithm is applied to each of the subsets in such a way that the output image estimation from one subset is used as input for the next one. Several partition criteria can be realized simultaneously in such a way that the sets given criteria 1 can be further partitioned by criteria 2. MLEM algorithm is applied to the subsets of the last criteria in the ordering hierarchy. In the case of the Compton camera, the simplest approach is to split the list of coincidence events provided by the camera into an ordered list of sets. More elaborated criteria can be used to order the projection data according to the a given set of scattering angle ranges.

The OSEM algorithm can be outlined as follows:

- For each k iteration:
  - For each subset S_n:
    - Apply MLEM to subset S_n:

$$f_j^{k+1} = \frac{f_j^k}{\sum_i H_{ij}} \sum_{i}^{\text{Measurement bins in } S_n} \frac{p_i H_{ij}}{\sum_l H_{il} f_l^k}.$$

  - End Loop over subsets.
- End iteration.

OSEM allows to increase the speed of the MLEM algorithm but does not reduce the computational power required and therefore cannot be implemented for Compton cameras with large number of channels.

5.3.3.3 List Mode Maximum Likelihood Expectation Maximization.

The implementation of MLEM or OSEM is impossible for Compton cameras with large number of channels. In the case of the Compton camera, the sums over the projections

space go over all the possible combinations of scatterer and absorber voxels. At the same time, the size of the transition matrix H_{ij} is also too big to be stored.

A more computationally efficient version of the algorithm called *List Mode Maximum Likelihood Expectation Maximization* (LM-MLEM) has been developed by Barret et al. [73] and tested by Parra and Barret [74]. The implementation of LM-MLEM for Compton cameras was done by Wilderman[75].

In the List Mode approach to MLEM (LM-MLEM) each one of the collected coincidences is considered as a unique bin and, thus, the sum over all the possible combinations of scatterer and absorber voxels is substituted by a sum over the list of detected coincidences N_{events}. The equation (5.23) is modified as:

$$f_j^{k+1} = \frac{f_j^k}{\epsilon_j} \sum_{i=1}^{N_{events}} \frac{H_{ij}}{\sum_{l=1}^{N_{BP}} H_{il} f_l^k}, \tag{5.24}$$

where ϵ_j is the camera efficiency for gamma photons emitted from the source position j[7]. Now the first sum is over the N_{events} detected coincidence events and each of the elements of the sum correspond to a single coincidence event (i.e., $p_i \to 1$). The second sum is now limited to the N_{BP} image voxels which are intersected by the back-projected cone. The value of N_{BP} is different for each coincidence event and must be computed by back-projecting the cone into the image FOV (see section 5.2.2).

A List Mode version of OSEM (LM-OSEM) can be obtained by applying LM-MLEM instead of MLEM in each OSEM iteration according to the following scheme:

- For each k iteration:
  - For each subset S_n:
    - For the N_S coincidence events in S_n:

$$f_j^{k+1} = \frac{f_j^k}{\epsilon_j} \sum_{i=1}^{N_S} \frac{H_{ij}}{\sum_{l=1}^{N_{BP}} H_{il} f_l^k}, \tag{5.25}$$

    - End loop over coincidence events.
  - End Loop over subsets.
- End iteration.

where N_S is the total number of coincidence events belonging to subset S_n. The sum over i is performed over the recorded coincidence events belonging to subset S_n, while

[7] Note that $\epsilon_j \neq \sum_{i=1}^{N_{events}} H_{ij}$.

the sum over l is performed over the N_{BP} image bins intersected by the back-projected cone surface.

With LM-OSEM the memory required by the algorithm is drastically reduced when compared with OSEM. This allows LM-OSEM to be implemented in Compton cameras with large number of channels. LM-OSEM has been evaluated for PET[32, 67], PEM [76], and Compton camera[77]. LM-OSEM will be one of the image reconstruction methods used in chapters 6.

Chapter 6

Modelization and Evaluation of VIP Compton Camera

The Monte Carlo simulation of the Compton camera design discussed in chapter 3 pursues two objectives. First, the simulation is to obtain the optimal values of the geometrical parameters of the design. Secondly, the Compton camera performance is evaluated on the efficiency and the image spatial resolution.

In the following sections we discuss the results of the simulations performed in order to establish the optimal geometrical parameters and the performance of the detectors for such configuration.

6.1 Geometry Modeling and Optimization

In this section we explore the effect of the different parameters of the Compton camera geometry on the performance of the scanner. The geometry of the design is defined by the planar area of the scatterer and the absorber detectors, together with their thicknesses, and the distance between them.

The planar surface of the scatterer and the absorber determines the size of the objects that can be scanned and affects the efficiency of the camera. Bigger detector surface yield higher efficiency and increased FOV. The surface that has been chosen for the Compton camera design (54×38 cm^2) is comparable to the size of the gamma cameras that can be found in commercial SPECT system. In this way, the comparison between the different tomographers can be performed easier.

The thicknesses of the detectors affect the efficiency of the Compton camera as they modify the interaction probability of the different possible physical processes. In the case of the scatterer detector more thickness implies a higher probability of Compton interaction for an incoming gamma photon. But as we increase the thickness the probability of multiple Compton scattering also increases. As has been discussed in previous sections (see 4.2), for a coincidence event, a single energy deposition should occur in each of the detectors within the time coincidence window and, thus, the events with more than one energy depositions in the scatterer are rejected. Therefore, for each value of the energy of the incoming gamma photon exists an optimal scatterer thickness that maximizes the camera efficiency.

Increasing the thickness of the absorber increases the probability of photoelectric interaction for the incoming gamma photons. The photoelectric probability will increase up to a point in which all the photons are absorbed. Further increase of the thickness beyond this point will have no effect on the camera efficiency. This optimal thickness value depends on the energy of the gamma photons emitted by the source.

Given the module designs discussed in section 3.2 of chapter 3, we can modify the scatterer thickness in steps of one centimeter by adding scatterer detector slices (see figure 3.7). In the case of the absorber we can also increase the thickness in steps of one centimeter by adding CdTe material (together with its read-out electronics) to the module (see figure 3.5).

We have performed MC simulations for different thickness values following the procedures discussed in chapter 3. The source used is based on the NEMA NU-4 2008[78] point-like source phantom. The phantom (see figure 6.1) consists of a cube made from acrylic material with a sphere in its center filled with water containing a certain activity of the isotope selected as source. The cube sides are 10 mm long, while the sphere radius is 0.1 mm. The phantom is placed at 10 cm from the edge of the scatterer and in the center of the camera FOV.

TABLE 6.1: Simulation Parameters

Generated events	5M
Measuring Time	20 μs
Dead Time	130 μs
Time Resolution	20 ns
Scatterer Trigger Threshold	10 keV
Absorber Trigger Threshold	20 keV
Scatterer to Absorber Distance	50 mm

Two different isotopes: ^{99m}Tc and ^{18}F, were used as a source. Each ^{99m}Tc decay produces a 141 keV gamma photon while the decays from ^{18}F produce a positron that

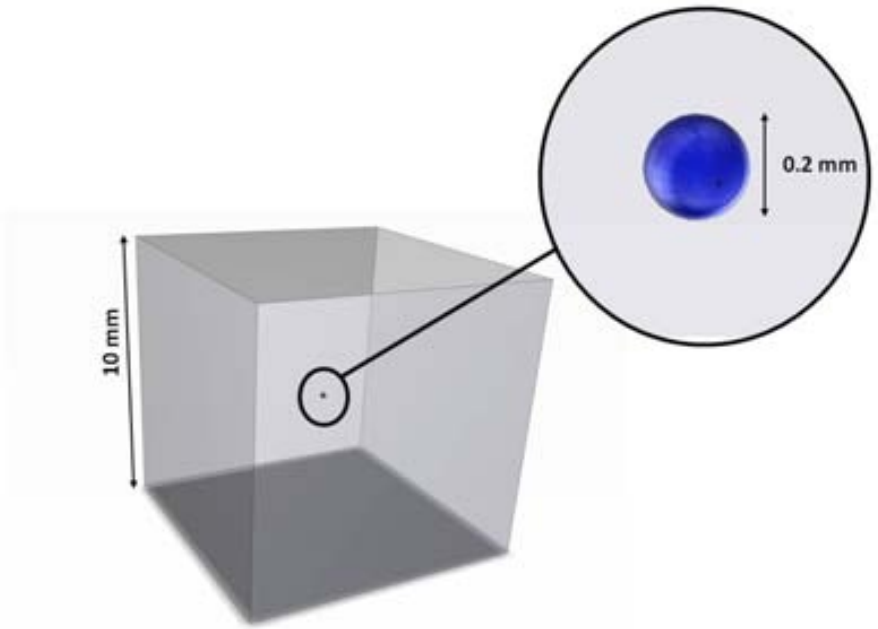

FIGURE 6.1: Representation of the PSF phantom based on NEMA NU-4 2008.

eventually annihilates with an electron creating a pair of 511 keV[1] gamma photons. The registered efficiency with ^{18}F is twice the value that would be registered with a 511 keV single photon emitter as each electron-positron annihilation in ^{18}F creates two gamma photons. These two isotopes are representative of the lower and upper limits of the energy range in which the camera is designed to operate.

The results of the simulations for the modeling of the detectors are shown in figure 6.2. The simulation parameters used are summarized in table 6.1. The energy resolution of the detectors (see chapter 4, section 4.2.1) is implemented in the simulation by smearing the deposited energy of each hit according to the different contributions to the error on the energy due to statistical fluctuations, electronic noise, and detector defects.

In the case of the scatterer the simulation shows that two centimeters of silicon provides the best efficiency compromise for the 141-511 keV range (see figure 6.2). The signal purity, defined as the fraction of true coincidences over all the detected, decreases with increasing scatterer thickness. The reason behind this decreasing purity is the increase of the number of multiple Compton interactions. If a gamma photon undergoes two consecutive Compton interactions in the scatterer in such a way that one of the energy depositions is below the trigger threshold, then the event can be wrongly identified as a one-to-one coincidence if the gamma undergoes a photoelectric interaction in the

[1] Assuming that the positron loses all its kinetic energy before the annihilation.

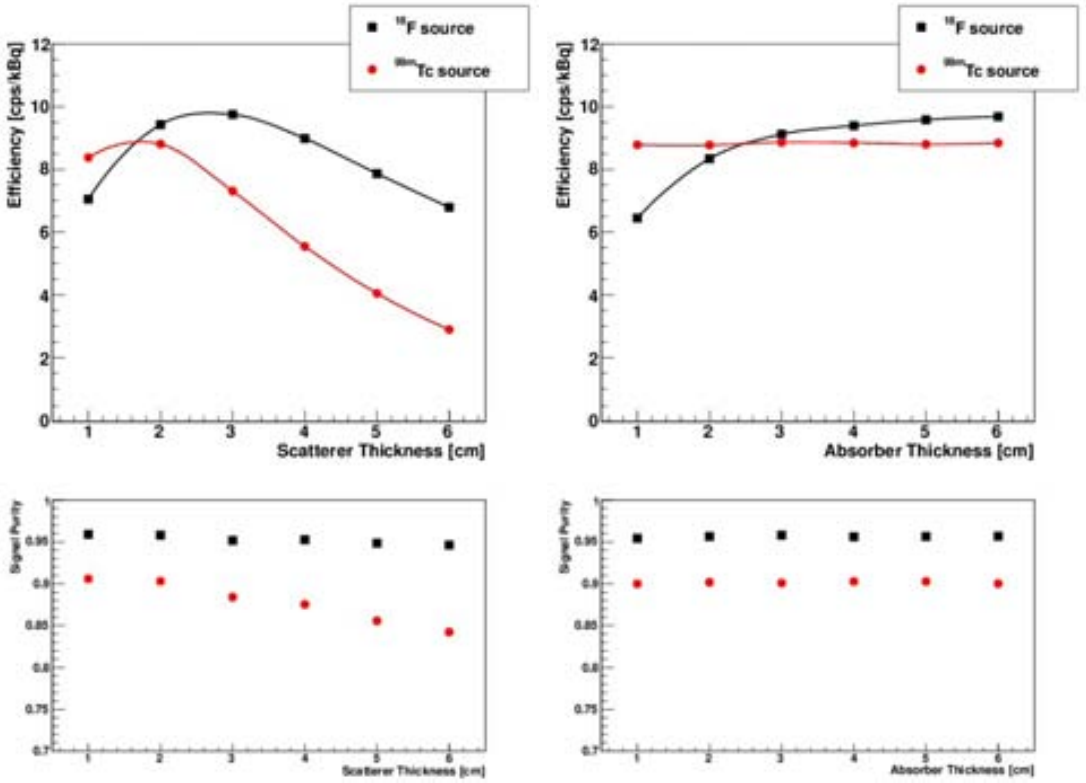

FIGURE 6.2: *Left:* efficiency (top) and signal purity (bottom) for different scatterer (Silicon) thicknesses. *Right:* efficiency (top) and signal purity (bottom) for different absorber (CdTe) thicknesses.

absorber afterwards. The signal purity for an scattering thickness of two centimeters is 93% for ^{18}F and 88% for ^{99m}Tc. The source of wrongly identified coincidences will be discussed in more detail in the next section.

For the absorber, one centimeter of CdTe is enough to stop all the incoming photons emitted by ^{99m}Tc, while at least four centimeters of thickness are required in order to absorb the 511 keV gamma photons produced by ^{18}F. However, a reduction of two centimeters in the absorber thickness will result into a $\sim 8\%$ reduction on the camera efficiency while the detectors cost would be cut by half. Even with 1 cm thickness for the absorber, and using two Compton cameras with two different orientations, there would not be a loss in efficiency whereas the cost of this system would be much lower. Similar arguments can be made for a thinner scatterer. However, in order to be able to use the same module as is used for the VIP PET design, we have done our simulations with 4 cm of absorber and 2 cm of Silicon, which, as figure 6.2 shows, gives a very good efficiency. As we will see in section 6.4.1, the image quality can be improved by reconstructing the image from the merged data coming from two cameras with different orientations.

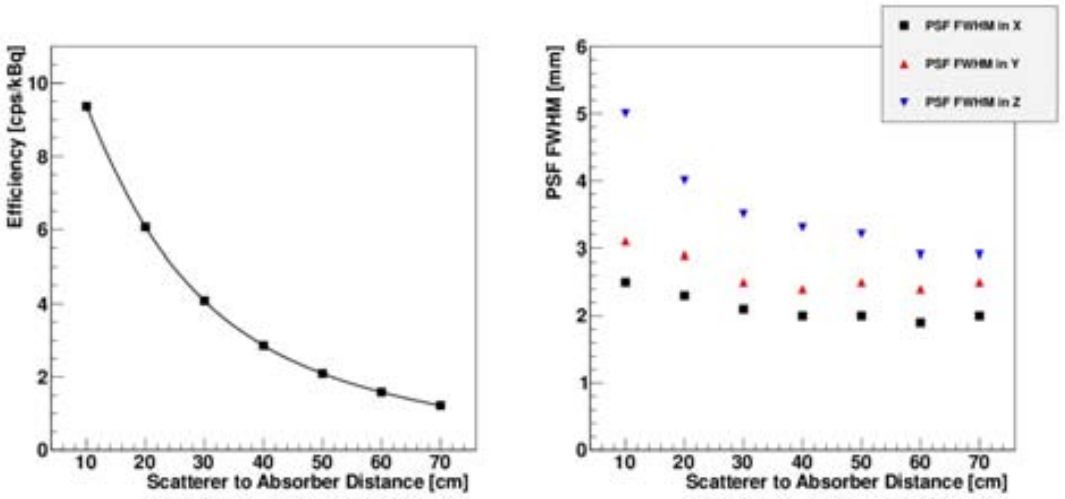

FIGURE 6.3: *Left:* Compton camera efficiency for different distances between the scatterer and the absorber detectors. ^{18}F isotope is used as source. *Right:* image resolution measured through the PSF FWHM in the different directions.

The distance between the scatterer and the absorber affects the Compton camera performance in two ways. As the distance between the detectors increases less gamma photons coming from the scatterer are able to reach the absorber resulting in a reduction of the camera efficiency. On the other hand, this increase in the distance reduces the angular error introduced by the size of the voxels (see chapter 2, section 2.2). This reduction of the geometrical angular error results in an improvement of the image spatial resolution.

TABLE 6.2: Compton Camera Geometrical Parameters

Field-Of-View	54×38 cm^2
Scatterer thickness	2 cm
Absorber thickness	4 cm
Scatterer-to-Absorber distance	10 cm

In order to quantify these effects in the case of our Compton camera design, we have performed simulations for different distances between the scatterer and the absorber. The same point-like phantom described above and the same parameters of table 6.1 were used for the simulations. The ^{18}F isotope is used as gamma source. The results are shown in figure 6.3. As shown by the simulation, in order to set the scatterer to absorber distance one has to choose to find a compromise between efficiency and image spatial resolution. From now on, we will set this distance at 10 cm as good image resolution can be achieved while having a high enough detector efficiency.

We have used the geometrical parameters summarized in table 6.2. To study the system efficiency, the signal purity, and the different sources of wrong coincidence identification.

6.2 Efficiency and Signal Purity

The MC simulation allows us to study not only the Compton camera efficiency, but also the signal purity and the various contributions to the wrongly identified coincidence events.

For the simulation study we used a phantom described in the NEMA NU 1-2007 [79] standard. The phantom is used for the evaluation of the count rate in scatter conditions for gamma cameras. It consists of a source holder container which is a disc made of acrylic material containing active water (with a given activity of the radiactive isotope of choice). The source holder is placed inside a case made also of acrylic material which is filled with water. A depiction of the phantom including its shape and size is shown in figure 6.4.

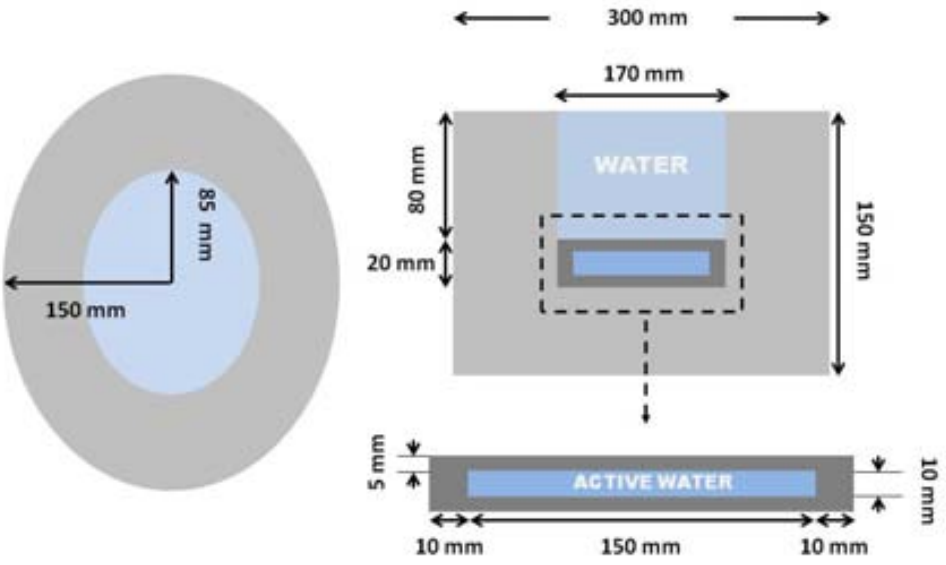

FIGURE 6.4: Schematic representation of the phantom for the count rate in scatter test described in NEMA NU 1-2007.

The same number of events are generated for different activities placed in the phantom. When the activity gets too high, the efficiency to detect two hit coincidences decreases as a consequence of the pile-up of events, up to the point in which the camera is completely saturated. The activity for which the camera saturates is mainly determined by the time coincidence window. When the activity increases up to a point in which several gamma photons can reach the camera and produce interactions within the time coincidence

window, saturation occurs. With higher activities, the detectors are not able to identify the coincidence events.

For each of the activity values the detected coincident events are clasiffied as follows:

- **True coindence:** event produced by a single gamma photon which undergoes a Compton interaction in the scatterer and a photoelectric interaction in the absorber.
- **Scattered event:** event for which the gamma photon has already scattered before reaching the camera, losing energy and changing its propagation direction in the process.
- **Random event:** in these events the two hits of the coincidence event are originated from two different unrelated gamma photons.
- **Other physics:** the main contribution to these events is back-scattering. In a back-scattering event the gamma photon crosses the scatterer without interacting, then it reaches the absorber detector undergoing a Compton interaction in which the gamma photon scatters back to the scatterer where the gamma finally undergoes a photoelectric absorption. Also coincidences produced by Rayleigh interactions fall into this category.

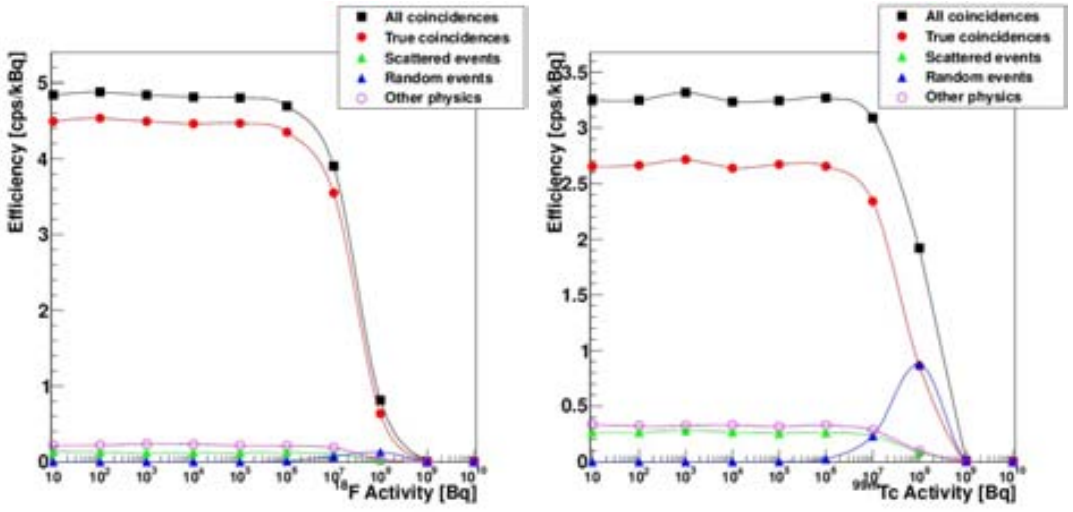

FIGURE 6.5: Compton camera efficiency for different ^{18}F (left) and ^{99m}Tc (right) activities. The detected coincidence events are classified.

The results of the test for ^{99m}Tc and ^{18}F isotopes are shown in figure 6.5. The simulations show that the camera can operate, using ^{99m}Tc or ^{18}F, with source activities up to 10^6 Bq with equal efficiency and is completely saturated at 10^9 Bq. The number

of true coincidence events amounts to 93% of the total number of detected coincidence events coming from ^{18}F and 82.32% of the ^{99m}Tc coincidence events.

The scattered events are mostly rejected thanks to the excellent energy resolution of the solid state detectors which allows to measure the total deposited energy in the two interactions and compare the sum of both energies with the original gamma energy. In the case of ^{18}F the scattered events amount to 2.53% of the measured coincidences, while for ^{99m}Tc they amount to 7.87% of the coincidence events. The increase of scattered events in ^{99m}Tc with respect to ^{18}F is due to the higher probability of low energetic Compton scattering in the source passive material of the 141 keV gamma photons.

The random events remain negligible in the non-saturated range for both isotopes. When the camera begins to saturate, due to pile-up events, the number of random events increases, especially in the case of ^{99m}Tc.

The other physics category amounts to 4.45% of the coincidence events for ^{18}F and 9.74% for ^{99m}Tc. The main contribution to these events is due to back-scattering as has been explained before.

The above results show the noise rejection capabilities of the Compton camera under high scattering environments. This allows to obtain a coincidence list with high purity, something which is very important in order to obtain a good image quality.

6.3 Reconstruction of Events with Multiple Energy Depositions

In the previous sections we have optimized the Compton camera geometry and we have studied its efficiency and purity. In these studies the coincidence events from which the images are reconstructed consist of a single interaction in the scatterer and a single interaction in the absorber.

However, undergoing a single-single coincidence is just one of the possibilities for the gamma photons that reach the camera. The number of events with more than two energy depositions produced by a single gamma photon grow as the energy of the emitted gammas increases. The recovery of these events can greatly augment the efficiency of the camera.

In this section we study a method to identify and recover coincidence events composed by more than two hits. We restrict ourselves to the events with a single energy deposition in the scatterer and two energy depositions in the absorber as this is the main contribution

in the 141 to 511 keV range. For higher energies, as occurring in gamma-ray astronomy, events with more than three energy depositions become more predominant. Several reconstruction methods have been investigated in this case [80].

6.3.1 Classification of Three-Hit Coincidence Events.

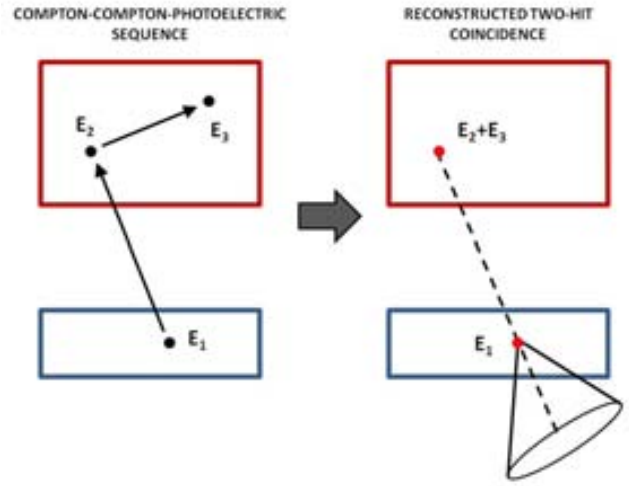

FIGURE 6.6: Reconstruction of a Compton-Compton-photoelectric sequence as a regular two-hit coincidence event.

The three-hit coincidence events consist of three energy depositions, one in the scatterer and two in the absorber, which happen within the time window defined by the timing resolution of the detectors. These three-hit coincidence events can occur in many different ways. For example, the interactions produced by two gamma photons reaching the camera simultaneously (i.e. random events). The three-hit coincidences that we might be able to recover as regular two-hit coincidences, are the ones produced by a single gamma photon as a result of two Compton interactions followed by a photoelectric absorption. If the order of this Compton-Compton-photoelectric (CCP) sequence is known then the event can be transformed in a two-hit coincidence event in which the first hit corresponds to the first Compton event of the CCP sequence and the second hit will have the position of the second Compton scattering hit of the CCP sequence and the energy equal to the energy of the second Compton hit (E_2), plus the photoelectric absorption (E_3) of the sequence (see figure 6.6).

In a Compton camera the CCP sequence can happen in six different ways as shown in figure 6.7. We classify these six possibilities in three categories depending on the order of the sequence.

- **Double Compton:** The first hit of the CCP sequence occurs in the scatterer (case A).
- **Simple backscattering:** The first and second hits of the CCP sequence occur in the absorber (case B).
- **Double backscattering:** The first hit of the CCP sequence occurs in the absorber, the second occurs in the scatterer, and the third in the absorber (case C).

Any of these CCP sequences can be recovered as a two-hit coincidences if the order of the sequence is known.

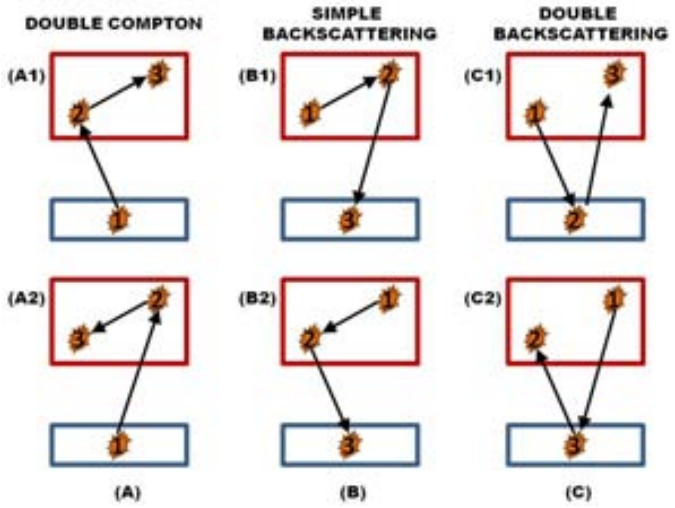

FIGURE 6.7: The six possible combinations of the Compton-Compton-photoelectric sequence. The order of the sequence is numbered. (a) Double Compton coincidence. (b) Three-hit simple backscattering coincidence. (c) Three-hit double backscattering coincidence.

In order to study the three-hit coincidence events and test the performance of our algorithm, we simulated 20 million generated gamma photons with an energy of 511 keV. The photons are emitted over a solid angle of 4π from an ideal point-like source placed at 10 cm from the scatterer edge with an activity of 10^5 Bq. The detector parameters used for the simulation are the same as used in previous sections (see table 6.1).

From the simulation on can observe that 0.63% of the emitted gammas undergo a two-hit coincidence while 0.67% undergo a three-hit coincidence. Within the three-hit coincidences 79% of them consist of a CCP sequence that we can potentially recover. These events are distributed within the three possible categories as follows: 97.66% of them are double Compton coincidences, 2.19 % are double backscattering, and 0.15% are single backscattering.

6.3.2 Time Ordering of the Compton-Compton-Photoelectric Sequences.

The aim of the algorithm is to identify the CCP sequences within the three-hit coincidence events and then establish the time order of the sequence to be able to transform the event into a two-hit coincidence. To achieve this, the algorithm seeks to identify the second Compton interaction of the sequence by comparing the geometrical scattering angle θ_G and the Compton scattering angle θ_E for each one of the possible orders of the CCP sequence.

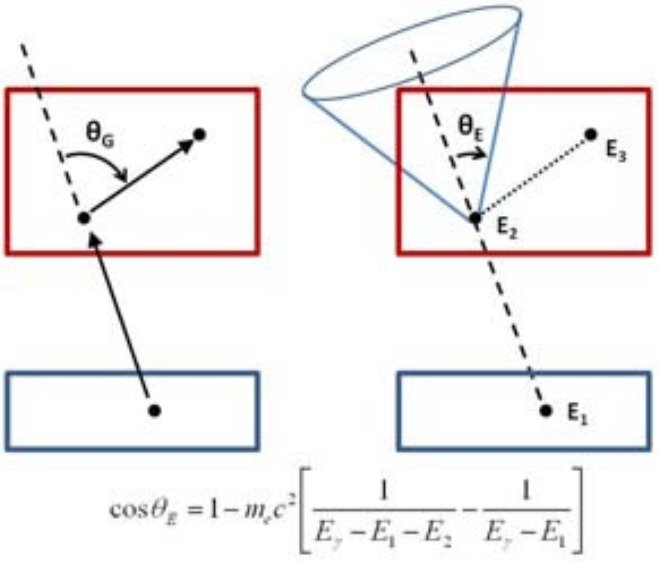

FIGURE 6.8: Geometrical scattering angle θ_G and Compton scattering angle θ_E for a given order of the CCP sequence. When the assumed order of the sequence is the correct one, both angles should be equal.

Assuming a given order of the CCP sequence one can calculate the scattering angle of the second hit of the sequence in two ways. First it can be done directly from the positions of the three hits. This geometrical scattering angle θ_G is the angle formed between the vector connecting the first and second hits and the vector connecting the second and third hits. On the other hand, if the chosen order of the sequence is correct, the second hit of the sequence is a Compton interaction. Therefore, the Compton scattering angle θ_E can be computed by using the Compton interaction kinematics (see chapter 2 and figure 6.8). These two angles θ_G and θ_E will be equal for the correct time order of the sequence. Hence, a way to identify the correct ordering consists of the computation and comparison of these two angle for each of the possible time orders of the CCP sequence.

If the uncertainty of $|\theta_G - \theta_E|$ is known, one can compute this quantity for the possible configurations within a given category (double Compton, simple and double backscattering) and check if the resulting value is below such uncertainty and therefore compatible

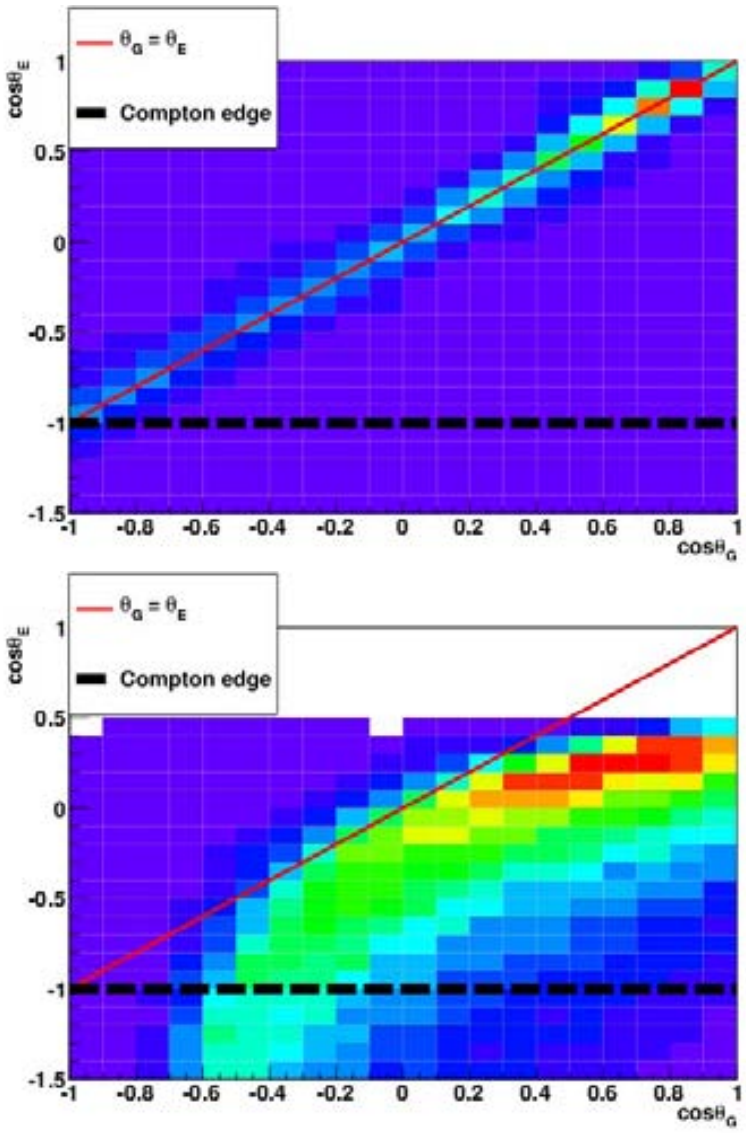

FIGURE 6.9: *Top:* Comparison between $\cos\theta_G$ and $\cos\theta_E$ for the correct sequence. *Bottom:* Comparison between $\cos\theta_G$ and $\cos\theta_E$ for the wrong sequence.

with zero. In the case of θ_E the sources of this uncertainty are the energy resolution of the detector and the Doppler broadening effect, while for θ_G it is the voxel size which limits the spatial precision[2].

The following steps are applied in order to identify the order of a potential CCP sequence:

1. For each one of the possible orderings of the CCP sequence, compute $|\theta_G - \theta_E|$.
2. If $|\theta_G - \theta_E|$ is below a given tolerance (based on the uncertainty) for one, and only one, of the possible orderings accept the three-hit coincidence as a CCP with this ordering.

[2]As we have seen in section 6.1, the scatterer to absorber distance also affects the error of θ_G.

Following the steps mentioned above, one can try to identify the CCP sequences for all the categories at once or just one or two of them simultaneously.

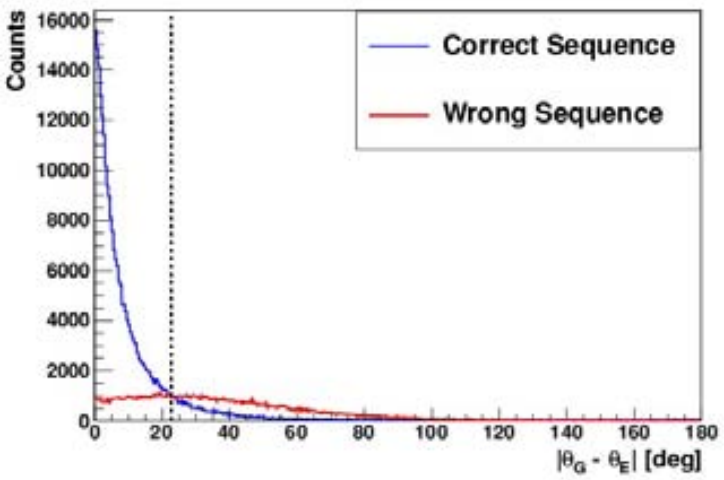

FIGURE 6.10: Distribution of $|\theta_E - \theta_G|$ for the correct and wrong CCP sequence. The blue line correspond to the correct sequence order in which $\theta_E = \theta_G$. The red line corresponds to a wrong ordering. The dashed line shows the intersection of both curves. This value will yield the maximum efficiency of the algorithm.

The method described above depends on the precision for which the value of the uncertainty of $|\theta_G - \theta_E|$ for the correct time order of the CCP sequence is known. To obtain this uncertainty we select from the simulation data the real CCP sequences in order to study the values of the angles for the correct and wrong orderings. In figure 6.9 we show $cos\theta_E$ *vs* $cos\theta_G$ calculated for the correct order and the wrong order. With the correct ordering, the obtained values of $cos\theta_E$ and $cos\theta_G$ are spread around the line defined by $\theta_G = \theta_E$ as expected. For the wrong ordering we see that $cos\theta_E$ takes values from $-\infty$ to 1 (corresponding to deposited energies between the 0 and the incident gamma energy). This allows us to discard the orderings for which the calculated value of $cos\theta_E$ is below -1.

In figure 6.10 the distribution of $|\theta_E - \theta_G|$ for the correct and wrong orderings of the CCP sequences are shown. From the overlapping of the two distributions it is clear that we can expect that some of the coincidences will be wrongly identified by the algorithm no matter the tolerance we use. The maximum efficiency of the algorithm is achieved on the intersection point of the two curves. In the case of the VIP Compton camera this intersection corresponds to a value of $|\theta_G - \theta_E|$ of 23 degrees for 511 keV gamma photons.

6.3.3 Monte Carlo Results.

The main contribution to the three-hit coincidences are the double Compton. When reconstructing only double Compton the algorithm recovers 43% of the three-hit coincidences with a purity of 94.7%, i.e., fraction of correctly reconstructed over all the reconstructed. In this way we can add 2.87 cps/kBq to the efficiency of the camera coming from the recovered three-hit coincidence events. When all the categories are reconstructed together the fraction of recovered three-hit coincidences reduces to 36.2% and the purity to 92%. As we add the other categories there are events which can fit in several categories simultaneously and they are discarded resulting in a loss of the algorithm performance. The algorithm fails in the reconstruction of the backscattering events (B) as it is unable to distinguish these events from their double Compton (A) opposite sequence. The reason is that both sequences share the same geometrical Compton scattering angle.

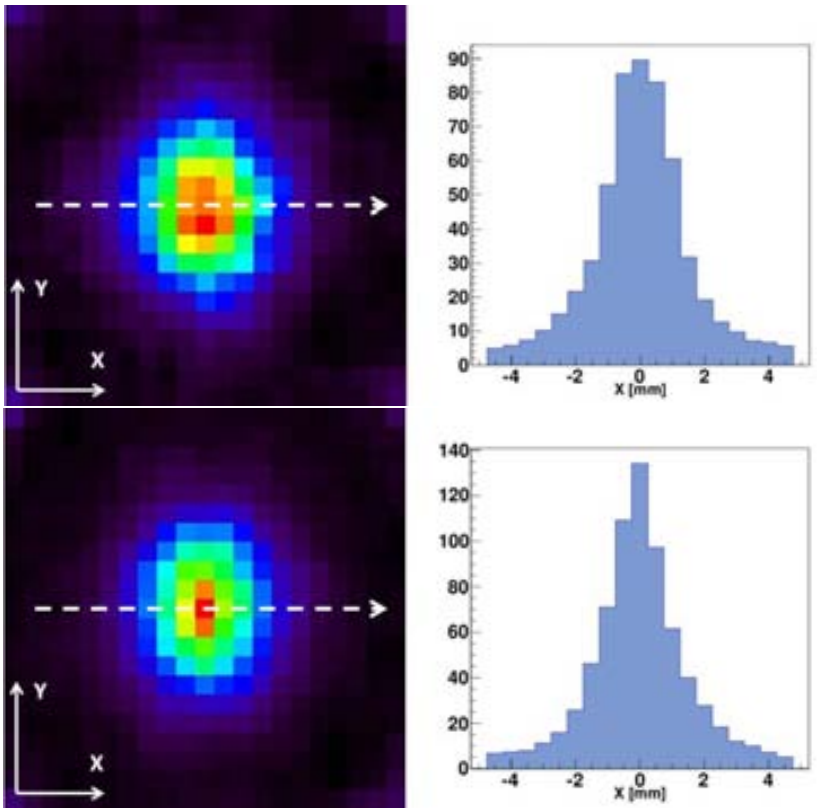

FIGURE 6.11: *Top:* In the left we show the central slice of the image of the point-like source reconstructed from two-hit coincidence events. On the right we show line profile along X axis of the same image. *Bottom:* In the left we show the central slice of the image of a point-like source reconstructed from three-hit coincidence events. On the right we show line profile along X axis of the same image.

Finally, in order to test that the recovered events contain the information needed for the image reconstruction we used two samples, each containing 200k coincidence events, to

reconstruct the image of the source from each of them. The first sample contains only detected two-hit coincidence events while the second is composed of recovered three-hit coincidences only. The images obtained are shown in figure 6.11. As can be seen in the images the recovered events carry the correct information.

The simulation results shows that by using the described method the efficiency of the Compton camera can be increased without deterioration of the original purity of the collected coincidences.

6.4 Image Spatial Resolution

In this section we study the image resolution that the Compton camera is able to achieve by using two different image reconstruction algorithms: Origin Ensemble (OE) and List Mode Ordered Subset Expectation Maximization (LM-OSEM).

We first quantify the image spatial resolution of the system by simulating a point source. The obtained values will be verified by placing two point like sources together in order to see if they can be distinguished.

6.4.1 Point Spread Function.

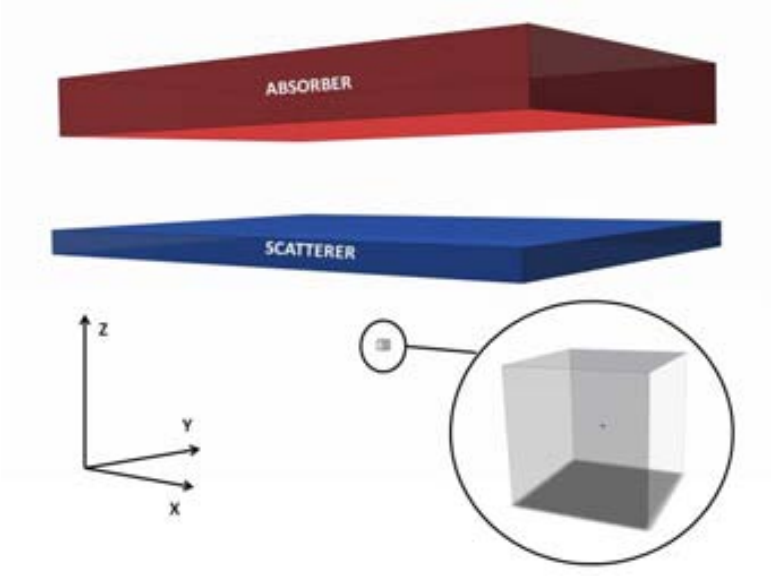

FIGURE 6.12: Scheme of the positioning of the PSF NEMA NU 1-2007 phantom with respect to the Compton camera.

The point spread function (PSF) is defined, for a given imaging system, as the image produced from a point source or point object. The spread of such an image provides an estimation of the system image resolution.

Using the phantom described in section 6.1 and illustrated in figure 6.1, we have reconstructed the PSF obtained for ^{18}F and ^{99m}Tc point-like gamma sources. Two different image reconstruction algorithms are employed: OE and LM-OSEM (see chapter 5).

All images are reconstructed using two million coincidence events. The point-like source phantom is placed at 10 cm from the scatterer edge and has an activity of 10^5 Bq of either ^{18}F or ^{99m}Tc. The distance between the phantom and the camera corresponds to the standard value used in SPECT image performance tests, allowing the comparison with commercially available gamma cameras. The image space is a cube of 20 mm sides segmented into voxels of 0.5×0.5×0.5 mm^3 size in the case of ^{18}F images, and 1×1×1 mm^3 in the case of ^{99m}Tc. The size of the image space voxels is adjusted according to the PSF size.

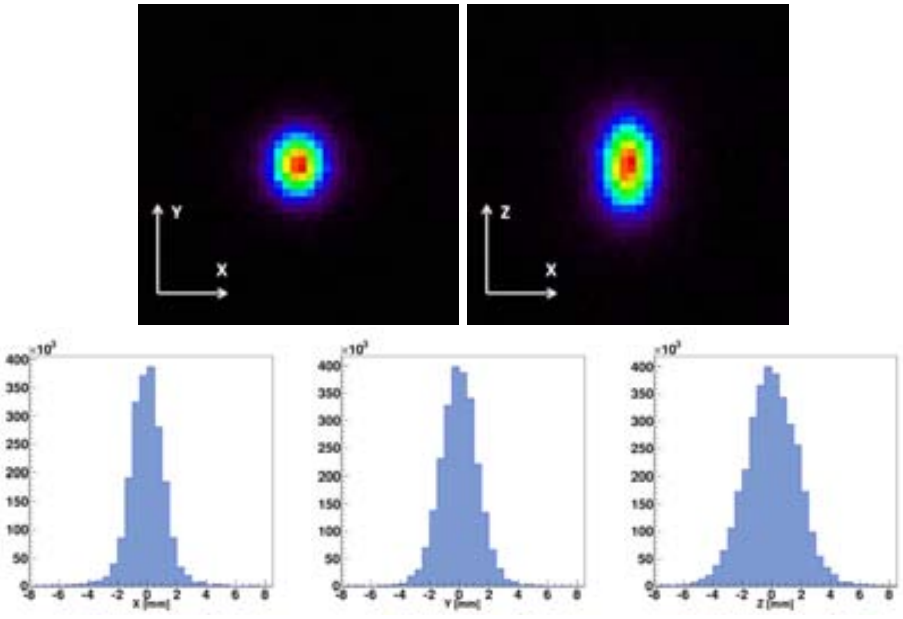

FIGURE 6.13: ^{18}F PSF reconstructed with OE. On the top image central slices in the X-Y and X-Z planes are shown. In the bottom the line profiles along the different directions are shown.

The positioning of the phantom with respect to the Compton camera is illustrated in figure 6.12. The coordinate axes are defined in such a way that the Z direction of the image space corresponds to the direction perpendicular to the scatterer plane, while the X direction is parallel to the stack modules, and the Y direction is perpendicular to them.

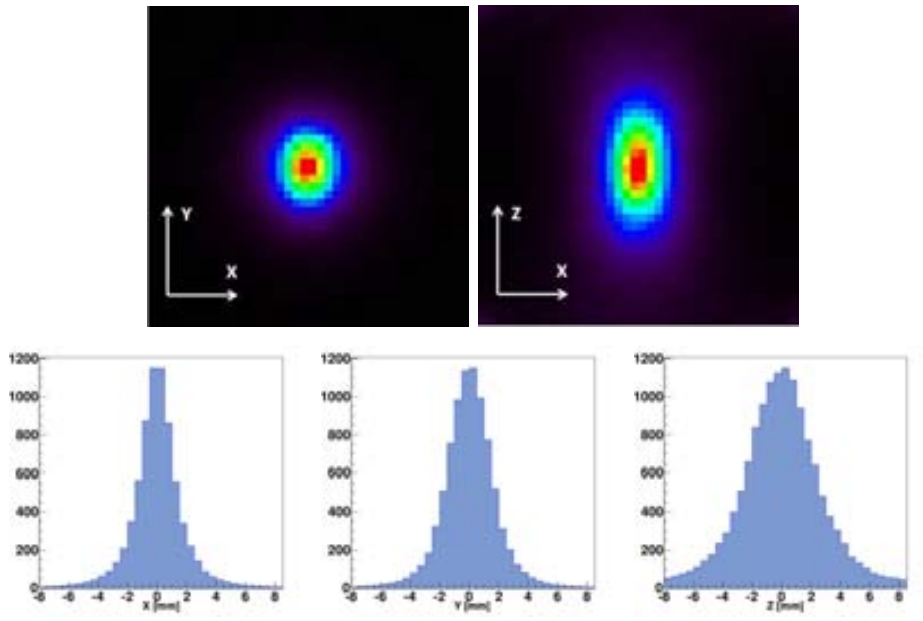

FIGURE 6.14: ^{18}F PSF reconstructed with LM-OSEM. On the top, image central slices in the X-Y and X-Z planes are shown. In the bottom, the line profiles along the different directions are shown.

The image spatial resolution is expected to be worst along the Z direction. The cones corresponding to the coincidence events are predominantly orientated along the Z direction and, as a result, the angular error on the cone surface will produce more spatial uncertainty along Z than along X or Y. It is expected to obtain worse image spatial resolution along Y axis than along X. This is due to the different geometrical angular error over the two directions (see chapter 2, section 2.2.2) because of the asymmetry in the shape of the voxels composing the scatterer and the absorber. The voxel pitch is equal to one millimeter along X and two millimeter along Y. The worse resolution along Z can be compensated by combining the data obtained from two different orientations (see figure 6.17).

The image spatial resolution is quantified as the FWHM of the PSF along the different directions. Line profiles crossing the source location along the different directions are computed and fitted to a Gaussian function (see table 6.3). The reconstructed images and projections using OE algorithm are shown in figures 6.13 and 6.15, for ^{18}F and ^{99m}Tc respectively. Due to the stochastic nature of OE, several trials must be performed in order to avoid random distortions of the PSF. A hundred OE iterations are applied over the same data in each trial. A total of hundred trials were performed and added up to produce the OE images. The images reconstructed with LM-OSEM and the line profiles are shown in figures 6.14 and 6.16, corresponding again to the ^{18}F and ^{99m}Tc isotopes respectively. To produce the images ten LM-OSEM iterations were performed.

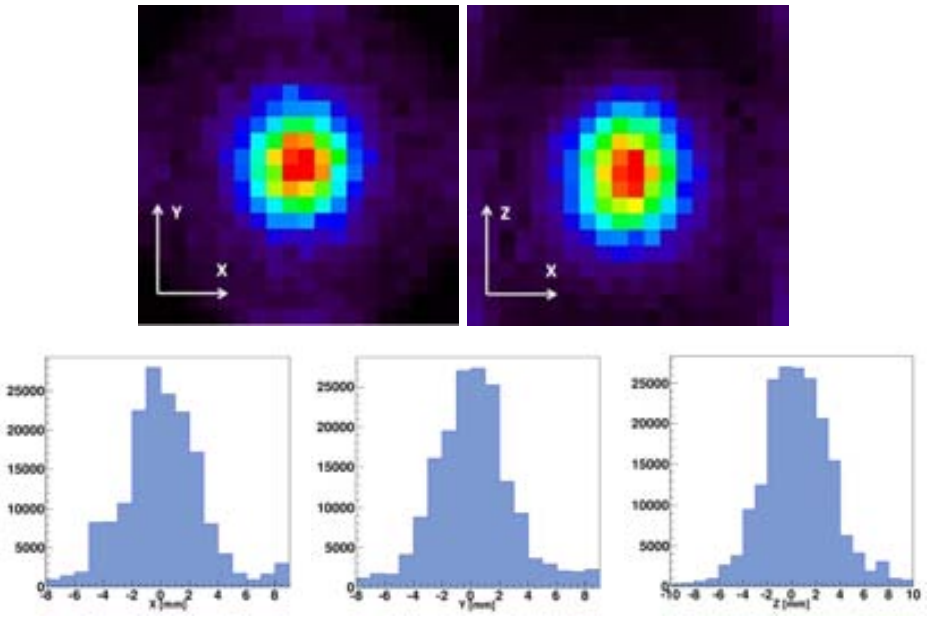

FIGURE 6.15: ^{99m}Tc PSF reconstructed with OE. On the top image central slices in the X-Y and X-Z planes are shown. In the bottom the projection profiles along the different directions are shown.

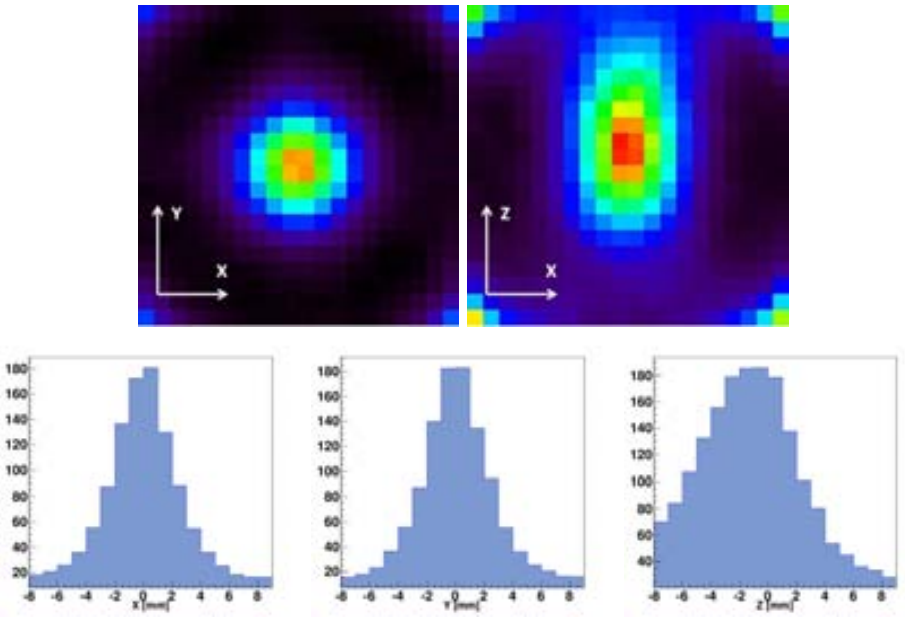

FIGURE 6.16: ^{99m}Tc PSF reconstructed with LM-OSEM. On the top, image central slices in the X-Y and X-Z planes are shown. In the bottom, the line profiles along the different directions are shown.

TABLE 6.3: Values of the PSF FWHM for ^{18}F and ^{99m}Tc.

	^{18}F PSF [mm]		^{99m}Tc PSF [mm]	
	OE	LM-OSEM	OE	LM-OSEM
X	1.97	2.62	4.92	4.70
Y	2.33	3.29	5.07	4.82
Z	3.83	4.99	5.77	8.09

The obtained values of PSF FWHM are summarized in table 6.3. The image resolution is better for ^{18}F than for ^{99m}Tc as the angular error from energy resolution[3] and Doppler broadening effect decreases with increasing energy of the emitted gamma photons. As was expected the resolution is better along X axis, followed by Y axis, and is the worst for Z axis. OE and LM-OSEM provide comparable values of the FWHM for both isotopes, but LM-OSEM provide images with less noise.

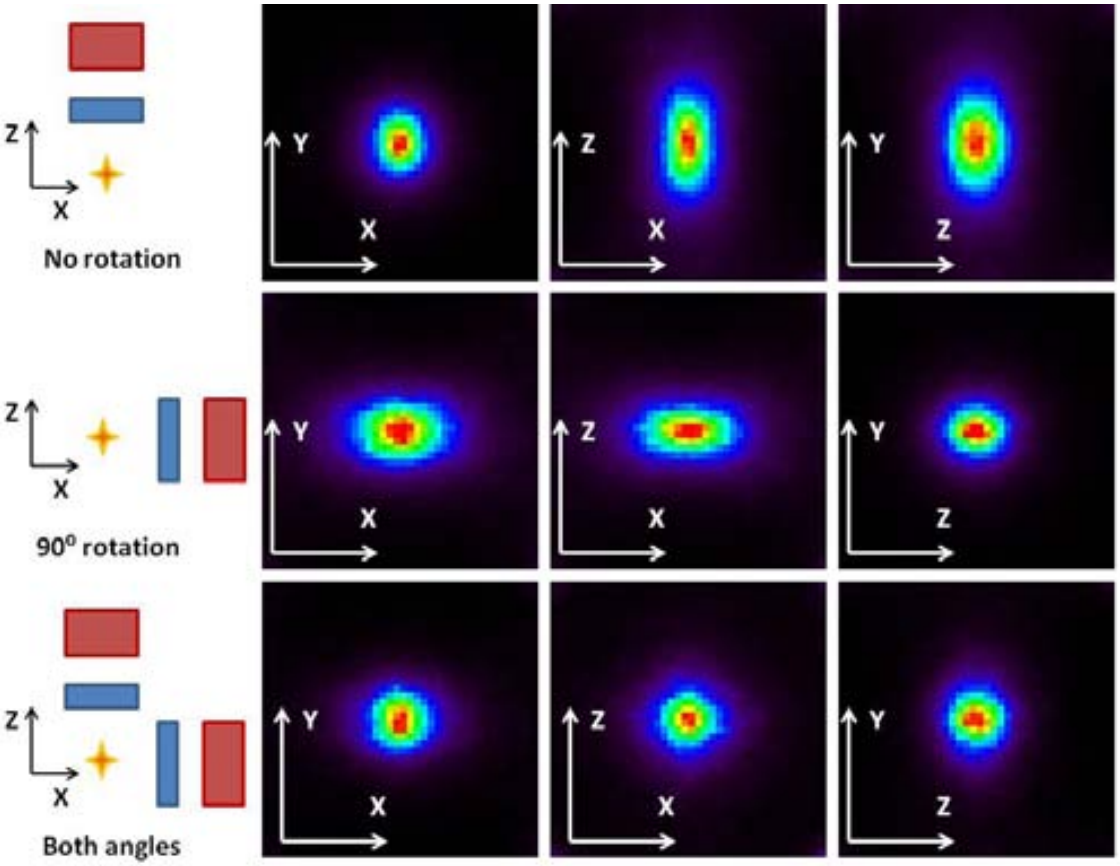

FIGURE 6.17: Images of an ^{18}F point-like source obtained from two different directions. *Top:* Images obtained with the Compton camera plane perpendicular to the Z axis.

A possible way to improve the image resolution along the direction perpendicular to the scatterer edge consists of scanning the phantom from two different directions and reconstruct the image from the combined data of the two scanning positions. In figure 6.17 we show the images obtained by scanning from two orthogonal directions, first separately and then mixing both data sets. The phantom used is again the point-like source phantom discussed above. ^{18}F isotope is used as a gamma source. All the images in the figure are reconstructed using LM-OSEM. As can be seen in the figure, the obtained PSF when mixing the data from both directions is spherically symmetric.

[3] As the energy resolution of the detectors is better for higher energies.

The FWHM value from the Gaussian fit of the line profiles along the axes directions are summarized in table 6.4.

TABLE 6.4: Values for the PSF from two different positions of the camera and the values resulting from mixing the data from both directions. The ^{18}F isotope is used as gamma source. The images are reconstructed using the LM-OSEM algorithm.

	0 degrees	90 degrees	Both
FWHM X [mm]	2.64	4.58	3.13
FWHM Y [mm]	3.25	3.15	3.15
FWHM Z [mm]	4.80	2.59	3.09

The data from two directions can be obtained by rotating the camera or by using two camera heads simultaneously. As has been discussed in section 6.1 if the absorber thickness is reduced by half, the camera efficiency drops only $\sim 8\%$, while the CdTe sensors can be used to build a second absorber detector reducing the cost of building a second camera head.

In the next section we will test the obtained values of the PSF by placing two point-like source at a distance comparable with the PSF FWHM.

6.4.2 Two Point-like Sources.

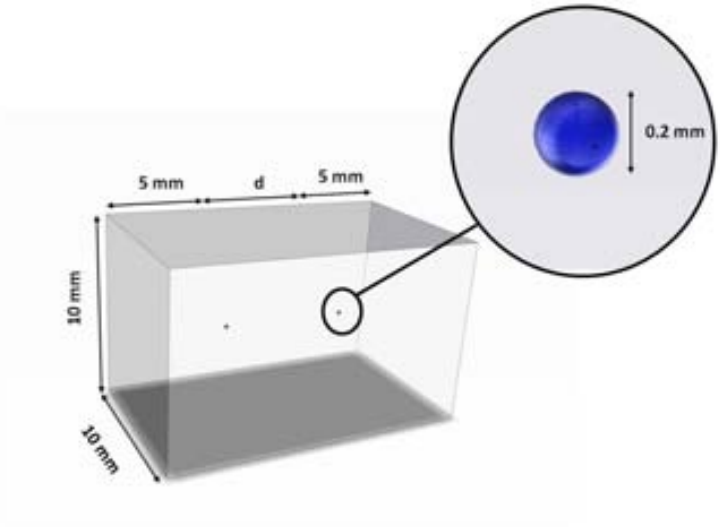

FIGURE 6.18: Phantom used for the two point source simulation. The distance d is set to 3 mm for ^{18}F and to 7 mm for ^{99m}Tc.

In order to test the image resolution of the system we have simulated two point sources separated at distances comparable with 1.5 times the PSF FWHM, as measured in the previous section.

The phantom used in the simulation is a modified version of the NEMA NU 4-2008 point phantom used in the previous section and described in 6.1. The phantom consists of a rectangular parallelepiped containing spheres with 0.1 mm radius filled with active water. The squared sides of the parallelepiped are 10 mm and the longitude in the other direction is 10 mm plus the separation between the spheres. In the case of ^{18}F the spheres are separated 4 mm ($\sim 1.5 \cdot 2.62$ mm (see table 6.3)), while the separation in the case of ^{99m}Tc is 7 mm ($\sim 1.5 \cdot 4.7$ mm (see table 6.3)). The phantom is placed at 10 cm of the scatterer edge with the two point sources aligned along the X direction, and containing 10^5 Bq of either ^{18}F or ^{99m}Tc.

The simulation parameters used in the previous test are also used for these simulations (see table 6.1). The image space is again a cube with 20 mm side segmented into 0.5 mm side cubic voxels in the case of ^{18}F sources and 1 mm side in the case of ^{99m}Tc sources. Four million coincidence events were used in order to reconstruct the images. In the case of the images reconstructed with OE, 100 iterations and 100 trials are performed in order to obtain the images. The images produced by LM-OSEM are obtained from 10 iterations.

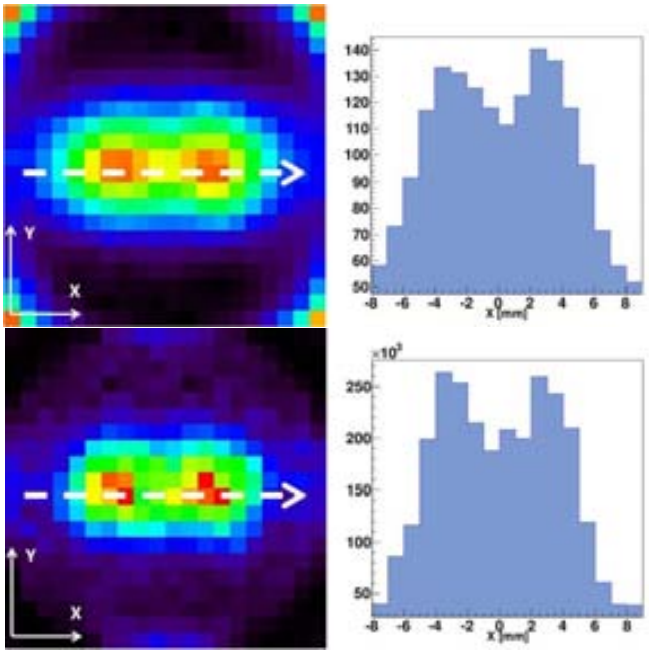

FIGURE 6.19: Images of the two point-like sources containing ^{99m}Tc and separated by 7 mm. *Top:* Images of the central slice in the X-Y plane and line profiles over X axis, reconstructed with LM-OSEM. *Bottom:* Images of the central slice in the X-Y plane and line profiles over X axis, reconstructed with OE.

The images obtained from two ^{99m}Tc point-like sources are shown in figure 6.19. As can be seen in the figure the two point-like sources can be clearly distinguished for both OE and LM-OSEM. The spread of the image of each point source is consistent with the

values obtained in section 6.4.1 and the position of the peaks is consistent with the real position of the sources.

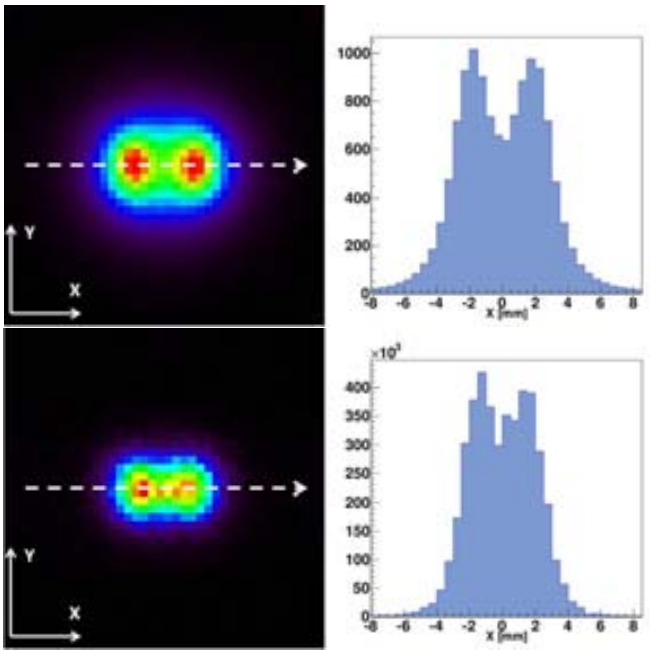

FIGURE 6.20: Images of the two point-like sources containing ^{18}F and separated by 4 mm. *Top:* Images of the central slice in the X-Y plane and line profiles over X axis, reconstructed with LM-OSEM. *Bottom:* Images of the central slice in the X-Y plane and line profiles over X axis, reconstructed with OE.

Figure 6.20 shows the images of two point-like sources containing ^{18}F and separated 4 mm. In this case the two points can be distinguished for both OE and LM-OSEM images. However, the image has less noise and the points can be more clearly distinguished in the case of LM-OSEM.

As is shown in figures 6.19 and 6.20, the two point sources can be resolved for both isotopes and with both image reconstruction algorithms. The positions of the peaks are consistent with the real positions of the two point-like sources. The FWHM of both peaks is also consistent with the PSF FWHM measured in section 6.4.1. The two point-like sources are resolved with a resolution better than 4 mm in case of ^{18}F and 7 mm in the case of ^{99m}Tc.

6.4.3 Point-like Sources with different activities.

In this section we will study the ability of the Compton camera to resolve different activity ratios between point-like sources. The test consists of the simulation of a phantom similar to the one described in the previous section. The phantom (shown in figure 6.21) consists of a parallelepiped with 10×10×30 mm^3 size, made from acrylic material. It

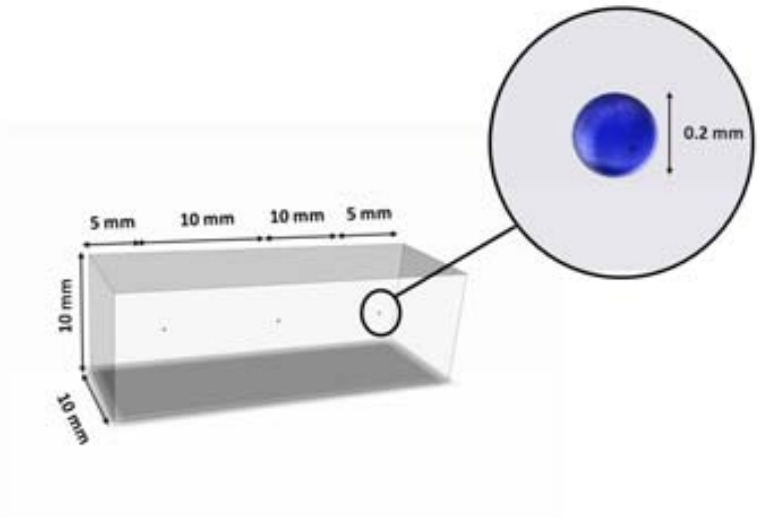

FIGURE 6.21: Phantom used for the three sources activity test.

contains three point-like sources separated 10 mm between each other. The sources have 10^5 Bq, $2 \cdot 10^5$ Bq, and $3 \cdot 10^5$ Bq activities of ^{18}F respectively. The phantom is placed at 10 cm from the scatterer edges, in such a way that the three points are aligned with the X axis.

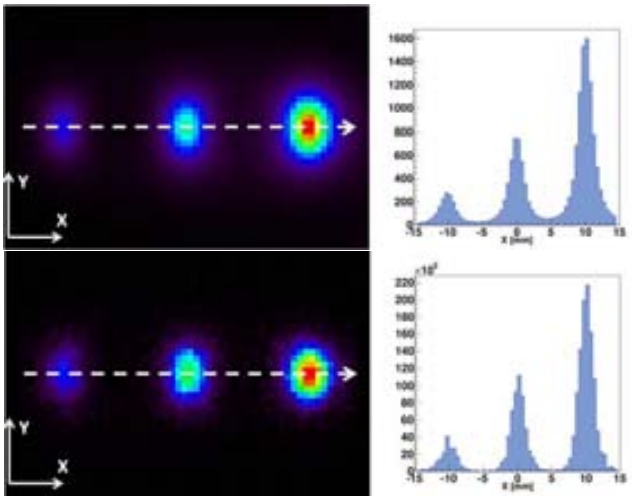

FIGURE 6.22: Images of the three point-like sources containing ^{18}F with increasing activities in a 1 : 2 : 3 ratio. *Top:* Images of the central slice in the X-Y plane and line profiles over X axis, reconstructed with LM-OSEM. *Bottom:* Images of the central slice in the X-Y plane and line profiles over X axis, reconstructed with OE.

The images are reconstructed from six million coincidences using OE and LM-OSEM algorithms. The image space a parallelepiped with sizes 30×20×20 mm^2, segmented into 0.5 mm voxels. In the case of OE, 100 iterations and 100 trials were performed in

order to obtain the images. For LM-OSEM, ten iterations were performed. In figure 6.22 the central image Z slice and the line profiles along the X axis are shown in the case of OE and LM-OSEM.

TABLE 6.5: Activity ratios between the sources. The content of the image voxels in a 10 mm cube centered in the point-like source. The result is normalized to the highest peak

Activity	OE	LM-OSEM
$1{\cdot}10^5$ Bq	1.16	1.32
$2{\cdot}10^5$ Bq	1.96	2.04
$3{\cdot}10^5$ Bq	**3**	**3**

To measure the activity ratios from the images we sum, for each one of the points, the content of the image voxels in a 10 mm cube centered in the point-like source. The result is normalized to the highest peak as it is the one with less spread. The obtained activity ratios are summarized in table 6.5. The obtained results show that with the Compton camera it is possible to distinguish between sources with different activities. The activity ratio is measured with an accuracy better than 70% for both algorithms.

6.5 Image Quality with a Horseshoe Phantom

In the previous sections the image resolution that the Compton camera can achieve was tested by simulating point-like sources. In this section we evaluate the quality of the images that can be obtained from the Compton camera comparing OE and LM-OSEM algorithms on a phantom with an extended source.

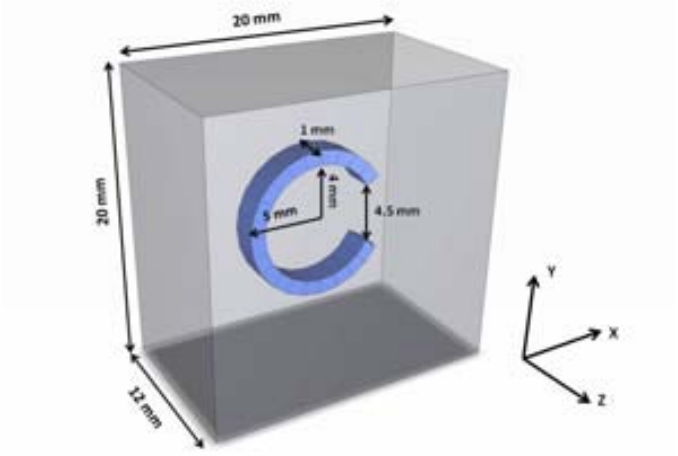

FIGURE 6.23: Scheme of the horseshoe phantom.

The data obtained from a scanned source is random as the emission process is a random process. This means that each time that a source is scanned different data is obtained and, hence, a different image will be produced. In order to assess the quality of the images produced with a given algorithm, sets of images produced from different data sets are compared with the true image which contains the exact map of activities in each image voxel. The image quality can be quantified [81] by the *bias*, the *variance*, and the *mean squared error* (MSE).

The bias is a measure of the accuracy of the image reconstruction algorithm defined by:

$$\text{Bias} = \frac{1}{N}\sum_{i=1}^{N}(\bar{X}_i - X_i^T)^2, \tag{6.1}$$

where N is the number of voxels in the image space, X^T is the true image, and $\bar{X}$ is the averaged image over the M images obtained:

$$\bar{X}_i = \frac{1}{M}\sum_{j=1}^{M} X_i^{(j)}, \tag{6.2}$$

where $X^{(j)}$ is the jth image of the set of images produced.

The variance is a measure of the consistency of the image reconstruction algorithm as it compares each of the images with the average image according to the equation:

$$\text{Variance} = \frac{1}{NM}\sum_{j=1}^{M}\sum_{i=1}^{N}(X_i^{(j)} - \bar{X}_i)^2. \tag{6.3}$$

Finally, the MSE for image $X^{(j)}$ is defined as:

$$\text{MSE} = \frac{1}{N}\sum_{i=1}^{N}(X_i^{(j)} - \bar{X}_i^T)^2. \tag{6.4}$$

The average MSE, which is a combination of the variance and the bias, is calculated as the arithmetic mean of the MSE obtained for each image.

In order to compare OE and LM-OSEM algorithm 10 images from different data sets are performed for each algorithm. The horseshoe phantom, shown in figure 6.23, consists of a "C" shape source with an inner radius of 4 mm, a thickness of 1 mm, and an aperture of 4.5 mm. The phantom is encased in a rectangular parallelepiped, made of acrylic material, with sides of 20 mm and a thickness of 12 mm. The source is filled with active water containing 10^5 Bq of the ^{18}F isotope. Using the same parameters described in section 6.1 a total of 22 million coincidence events are collected for each one of the images.

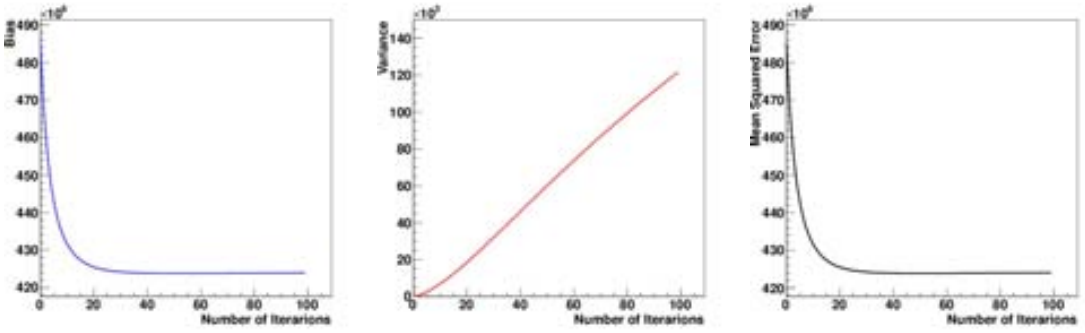

FIGURE 6.24: Image quality statistical values for horseshoe phantom using LM-OSEM algorithm.

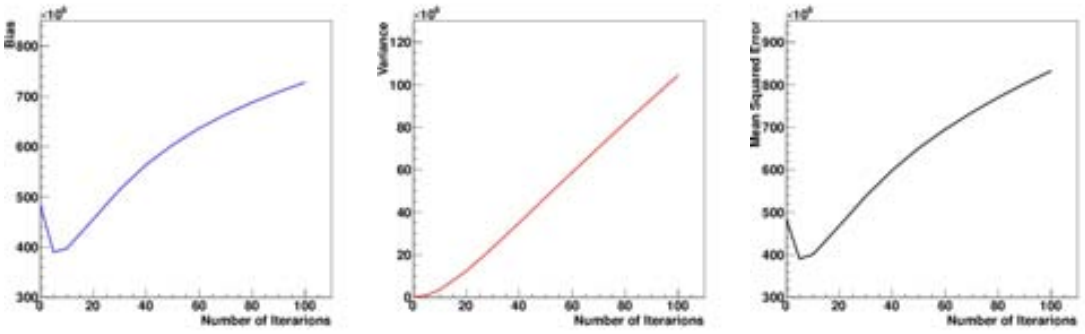

FIGURE 6.25: Image quality statistical values for horseshoe phantom using OE algorithm.

In the images produced by LM-OSEM only one subset is used for the reconstruction of the images. The use of more subsets makes the algorithm converge faster as less iterations are needed, but the obtained image cannot be obtained with the same accuracy. This is because the product of the number of subsets times the number of iterations, for the optimal image, is more or less a constant. With more subsets, less iterations are needed to reach the optimal solution but there is a chance to overshoot, since the optimal image might lie in between two subsequent iterations.

Figure 6.24 shows the obtained values of the bias, the variance, and the average MSE for increasing number of LM-OSEM iterations. The bias reaches a constant value as the algorithm converges. On the other hand, the variance grows with the number of iterations. The value of the bias is three orders of magnitude higher than the variance and, therefore, the effect of the increasing variance on the average MSE is very little.

The values of bias, variance, and MSE in the case of OE are shown in figure 6.25. With OE the bias reaches a minimum and begins to grow afterwards. The variance grows like in the case of LM-OSEM but now its value is comparable to the bias. The average MSE shows the same behavior as the bias but has higher value due to the higher

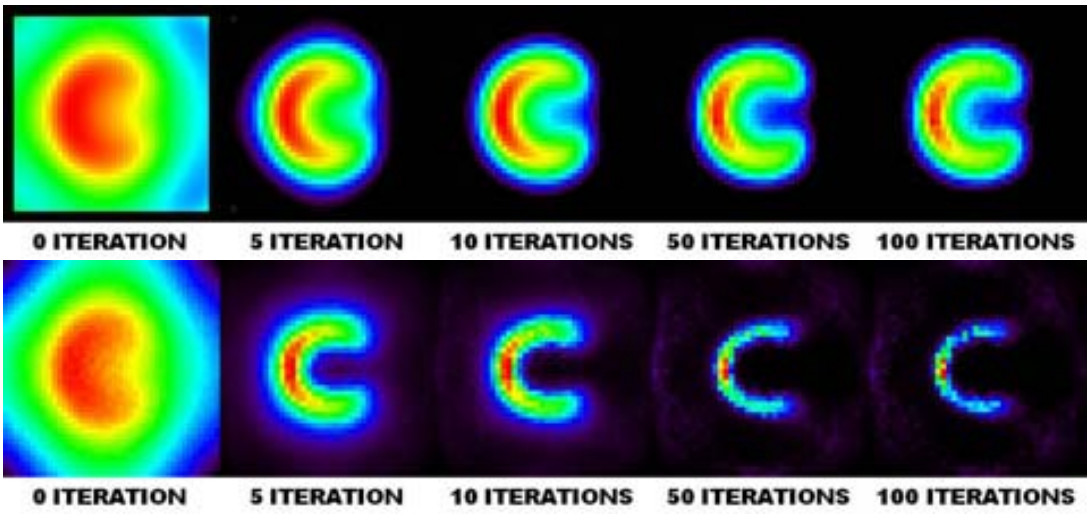

FIGURE 6.26: Reconstructed images of the Horseshoe phantom for different numbers of iterations using LM-OSEM (top) and OE (bottom).

variance. What this is indicating is that after OE has converged the image degrades with every iteration, diverging more and more from the true image. Therefore, the number of iterations to use is really important in order to obtain accurate images with OE. Unfortunately, it cannot be estimated a priory as it depends on the complexity of the phantom and on the number of coincidence events used to reconstruct the image.

The above conclusions are illustrated in figure 6.26 where we show images obtained from OE and LM-OSEM for increasing number of iterations. As can be seen the OE image degrades for increasing number of iterations while LM-OSEM stays constant, with images with similar quality.

The optimal images in the case of OE and LM-OSEM are shown in figure 6.27 together with the corresponding line profiles along Y direction. The distance between the peaks of the line profiles is 8.1 mm in the case of LM-OSEM and 7.15 mm in the case of OE, while the real value of the horseshoe diameter is 8.5 mm. Both the phantom shape and the 4.5 mm gap are very well recognized in the produced images.

This image quality study allows us to obtain the optimal number of iterations for OE and LM-OSEM. In the case of OE the optimal image is obtained after 10 iterations. The optimal image in the case of LM-OSEM is obtained for the minimum value of the bias at 40 iterations. LM-OSEM is a more robust image reconstruction method as the image does not degrade as quickly as with OE, when the optimal number of iterations is surpassed. LM-OSEM also requires less statistics to reconstruct the images than OE. With OE several trials are needed due to the stochastic nature of the algorithm increasing the computational power required required.

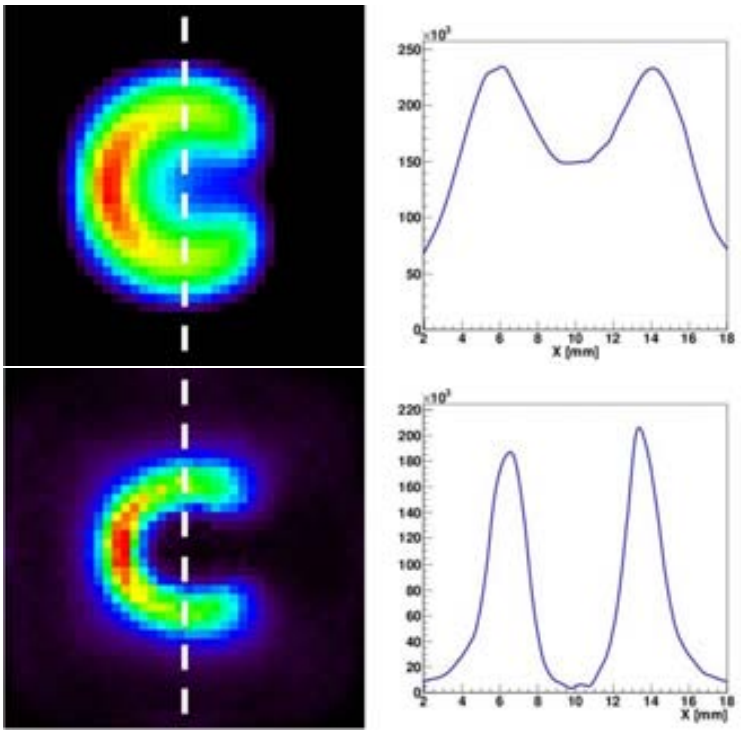

FIGURE 6.27: Images and line profiles of the horseshoe phantom for the optimal images obtained either with LM-OSEM or OE. In the case of LM-OSEM (top) 40 iterations are performed, while for OE 10 iterations and 100 trials were performed. The distance between the peaks is 8.1 mm for LM-OSEM and 7.15 mm for OE.

6.6 Image Reconstruction with Other Extended Phantoms

In the previous section the image quality of the Compton camera was evaluated by the use of the horseshoe phantom. The Compton imaging of extended sources adds an extra layer of complexity to the image reconstruction problem. Cones with origins at different locations in the FOV will intersect in complicated ways. In this section we will show the image recontruction capabilities of the Compton camera with some extended source phantoms.

The performance of LM-OSEM for the different scanners under study (PET, PEM, and Compton camera) has been evaluated and reported [77]. Figure 6.28 shows the image of one of the standard test phantoms for nuclear medicine: the Derenzo phantom. It consist of a cylinder divided in five segments, each of them containing rods with equal activity and varying diameter and distances. The image shown was reconstructed from 70 million simulated coincidence events using LM-OSEM. Two iterations of LM-OSEM were performed and the data was split into 70 subsets. The image space consists of 160×160×1 parallelepiped bins with size 0.5×0.5×12 mm^3. As can be seen in the image and the corresponding line profile, the 1.5 mm rods can be clearly distinguished

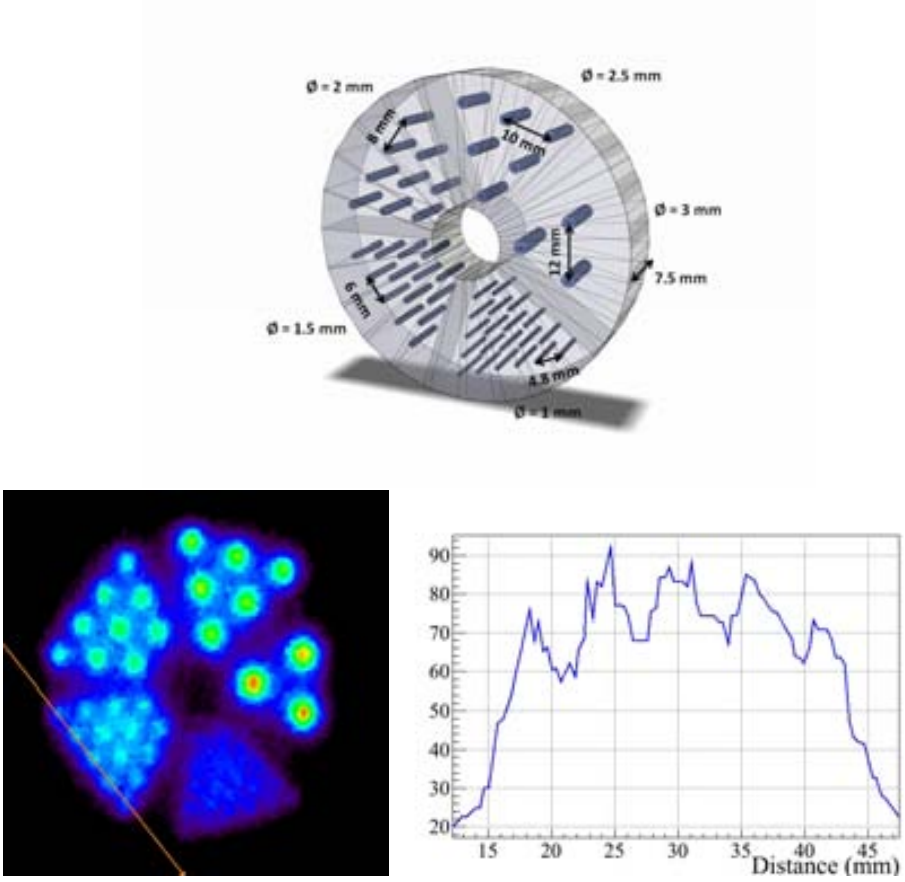

FIGURE 6.28: *Top:* scheme of the phantom. *Bottom:* reconstructed image with LM-OSEM and corresponding line profile of the 1.5 mm diameter rods. [77]

(see figure 6.28). This image is an important achievement as it shows the capabilities of the Compton camera to reconstruct complicated extended phantoms in a realistic simulation (including Doppler broadening, detector energy resolution, effect of voxel size, ...). The attempts to reconstruct the Derenzo phantom with the OE algorithm have been unsuccessful.

Another example is show in figure 6.29: a reconstructed image of a human brain slice phantom. The brain slice is simulated by using a DICOM file. The file has information of a 2D binned slice of a human brain containing the density information of the materials present inside the bins. An activity of 10^5 Bq of the ^{18}F isotope is simulated in the gray matter of the brain slice. A total of 34 million coincidence events were collected and 20 LM-OSEM iterations were performed in order to obtain the image. The image space is a parallelepiped consisting of 220×220×1 bins with size 1×1×5 mm^3. The gray matter structures in the image are clearly distinguishable and consistent with the anatomical distribution shown in the DICOM file.

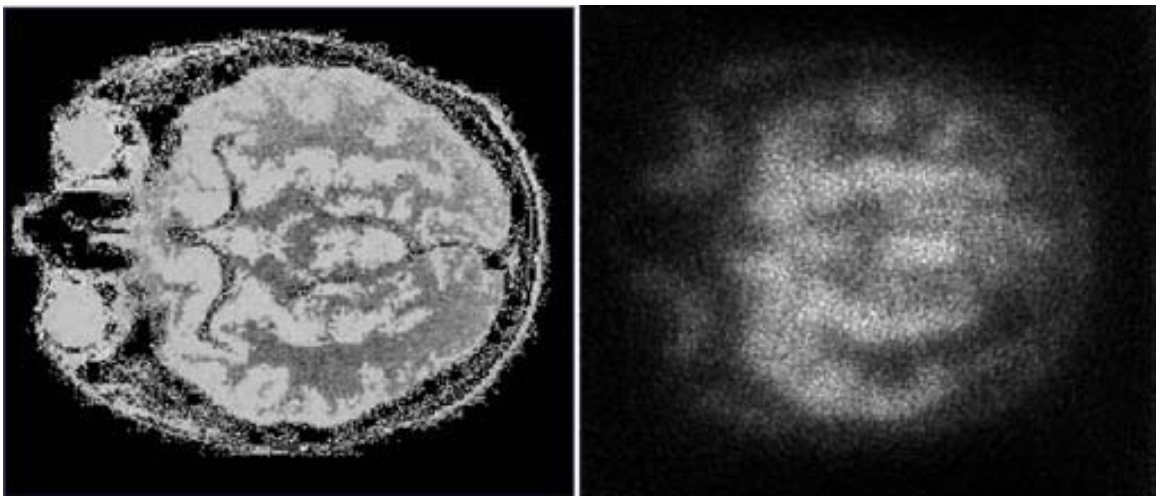

FIGURE 6.29: In the left we show a DICOM image corresponding to a brain slice. In the right the reconstructed image using the LM-OSEM algorithm.

The results shown above proves the imaging capabilities of the proposed Compton camera. There is still room for improvement as no transition matrix was used in LM-OSEM and no attenuation correction on the images was performed. The main limitation continues to be the computational power required. With more powerful computers and thanks to the pixelated solid-state technology developments, Compton cameras could be an important diagnosis and analysis device in nuclear medicine.

Chapter 7

Compton Camera Proof of Concept Prototype

As part of the experimental evaluation of the 3D detector packaging technology proposed by the VIP project, a prototype module detector unit using a different read-out ASIC has been designed. This chapter presents the simulation studies carried out in order to establish the feasibility of building a Compton camera prototype from these module units. These results have been already published [82].

In the following sections we will first describe the prototype and the different detector module unit. The efficiency of the prototype, the purity of the signal and the image spatial resolution will then be discussed.

7.1 Prototype Compton Camera Simulation

As in the case of the Compton camera discussed in chapter 3, the scatterer and absorber of the Compton camera prototype are built up from module detector units. An individual module contains an array of 2×4 CdTe detectors (see figure 7.1). The dimension of the CdTe detectors is 10 mm $\times$ 10 mm $\times$ 2 mm. The array of detectors are mounted on a 300 μm SiO_2 glass substrate placed upon a 100 μm flex-ridge kapton layer. The CdTe detectors are pixelated with a 2 mm $\times$ 1 mm $\times$ 2 mm voxel size.

The scheme of the module unit and of the complete prototype are shown in figure 7.1. The absorber is made by stacking 10 module units. In this way, we create a 4000 channels 3D voxel array with a density of 182 voxels/cm^3. The absorber's dimensions are 2 cm $\times$ 2 cm $\times$ 4 cm. The scatterer consists of just one module unit. The scatterer to absorber

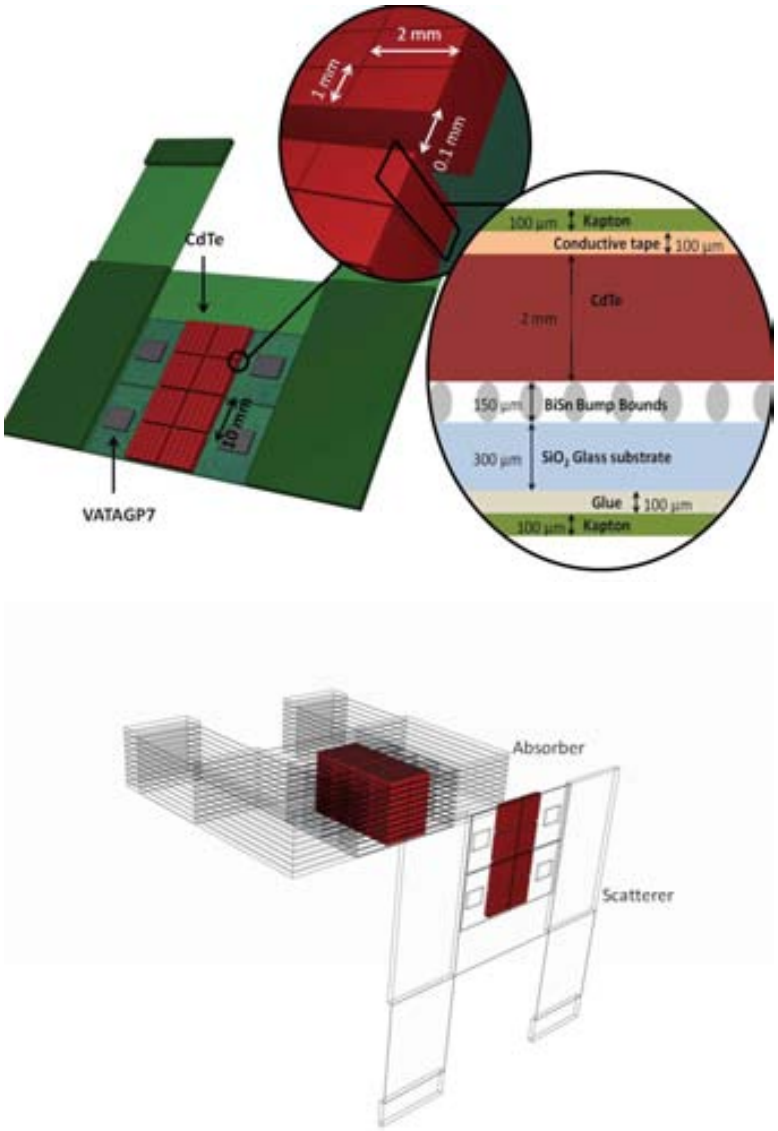

FIGURE 7.1: *Top:* Schematic of the module unit. *Bottom:* Compton camera built from module units. The scatterer is made with one single module while the absorber is the result of the stacking of 10 modules. The voxel density is 182 voxels/cm^3.

distance is set to 5 cm. The absorber is vertically stacked in such a way that the detector can easily be made bigger by simply adding more modules (see figure 7.1).

The read-out of the 400 channels present in each module unit is performed by four VATAGP7 ASICs[1][2]. VATAGP7 is a 128-channel self-triggered charge-efficiency amplifier. The energy resolution characterization of the pixelated CdTe detectors has been performed and reported [27].

[1]Gamma Medica webpage: http://www.gammamedica.com/
[2]Ideas webpage: http://ideas.no/

TABLE 7.1: Camera Prototype Parameters

Detector	
Measuring Time	500 ns
Dead Time	51.2 μs
Time Resolution	100 ns
Trigger Threshold	20 keV
System	
Area	20 mm $\times$ 40 mm
Scatterer Thickness	2 mm
Absorber Thickness	20 mm
Scatterer to Absorber Distance	50 mm

The simulation of the prototype is performed with GAMOS as described in chapter 4. The data from the simulation is processed by a modified version of the C++ detector response simulation code discussed in section 4.2.2 of chapter 4. The modifications affect the data acquisition process and are due to the differences in behavior of the VATAGP7 ASIC with respect to the VIP-PIX.

After the data acquisition, the coincidence selection algorithm processes the data in order to group consecutive hits inside a 100 ns coincidence time window. Events with a single hit in the scatterer and a single hit in the absorber are selected as candidates, of which only the ones in which the combined energy of the hits is 511 keV with a $\pm 1.57\%$ tolerance are taken as coincidence events. All the parameters used in the simulation are summarized in table 7.1.

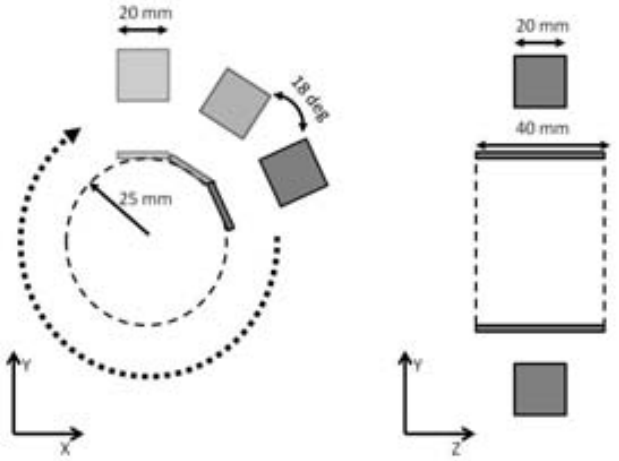

FIGURE 7.2: The camera is rotated creating a cylindrical FOV of 25 mm radius and 40 millimeters length.

All the images that we will show are reconstructed by using the OE algorithm discussed in chapter 5. The distance between the different sources used (placed at the FOV center) and the scatterer edge is 25 mm in all the simulations. Since the FOV is smaller (20×20 mm^2) than in the standard VIP Compton camera, the range of angles covered by the detector is also smaller. OE uses the density of cones crossing the image space voxels in order to reconstruct the image. With the small FOV the density of cones is high enough to create artifacts in the images reconstructed with OE. In order to overcome this limitation we rotate the detector at constant time intervals covering the 360 degree circumference in twenty steps of 18 degrees each (see figure 7.2). This creates a cylindrical FOV of 25 mm radius and 40 mm length.

7.2 Efficiency and Signal Purity

In order to measure the source activity range in which the system can operate and evaluate the efficiency of the camera, different simulations have been performed. The same point-like phantom described in section 6.1 of chapter 6 will be used in all the efficiency tests. The gamma photon source will be the ^{18}F isotope in all simulations.

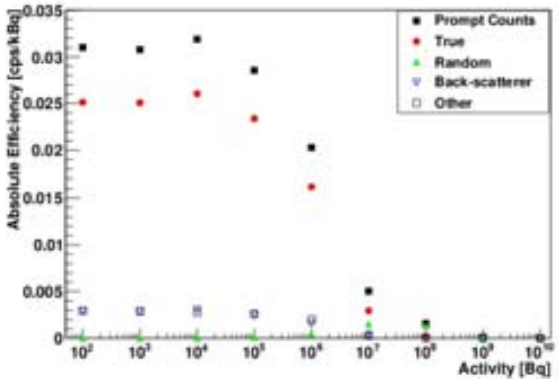

FIGURE 7.3: Absolute efficiency versus source activity and event classification.

In figure 7.3 we show the absolute efficiency of the Compton camera (i.e., the number of coincidence events divided by the total number of emitted gammas in all directions) in counts per second per kBq for increasing activities. The events are classified as "true", "random" (i.e., coming from two unrelated gammas), "back-scattering" (i.e., gammas that make a high energetic Compton interaction in the absorber and scatter back to the scatterer where they are absorbed) or "other". The main contribution to the "other" category are events with more than one hit in scatterer or absorber but in which the extra hits are below trigger threshold. One can see that the count rate begins to drop at 10^5 Bq and the camera is completely saturated at 10^9 Bq. The absolute efficiency is

0.03 cps/kBq for activities $< 10^5$ Bq. The fraction of true events over the total number of coincidence events is 81% in the entire non-saturated range. For all the following simulations the activity is set at 10^4 Bq where the saturation effects are negligible.

In order to compare the obtained efficiency with commercially available SPECT systems, one needs to compute the intrinsic efficiency (i.e., the number of coincidence events divided by the gammas that reach the detector). For a point-like source in the center of the FOV, absolute and intrinsic efficiencies are related by the following formula:

$$\epsilon_{int} = \epsilon_{abs} \cdot (\frac{4\pi}{\Omega}), \tag{7.1}$$

where ϵ_{int} is the intrinsic efficiency, ϵ_{abs} is the absolute efficiency, and Ω is the solid angle covered by the detector. The obtained intrinsic efficiency of the Compton camera prototype is 0.4 cps/kBq.

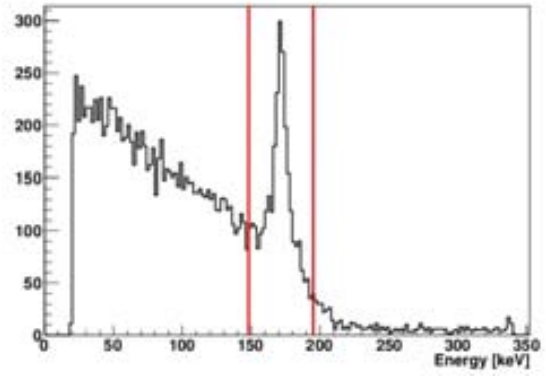

FIGURE 7.4: Energy depositions on the scatterer detector. The peak at 171 keV corresponds to back-scattering events. The red lines indicate the cut applied around the back-scattering peak to eliminate those events.

Approximately 10% of the total number of events are due to "back-scattering". If these events can be identified, one can reconstruct a Compton cone from the absorber interaction and include them in the image reconstruction. Otherwise, these events contribute to the noise as they will yield a wrong Compton angle as it is calculated under the assumption that the Compton scattering took place in the scatterer and the absorption in the absorber, instead of the other way around. Due to the small size of the detectors compared to the scatterer to absorber distance the "back-scattering" events are distributed in a well defined peak on the energy spectrum, as seen in figure 7.3. The simplest way to eliminate the back-scattered events is to fit the "back-scattering" peak and cut all the events in a fixed range around the peak mean.

As it has been shown [18], silicon is a superior choice as scatterer detector material because of its reduced Doppler broadening effect and its bigger Compton cross section

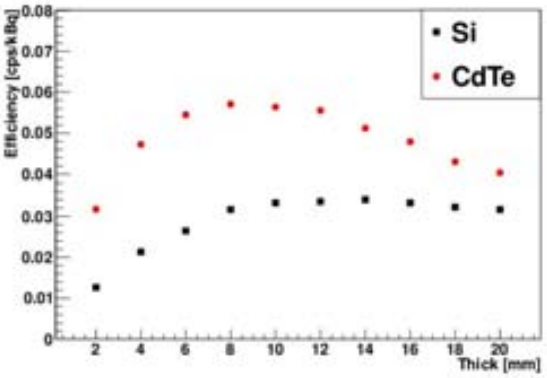

FIGURE 7.5: Absolute efficiency of the Compton camera for different scatterer thickness. The black squares correspond to Si and the red circles to $CdTe$.

for low energy gammas (e.g., as emitted by ^{99m}Tc). However, for 511 keV gammas a thicker scatterer is needed if one uses silicon. In figure 7.5 the absolute efficiency of the Compton camera prototype is computed when $CdTe$ is substituted with Si in the scatterer detector. For 511 keV gammas at least four module units containing 2 mm thick Si detectors must be stacked above each other to match the efficiency of a single layer of CdTe.

7.3 Image Reconstruction

7.3.1 Point-like source.

In order to characterize the image spatial resolution we can expect from the prototype, an image of the point-like source phantom in the center of FOV is reconstructed from 10 thousand coincidence events. A total of 1000 iterations and 100 trials were performed in order to obtain the images shown in figure 7.6. The image FOV is $20 \times 20 \times 20$ mm^3, segmented in cubic bins with sides of 0.5 mm. The z-axis is defined as the rotation axis of the Compton camera prototype. The behaviour of the camera in all the directions perpendicular to the z-axis is expected to be the same due to the cylindrical symmetry created by the rotation.

The FWHM of the PSF along the axial direction (z-axis) is 1.5 mm while in the radial directions (any direction perpendicular to z-axis) the FWHM of the PSF is 2.2 mm. As was explained in section 6.4.1 of chapter 6, the PSF FWHM will be worse along the directions perpendicular to the scatterer edge than in the directions parallel to it. In the case of the Compton camera prototype only the z-axis is parallel to the scatterer edge

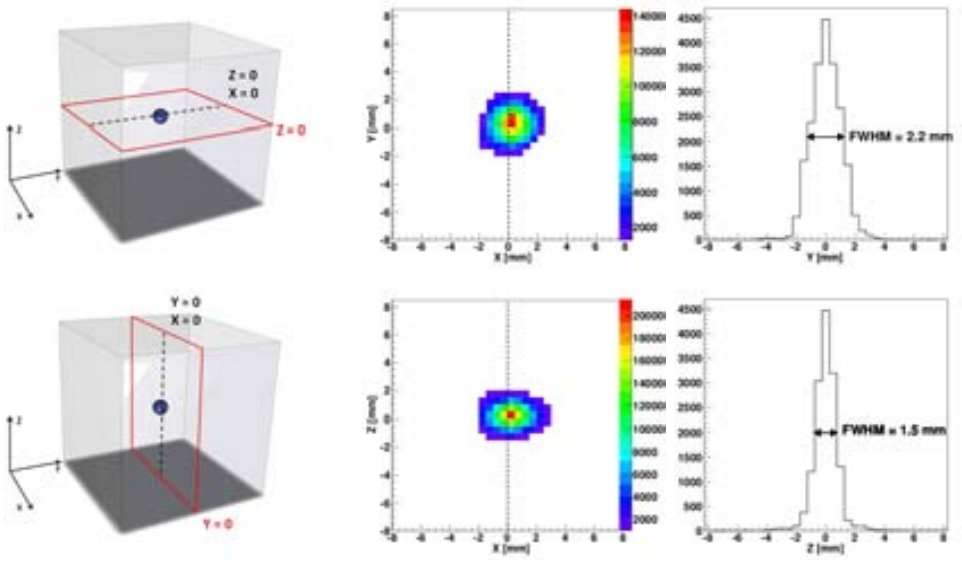

FIGURE 7.6: Point-Spread-Function. *Top left:* Representation of the phantom. *Top center:* Image of a central slice in the X-Y plane. *Top right:* Line profile along Y direccion. FWHM is equal in X and Y directions. *Bottom left:* Representation of the phantom. *Bottom center:* Image of a central slice in the X-Z plane. *Bottom right:* Line profile along Z direccion. FWHM is smaller along Z axis which corresponds to the FOV cylinder axis.

as the camera rotates. Comparable spatial resolution is obtained with Compton camera prototypes using Double-sided Silicon Strip Detectors (DSSD) for the scatterer [24].

7.3.2 Two point-like sources.

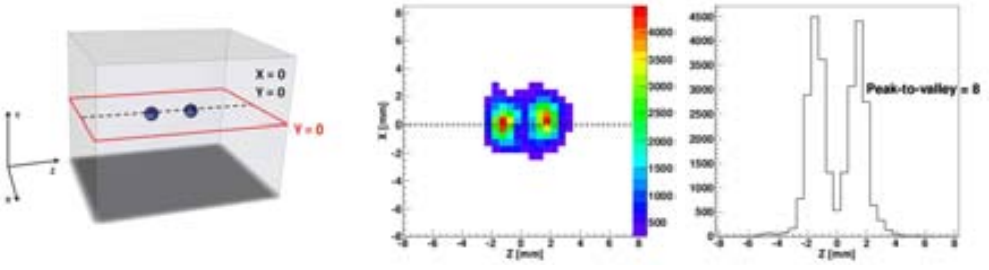

FIGURE 7.7: Two points with 3 mm distance. *Left:* Representation of the phantom. *Center:* Image of a central slice containing both sources. *Right:* Line profile along Z direction.

To test the resolving power of the prototype we simulated two point-like sources with 3 mm separation. In the simulation we use a modified version of the phantom used for the single point-like source. It consists of a rectangular acrylic block with 10×10 mm^2 base area and 13 mm height. Two 0.1 mm spheres are placed at 1.5 mm from the center of the acrylic block along the longest direction. The phantom is placed with respect to

the camera in such a way that the sources are aligned with the axial direction of the cylindrical FOV.

The image is reconstructed using 20 thousand coincidence events. The two point-like sources can be clearly distinguished with a peak-to-valley ratio of 8 as seen in figure 7.7. The PSF for each of the points remains equal at 1.5 mm FWHM.

7.3.3 Point-like sources with different activities.

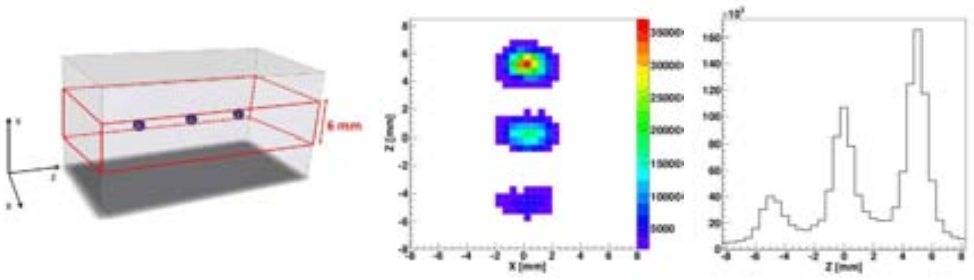

FIGURE 7.8: Three points with different activities. *Left:* Representation of the phantom. *Center:* Image of 6 mm thick central slice. *Right:* Projection along Z direction.

The ability to accurately distinguish different activities is important to differentiate the signal from background activity and to distinguish different tissues in real medical applications.

In order to quantify the accuracy of our Compton camera when reconstructing different activities, we used a phantom with the same dimensions of the one used with two point-like sources, but now it contains three point-like sources with 5 mm separation and activity ratios of 1:2:3 times 100 kBq. In figure 7.8 the image reconstructed from 30 thousand coincidence events is shown.

To measure activity ratios from the image we fit to a Gaussian function each one of the three peaks and integrate all the events in a region of five sigma around the mean value. Normalizing the result to the lowest peak we obtain a ratio between the activities of 1:2.4:3.2. Hence the activity ratio is measured with an accuracy better than 80%.

7.3.4 Point-like source on cube vertices.

To show the full 3D imaging capabilities of the Compton camera we simulate an array of point-like sources arranged in the vertices of a cube. The phantom used in the simulation is again a modified version of the one used for the point-like source. It consists of a cube with sides of 15 mm length made of acrylic material which contains eight point-like sources of radio-tracers placed at the vertices of another cube with sides of 10 mm, see

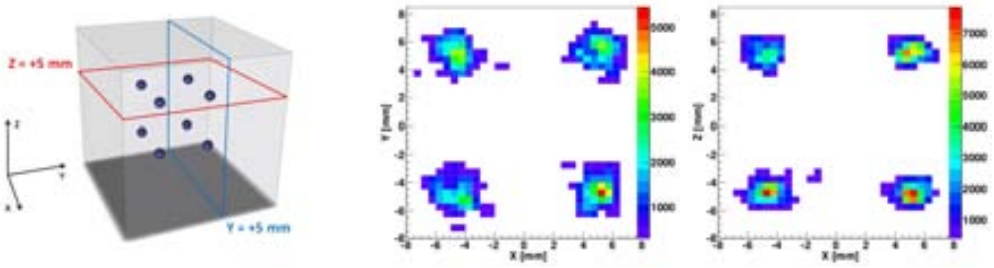

FIGURE 7.9: Points arranged in a cube. *Left:* Representation of the phantom. *Center:* Image of 6 mm thick X-Y slice covering the first 4 sources in the Z direction. *Right:* Image of 6 mm thick X-Z slice covering the first 4 sources in the Y direction.

figure 7.9. The image FOV used by OE is $20 \times 20 \times 20$ mm^3 divided in cubic bins with sides of 0.5 mm.

The image reconstructed using 80 thousand coincidence events of a three dimensional array of eight points in the vertices of a cube is shown in figure 7.9. Two slices of the fully reconstructed 3D image with different plane orientation are shown. The FWHM is consistent with the PSF analysis and the points are clearly distinguishable and with compatible intensities.

7.4 Conclusion

In this chapter we have presented a simulation study of a Compton gamma camera prototype, under construction, that has pixelated *CdTe* detectors, stacked above each other, to form a true 3D detector.

The prototype has an absolute efficiency of 0.03 cps/kBq for activities below 10^5 Bq. The purity of the collected coincidence events is 81% in the entire non-saturated range. The obtained efficiency value is enough to perform laboratory tests, like small animal molecular imaging, as enough coincidence events can be collected in a reasonable amount of time ($\sim$ 25 k coincidence event per day with 10^4 activity).

The image resolution is measured as the FWHM of the PSF reconstructed with the OE algorithm. The obtained FWHM is 2.2 mm along the radial direction of the cylindrical FOV, and 1.5 mm along the axial direction. This PSF values are confirmed by simulating two point-like sources at 3 mm distance. The two points are clearly distinguished in the reconstructed image. The obtained image resolution is comparable with the one obtained by other Compton camera prototypes [24]. The 3D imaging capabilities and the ability to distinguish different activity ratios are also shown through the simulations. The obtained values of the PSF FWHM are better than the ones obtained in chapter 6 for

the VIP Compton camera. The reason for this is that the phantoms are placed closer to the scatterer edge (2.5 cm in the case of the prototype and 10 cm in the case of the full camera) resulting in a lower angular error.

These simulation results are promising and encouraging to set the case to construct high density stacked pixelated CdTe detectors. A first layer of the detector has already been built and characterized [83]. The presented prototype serves as a proof of concept to construct a detector with similar design but with a larger area, e.g 30 cm x 30 cm, that matches the common needs of the nuclear medical imaging practice.

Chapter 8

Closing Remarks

The VIP project proposes a novel detector design that uses pixelated solid-state CdTe detector. The modular design of the detectors allows to apply the same detector concept to different scanners like PET, PEM and Compton camera. The work presented in this thesis evaluates the VIP Compton camera design, with a scatterer made of Silicon and an absorber made of CdTe. All channels of the VIP Compton camera design have an independent read-out.

The Compton camera design presented in chapter 3 is evaluated using Monte Carlo simulations. The full camera, the different sources, and the physics are simulated using the GAMOS framework. GAMOS (see chapter 4) allows to perform Geant4 simulations using a simple scripting language. The effect of detector energy resolution, the voxel size, and the Doppler broadening effect are all included in the simulation.

A big challenge for Compton cameras is the image reconstruction. Two image reconstruction methods are used in this thesis: OE and LM-OSEM. With OE, for each coincidence event, a random position is assigned within the surface defined by the corresponding Compton cone. In each OE iteration a new random position is calculated for each event and accepted with a probability which depends on the density of events in the old and new locations. Due to the stochastic nature of OE several trial runs must be performed and averaged in order to avoid random fluctuations. LM-OSEM, on the other hand, uses the EM algorithm to obtain the most probable image for a given list of coincidences. LM-OSEM is a fast and robust algorithm which allows to avoid the main drawbacks of the standard MLEM algorithm. Both algorithms (and some others) are described in detail in chapter 5.

In chapter 6 the Compton camera design is evaluated using Monte Carlo simulations. The efficiency of the camera for different thicknesses of the scatterer (Si) and the absorber

(CdTe) detectors, is obtained through Monte Carlo simulations using the ^{99m}Tc (141 keV gamma emitter) and ^{18}F (positron emitter, producing electron-positron annihilation gamma photons with energy 511 keV) isotopes. For a scatterer thickness of 2 cm and an absorber thickness of 4 cm, the obtained efficiency is 9.4 cps/kBq for ^{18}F and 8.8 cps/kBq for ^{99m}Tc. However, having two Compton cameras at different angles, with an absorber of smaller thickness (e.g. 2 cm), would result in better efficiency and better image resolution for the same cost.

The maximum activity in which the camera can operate and the different kinds of false coincidence events are also studied in chapter 6. The results show that for both ^{18}F and ^{99m}Tc the camera can operate with activities up to 10^6 Bq with optimum efficiency and is completely saturated at 10^9 Bq. The number of true events amounts to 93% of the detected coincidences in the case of ^{18}F and 81.32% in the case of ^{99m}Tc. The main contribution to the false coincidences are the back-scattering events which constitutes the 4.45% of the coincidence events in the case of ^{18}F, and the 9.74% in the case of ^{99m}Tc. The scattered events are mostly rejected thanks to the excellent energy resolution of the detectors. In the case of ^{18}F only 2.53% of the detected coincidences are scattered events, this number increases to 7.87% for ^{99m}Tc.

In order to increase the efficiency of the camera, a method to reconstruct coincidence events composed by three hits is also presented. The method uses the Compton kinematics to identify the order of the sequence of hits. The simulation results, using ^{18}F, show that 43% of the coincidences with three hits can be recovered with a purity (i.e., fraction of correctly reconstructed over all the reconstructed) of 93%. This allows to add 2.87 cps/kBq to the camera efficiency.

The image resolution of the camera is evaluated by measuring the PSF FWHM for the ^{18}F and ^{99m}Tc isotopes. The OE and LM-OSEM algorithms are used to reconstruct the PSF. The obtained values are shown in table 6.3. Different values of the PSF FWHM are obtained for the different spatial directions. In the case of the directions parallel to the scatterer plane the different resolution is due to the asymmetry in the detector voxels. The worst image resolution is obtained in the direction orthogonal to the scatterer plane due to the fact that the Compton cones are predominantly oriented in this direction. The asymmetry in the PSF can be eliminated by collecting coincidence events from two orthogonal directions, i.e., placing the camera in two orthogonal directions with respect to the source.

The obtained values of the PSF FWHM are tested by simulating two point-like sources at distances comparable to the FWHM (1.5 times the FWHM). In the case of ^{18}F, the point sources are resolved at a distance of 4 mm, while for ^{99m}Tc they are resolved at 7

mm. For both isotopes and both image reconstruction algorithms the two point sources can be clearly distinguished in the obtained images.

We also tested the accuracy of the camera in distinguishing between sources with different activities. Three point sources with activity ratios 1:2:3 were simulated. The simulation shows an accuracy better than 70% on the reconstructed ratios.

The quality of the images produced by OE and LM-OSEM was evaluated for an extended phantom using standard statistical methods. The obtained results shows that the images obtained from OE degrades quickly if more than the optimal number of iterations are performed. LM-OSEM, on the other hand, shows a more consistent behavior, with higher mean squared error than OE, but with very little image degradation when more iterations than needed are performed.

The image capabilities of the camera when imaging extended and complex phantom are shown in the last section of chapter 6 where we show the reconstructed images of the Derenzo phantom and of a human brain slice. These images are an important achievement as they show that the camera is able to reconstruct the images of complicated extended phantoms. The images were reconstructed with LM-OSEM. OE is not able to separate the smaller details of these phantoms.

A proof of concept Compton camera prototype is evaluated in chapter 7. The prototype is a small FOV Compton camera using CdTe as detector material for both the scatterer and the absorber. Similar tests to those performed for the VIP Compton camera are performed in order to study the performance of the prototype. The prototype is able to operate with activities up to 10^4 Bq without pile-up events. The obtained efficiency is 0.03 cps/kBq, much lower than in the full camera due to the smaller FOV. The image resolution of the prototype is evaluated by simulating point-like source phantoms (similar to those used previously in chapter 6) containing ^{18}F. All the images are reconstructed with the OE algorithm. The PSF obtained is smaller than the one obtained with the full camera as the phantoms are placed closer to the scatterer edge. The values of the PSF are tested by resolving two point-like sources at 3 mm distance. The accuracy in distinguishing sources with different activities is also shown.

The simulation tests performed show that the proposed Compton camera design yields higher efficiency than commercially available SPECT. The reconstructed PSFs for ^{18}F and ^{99m}Tc point sources also show that the image resolution is better than the one obtained with commercial SPECT in similar conditions. These results are possible thanks to the excellent energy and spatial resolution of the solid state detectors, and the developments in the image reconstruction field.

The studies performed in this thesis are encouraging for further research in Compton imaging. However, the simulations performed must be validated with real data. There is room for improvement in the image reconstruction (for example including physics and detector response models in the transition matrix in the case of LM-OSEM). The image reconstruction requires high computational resources but more powerful computers will be available in the future reducing the time needed to obtain the images.

The VIP project will produce 120 module detector units during 2014. Two stacks of 60 modules will be built. The stacks will be used as a proof of concept PET prototype, but due to the flexibility of the design they can also be used to make a PEM prototype or as absorber detector for a Compton camera prototype. The obtained data from such a prototype can set a milestone for the research on Compton cameras for medical applications.

Appendix A

Central Slice Theorem

Consider a two dimensional source with an activity density given by $f(x, y)$. If we define a rotated coordinate reference frame $\{x', y'\}$ with a counter-wise rotation angle θ we can define the projection data in the y' direction as the line integral of the image in this direction:

$$p(x', \theta) = \int_{-\infty}^{+\infty} f(x, y) dy'. \tag{A.1}$$

The $\{x, y\}$ coordinates and the rotated coordinates $\{x', y'\}$ are related through the rotation matrix corresponding to a counter-clockwise rotation:

$$\begin{pmatrix} x \\ y \end{pmatrix} = \begin{pmatrix} \cos\theta & -\sin\theta \\ \sin\theta & \cos\theta \end{pmatrix} \begin{pmatrix} x' \\ y' \end{pmatrix}. \tag{A.2}$$

We define the one dimensional Fourier transform and its inverse as:

$$H(\omega_x) = \mathcal{F}_1\{h(x)\} = \int_{-\infty}^{+\infty} h(x) e^{-i2\pi\omega_x x} dx \tag{A.3}$$

$$h(x) = \mathcal{F}_1^{-1}\{H(\omega_x)\} = \int_{-\infty}^{+\infty} H(\omega_x) e^{i2\pi\omega_x x} d\omega_x, \tag{A.4}$$

where ω_x are the frequencies corresponding to the x coordinate and $h(x)$ is an arbitrary function.

The Fourier transform of the projection $p(x', \theta)$ is given by

$$P(\omega'_x, \theta) = \int_{-\infty}^{+\infty} p(x', \theta) e^{-i2\pi\omega'_x x'} dx'. \tag{A.5}$$

Using equation (A.1) we obtain

$$\begin{aligned} P(\omega'_x, \theta) &= \int_{-\infty}^{+\infty} \int_{-\infty}^{+\infty} f(x,y) e^{-i2\pi\omega'_x x'} dx' dy' \\ &= \int_{-\infty}^{+\infty} \int_{-\infty}^{+\infty} f(x,y) e^{-i2\pi\omega'_x (x\cos\theta + y\sin\theta)} dx dy \\ &= F(\omega'_x \cos\theta, \omega'_x \sin\theta). \end{aligned} \tag{A.6}$$

Where we have used the invariance under rotation of the surface element[1] $dxdy$ and the two dimensional Fourier transform of $f(x,y)$ defined as

$$F(\omega_x, \omega_y) = \mathcal{F}_2\{f(x,y)\} = \int_{-\infty}^{+\infty} \int_{-\infty}^{+\infty} f(x,y) e^{-i2\pi\omega_x x} e^{-i2\pi\omega_y y} dx dy. \tag{A.7}$$

In order to clarify the meaning of the equation (A.6) we can write the Fourier transform of the image $F(\omega_x, \omega_y)$ in terms of the frequencies on the rotated reference frame defined by

$$\begin{pmatrix} \omega_x \\ \omega_y \end{pmatrix} = \begin{pmatrix} \cos\theta & -\sin\theta \\ \sin\theta & \cos\theta \end{pmatrix} \begin{pmatrix} \omega'_x \\ \omega'_y \end{pmatrix}, \tag{A.8}$$

obtaining:

$$F(\omega'_x, \omega'_y) = \int_{-\infty}^{+\infty} \int_{-\infty}^{+\infty} f(x,y) e^{-i2\pi(\omega'_x \cos\theta - \omega'_y \sin\theta)x} e^{-i2\pi(\omega'_x \sin\theta + \omega'_y \cos\theta)y} dx dy. \tag{A.9}$$

By the comparison of equations (A.6) and (A.9) one can realize the following relation:

$$P(\omega'_x, \theta) = F(\omega_x, \omega_y)|_{\omega'_y = 0}. \quad \square \tag{A.10}$$

The above result, known as the *Central Slice Theorem*, states that the Fourier transform of the projection data in a direction $P(\omega'_x, \theta)$ is equal to the central slice perpendicular to the projection direction (defined by the condition $\omega'_y = 0$) of the Fourier transform $F(\omega_x, \omega_y)$ of the image $f(x,y)$.

[1] Which can be easily proven by calculating the Jacobian matrix corresponding to the variable change, which is equal to the rotation matrix. The absolute value of the determinant of the Jacobian matrix is therefore one.

Bibliography

[1] W. D. Coolidge and E. E. Charlton. X-ray history and development. *Electrical Engineering*, 64(12):427–432, Dec 1945. ISSN 0095-9197. doi: 10.1109/EE.1945.6441361.

[2] R. W. Todd, J. M. Nightingale, and D. B. Everett. A proposed [gamma] camera. *Nature*, 251(5471):132–134, Sep 1974. doi: 10.1038/251132a0.

[3] M. Chmeissani, P. Arce, and M. Canadas. Modeling and simulation of PET scanner based on pixelated solid-state detector. In *Nuclear Science Symposium Conference Record (NSS/MIC), 2009 IEEE*, pages 3496–3502, 2009. doi: 10.1109/NSSMIC.2009.5401799.

[4] H. Anger. A new instrument for mapping gamma-ray emitters. *Biology and Medicine Quarterly Report UCRL*, 3653(38), 1957.

[5] P. J. Slomka, D. Dey, W. L. Duvall, M. J. Henzlova, D. S. Berman, and G. Germano. Advances in nuclear cardiac instrumentation with a view towards reduced radiation exposure. *Curr Cardiol Rep*, 14(2):208–216, Apr 2012. doi: 10.1007/s11886-012-0248-z.

[6] N.U. Schramm, G. Ebel, U. Engeland, T. Schurrat, M. Behe, and T. M. Behr. High-resolution spect using multipinhole collimation. *Nuclear Science, IEEE Transactions on*, 50(3):315–320, 2003. ISSN 0018-9499. doi: 10.1109/TNS.2003.812437.

[7] O. Schillaci, E. Cossu, P. Romano, C. Sanso, R. Danieli, A. V. Granai, G. Caravaglia, C. A. Pistolese, O. Buonomo, and G. Simonetti. High-resolution gamma-camera for molecular breast imaging: First clinical results. *Phys Med*, 21 Suppl 1: 121–124, 2006.

[8] C. Fiorini, P. Busca, R. Peloso, A. Abba, A. Geraci, C. Bianchi, G. L. Poli, G. Virotta, K. Erlandsson, B. F. Hutton, P. Lechner, H. Soltau, L. Struder, A. Pedretti, P. Van Mullekom, L. Ottobrini, and G. Lucignani. The HICAM gamma camera. *Nuclear Science, IEEE Transactions on*, 59(3):537–544, 2012. ISSN 0018-9499. doi: 10.1109/TNS.2012.2192940.

[9] S. S. Gambhir, D. S. Berman, J. Ziffer, M. Nagler, M. Sandler, J. Patton, B. Hutton, T. Sharir, S. B. Haim, and S. B. Haim. A novel high-sensitivity rapid-acquisition single-photon cardiac imaging camera. *J. Nucl. Med.*, 50(4):635–643, Apr 2009. doi: 10.2967/jnumed.108.060020.

[10] M. Singh. An electronically collimated gamma camera for single photon emission computed tomography. *Medical Physics*, 10(4):421–435, Aug 1983. doi: 10.1118/1.595313.

[11] O. Klein and Y. Nishina. Über die streuung von strahlung durch freie elektronen nach der neuen relativistischen quantendynamik von dirac. *Zeitschrift für Physik*, 52(11-12):853–868, 1929. ISSN 0044-3328. doi: 10.1007/BF01366453. URL http://dx.doi.org/10.1007/BF01366453.

[12] G.F. Knoll. *Radiation detection and measurement*. Wiley, 2000. ISBN 9780471073383.

[13] N. H. Clinthorne. A method for improving the spatial resolution of a compton camera. *U.S. Patent 6,323,492*, Nov 2001.

[14] Stefano Del Sordo, Leonardo Abbene, Ezio Caroli, Anna Maria Mancini, Andrea Zappettini, and Pietro Ubertini. Progress in the development of CdTe and CdZnTe semiconductor radiation detectors for astrophysical and medical applications. *Sensors*, 9(5):3491–3526, 2009. ISSN 1424-8220. doi: 10.3390/s90503491. URL http://www.mdpi.com/1424-8220/9/5/3491.

[15] Alan Owens and A. Peacock. Compound semiconductor radiation detectors. *Nuclear Instruments and Methods in Physics Research Section A: Accelerators, Spectrometers, Detectors and Associated Equipment*, 531(1–2):18 – 37, 2004. ISSN 0168-9002. doi: http://dx.doi.org/10.1016/j.nima.2004.05.071. URL http://www.sciencedirect.com/science/article/pii/S0168900204010575. Proceedings of the 5th International Workshop on Radiation Imaging Detectors.

[16] A.G. Kozorezov, J.K. Wigmore, A. Owens, R. den Hartog, A. Peacock, and Hala A Al-Jawhari. Resolution degradation of semiconductor detectors due to carrier trapping. *Nuclear Instruments and Methods in Physics Research Section A: Accelerators, Spectrometers, Detectors and Associated Equipment*, 546(1–2):209 – 212, 2005. ISSN 0168-9002. doi: http://dx.doi.org/10.1016/j.nima.2005.03.026. URL http://www.sciencedirect.com/science/article/pii/S0168900205006303. Proceedings of the 6th International Workshop on Radiation Imaging Detectors Radiation Imaging Detectors 2004 6th International Workshop on Radiation Imaging Detectors.

[17] R. C. Alig, S. Bloom, and C. W. Struck. Scattering by ionization and phonon emission in semiconductors. *Phys. Rev. B*, 22:5565–5582, Dec 1980. doi: 10.1103/PhysRevB.22.5565. URL http://link.aps.org/doi/10.1103/PhysRevB.22.5565.

[18] C.E. Ordonez, A. Bolozdynya, and W. Chang. Doppler broadening of energy spectra in compton cameras. In *Nuclear Science Symposium, 1997. IEEE*, volume 2, pages 1361 –1365 vol.2, nov 1997. doi: 10.1109/NSSMIC.1997.670574.

[19] F. Biggs, L.B. Mendelsohn, and J.B. Mann. Hartree-Fock compton profiles for the elements. *Atomic Data and Nuclear Data Tables*, 16(3):201 – 309, 1975. ISSN 0092-640X. doi: http://dx.doi.org/10.1016/0092-640X(75)90030-3. URL http://www.sciencedirect.com/science/article/pii/0092640X75900303.

[20] Y.F. Du, Z. He, G.F. Knoll, D.K. Wehe, and W. Li. Evaluation of a compton scattering camera using 3-D position sensitive CdZnTe detectors. *Nuclear Instruments and Methods in Physics Research Section A: Accelerators, Spectrometers, Detectors and Associated Equipment*, 457(1-2):p. 203–211, 2001. ISSN 0168-9002. doi: 10.1016/S0168-9002(00)00669-0.

[21] A. Poitrasson-Riviere, M.C. Hamel, K. Ide, J.K. Polack, K.L. McMillan, S.D. Clarke, M. Flaska, S.A. Pozzi, G. Pausch, C.-M. Herbach, M. Ohmes, and J. Stein. Large-scale compton-camera simulations, validation experiments, and image reconstruction. In *Nuclear Science Symposium and Medical Imaging Conference (NSS/MIC), 2011 IEEE*, pages 212–215, 2011. doi: 10.1109/NSSMIC.2011.6154482.

[22] V. Schoenfelder et al. Instrument description and performance of the Imaging Gamma-Ray Telescope COMPTEL aboard the Compton Gamma-Ray Observatory. *Astrophysical Journal Supplement Series*, 86:657–692, June 1993. doi: 10.1086/191794.

[23] V. Schonfelder, R. Diehl, G.G. Lichti, H. Steinle, B. N. Swanenburg, A. J M Deerenberg, H. Aarts, J. Lockwood, W. Webber, J. Macri, J. Ryan, G. Simpson, B. G. Taylor, K. Bennett, and M. Snelling. The imaging compton telescope COMPTEL on the gamma ray observatory. *Nuclear Science, IEEE Transactions on*, 31(1): 766–770, 1984. ISSN 0018-9499. doi: 10.1109/TNS.1984.4333363.

[24] S. Takeda, H. Aono, S. Okuyama, S.-n. Ishikawa, H. Odaka, S. Watanabe, M. Kokubun, T. Takahashi, K. Nakazawa, H. Tajima, and N. Kawachi. Experimental results of the gamma-ray imaging capability with a Si/CdTe semiconductor compton camera. *Nuclear Science, IEEE Transactions on*, 56(3):783–790, June 2009. ISSN 0018-9499. doi: 10.1109/TNS.2008.2012059.

[25] Y.F. Yang, Y. Gono, S. Motomura, S. Enomoto, and Y. Yano. A compton camera for multitracer imaging. *Nuclear Science, IEEE Transactions on*, 48(3):656 –661, jun 2001. ISSN 0018-9499. doi: 10.1109/23.940142.

[26] M.-H. Richard, M. Chevallier, D. Dauvergne, N. Freud, P. Henriquet, F. Le Foulher, J.-M. Letang, G. Montarou, C. Ray, F. Roellinghoff, E. Testa, M. Testa, and A. H. Walenta. Design guidelines for a double scattering compton camera for prompt-γ imaging during ion beam therapy: A monte carlo simulation study. *Nuclear Science, IEEE Transactions on*, 58(1):87–94, 2011. ISSN 0018-9499. doi: 10.1109/TNS.2010.2076303.

[27] G Ariño, M Chmeissani, G De Lorenzo, C Puigdengoles, E Cabruja, Y Calderón, M Kolstein, J G Macias-Montero, R Martinez, E Mikhaylova, and D Uzun. Energy and coincidence time resolution measurements of CdTe detectors for PET. *Journal of Instrumentation*, 8(02):C02015, 2013. URL http://stacks.iop.org/1748-0221/8/i=02/a=C02015.

[28] Stephan Berko and Frank L. Hereford. Experimental studies of positron interactions in solids and liquids. *Rev. Mod. Phys.*, 28:299–307, Jul 1956. doi: 10.1103/RevModPhys.28.299. URL http://link.aps.org/doi/10.1103/RevModPhys.28.299.

[29] C. S. Levin and E. J. Hoffman. Calculation of positron range and its effect on the fundamental limit of positron emission tomography system spatial resolution. *Phys Med Biol*, 44(3):781–799, Mar 1999.

[30] S. DeBenedetti, C. E. Cowan, W. R. Konneker, and H. Primakoff. On the angular distribution of two-photon annihilation radiation. *Phys. Rev.*, 77:205–212, Jan 1950. doi: 10.1103/PhysRev.77.205. URL http://link.aps.org/doi/10.1103/PhysRev.77.205.

[31] D. L. Bailey, D. W. Townsed, P. E. Walk, and M. N. Maisey. *Positron Emission Tomography: Basic Sciences*. London: Springer-Verlag Limited, 2005.

[32] E. Mikhaylova, G. De Lorenzo, M. Chmeissani, M. Kolstein, M. Canadas, P. Arce, Y. Calderon, D. Uzun, G. Arino, and J. Macias-Montero. Simulation of the expected performance of a seamless scanner for brain PET based on highly pixelated CdTe detectors. *Medical Imaging, IEEE Transactions on*, PP(99):1–1, 2013. ISSN 0278-0062. doi: 10.1109/TMI.2013.2284657.

[33] M. Kolstein, G. De Lorenzo, E. Mikhaylova, M. Chmeissani, G. Ariño, Y. Calderón, I. Ozsahin, and D. Uzun. Evaluation of origin ensemble algorithm for image reconstruction for pixelated solid-state detectors with large number of channels.

Journal of Instrumentation, 8(04):P04030, 2013. URL http://stacks.iop.org/1748-0221/8/i=04/a=P04030.

[34] E. Mikhaylova et al. Simulation of pseudo-clinical conditions and image quality evaluation of PET scanner based on pixelated CdTe detector. In *Nuclear Science Symposium and Medical Imaging Conference (NSS/MIC), 2011 IEEE*, pages 2716 –2722, oct. 2011. doi: 10.1109/NSSMIC.2011.6152955.

[35] G De Lorenzo, M Chmeissani, D Uzun, M Kolstein, I Ozsahin, E Mikhaylova, P Arce, M Cañadas, G Ariño, and Y Calderón. Pixelated CdTe detectors to overcome intrinsic limitations of crystal based positron emission mammographs. *Journal of Instrumentation*, 8(01):C01030, 2013. URL http://stacks.iop.org/1748-0221/8/i=01/a=C01030.

[36] J.-G. Macias-Montero, M. Sarraj, M. Chmeissani, C. Puigdengoles, G. De Lorenzo, and R. Martinez. Toward VIP-PIX: A low noise readout ASIC for pixelated CdTe gamma-ray detectors for use in the next generation of PET scanners. *Nuclear Science, IEEE Transactions on*, 60(4):2898–2904, 2013. ISSN 0018-9499. doi: 10.1109/TNS.2013.2270115.

[37] L. Abbene, G. Gerardi, F. Principato, A. A. Turturici, S. Del Sordo, and G. Raso. Characterization of Al-Schottky CdTe detectors. In *Nuclear Science Symposium and Medical Imaging Conference (NSS/MIC), 2011 IEEE*, pages 4636–4641, Oct 2011. doi: 10.1109/NSSMIC.2011.6154749.

[38] G. Arino et al. Characterization of CdTe detector for use in PET. In *Nuclear Science Symposium and Medical Imaging Conference (NSS/MIC), 2011 IEEE*, pages 4598 –4603, oct. 2011. doi: 10.1109/NSSMIC.2011.6154742.

[39] S. Agostinelli et al. Geant4—a simulation toolkit. *Nuclear Instruments and Methods in Physics Research Section A: Accelerators, Spectrometers, Detectors and Associated Equipment*, 506(3):250 – 303, 2003. ISSN 0168-9002. doi: http://dx.doi.org/10.1016/S0168-9002(03)01368-8. URL http://www.sciencedirect.com/science/article/pii/S0168900203013688.

[40] S. Abdoulline et al. The CMS simulation software. In *Nuclear Science Symposium Conference Record, 2006. IEEE*, volume 3, pages 1655–1659, 2006. doi: 10.1109/NSSMIC.2006.354216.

[41] P. Arce et al. Simulation framework and XML detector description for the CMS experiment. *Nuclear Instruments and Methods in Physics Research Section A: Accelerators, Spectrometers, Detectors and Associated Equipment*, 502(2–3):687 – 688, 2003. ISSN 0168-9002. doi: http://dx.doi.org/10.

1016/S0168-9002(03)00544-8. URL http://www.sciencedirect.com/science/article/pii/S0168900203005448. Proceedings of the VIII International Workshop on Advanced Computing and Analysis Techniques in Physics Research.

[42] D. Costanzo, A. Dell'Acqua, M. Gallas, A. Rimoldi, J. Boudreau, V. Tsulaia, and A. Di Simone. The Geant4-based simulation software of the ATLAS detector. In *Nuclear Science Symposium Conference Record, 2006. IEEE*, volume 1, pages 5–11, 2006. doi: 10.1109/NSSMIC.2006.356099.

[43] G. Corti, Cattaneo, et al. Software for the LHCb experiment. In *Nuclear Science Symposium Conference Record, 2004 IEEE*, volume 4, pages 2048–2052 Vol. 4, 2004. doi: 10.1109/NSSMIC.2004.1462666.

[44] F. Lei, P.R. Truscott, C.S. Dyer, B. Quaghebeur, D. Heynderickx, P. Nieminen, H. Evans, and E. Daly. Mulassis: a Geant4-based multilayered shielding simulation tool. *Nuclear Science, IEEE Transactions on*, 49(6):2788–2793, 2002. ISSN 0018-9499. doi: 10.1109/TNS.2002.805351.

[45] G. Santin, V. Ivanchenko, H. Evans, P. Nieminen, and E. Daly. GRAS: a general-purpose 3-D modular simulation tool for space environment effects analysis. *Nuclear Science, IEEE Transactions on*, 52(6):2294–2299, 2005. ISSN 0018-9499. doi: 10.1109/TNS.2005.860749.

[46] G. Santin, D. Strul, D. Lazaro, L. Simon, M. Krieguer, M. Vieira Martins, V. Breton, and C. Morel. GATE, a geant4-based simulation platform for PET integrating movement and time management. In *Nuclear Science Symposium Conference Record, 2002 IEEE*, volume 2, pages 1325–1329 vol.2, 2002. doi: 10.1109/NSSMIC.2002.1239563.

[47] Pedro Arce, Juan Ignacio Lagares, Laura Harkness, Daniel Pérez-Astudillo, Mario Cañadas, Pedro Rato, María de Prado, Yamiel Abreu, Gianluca de Lorenzo, Machiel Kolstein, and Angelina Díaz. GAMOS: A framework to do geant4 simulations in different physics fields with an user-friendly interface. *Nuclear Instruments and Methods in Physics Research Section A: Accelerators, Spectrometers, Detectors and Associated Equipment*, 2013. ISSN 0168-9002. doi: http://dx.doi.org/10.1016/j.nima.2013.09.036. URL http://www.sciencedirect.com/science/article/pii/S0168900213012709.

[48] V. Ivanchenko et al. Recent improvements in geant4 electromagnetic physics models and interfaces. *Progress in NUCLEAR SCIENCE and TECHNOLOGY*, 2:898–903, 2011.

[49] H. Burkhardt, V.M. Grichine, P. Gumplinger, V.N. Ivanchenko, R. P. Kokoulin, M. Maire, and L. Urban. Geant4 standard electromagnetic package for HEP applications. In *Nuclear Science Symposium Conference Record, 2004 IEEE*, volume 3, pages 1907–1910 Vol. 3, 2004. doi: 10.1109/NSSMIC.2004.1462617.

[50] J. Apostolakis et al. The performance of the Geant4 standard EM package for LHC and other applications. *Journal of Physics: Conference Series*, 119(3):032004, 2008. URL http://stacks.iop.org/1742-6596/119/i=3/a=032004.

[51] S.T. Perkins et al. Tables and graphs of electron-interaction cross sections from 10 ev to 100 gev derived from the LLNL evaluated electron data library (EEDL), Z=1-100. *UCRL-50400*, 31, 1997.

[52] D. Cullen et al. EPDL97, the evaluated photon data library, 97 version. *UCRL-50400*, 6(Rev. 5), 1997.

[53] Rene Brun and Fons Rademakers. ROOT — an object oriented data analysis framework. *Nuclear Instruments and Methods in Physics Research Section A: Accelerators, Spectrometers, Detectors and Associated Equipment*, 389(1–2):81 – 86, 1997. ISSN 0168-9002. doi: http://dx.doi.org/10.1016/S0168-9002(97)00048-X. URL http://www.sciencedirect.com/science/article/pii/S016890029700048X. ¡ce:title¿New Computing Techniques in Physics Research V¡/ce:title¿.

[54] D.H. Wilkinson. *Ionization Chambers and Counters*. New York: Cambridge Univ. Press, 1950.

[55] W. Shockley. Currents to conductors induced by a moving point charge. *Journal of Applied Physics*, 9(10):635–636, 1938. doi: http://dx.doi.org/10.1063/1.1710367. URL http://scitation.aip.org/content/aip/journal/jap/9/10/10.1063/1.1710367.

[56] S. Ramo. Currents induced by electron motion. *Proceedings of the IRE*, 27(9): 584–585, 1939. ISSN 0096-8390. doi: 10.1109/JRPROC.1939.228757.

[57] E. Whittaker and G. Robinson. *The Calculus of Observations: A Treatise on Numerical Mathematics*. Dover Publications, 4th edition, 1967.

[58] S.J. Wilderman, W.L. Rogers, G.F. Knoll, and J.C. Engdahl. Fast algorithm for list mode back-projection of compton scatter camera data. In *Nuclear Science Symposium, 1997. IEEE*, pages 391–395 vol.1, 1997. doi: 10.1109/NSSMIC.1997.672609.

[59] M.J. Cree and P.J. Bones. Towards direct reconstruction from a gamma camera based on compton scattering. *Medical Imaging, IEEE Transactions on*, 13(2):398–407, 1994. ISSN 0278-0062. doi: 10.1109/42.293932.

[60] R. Basko, G.L. Zeng, and G.T. Gullberg. Application of spherical harmonics to image reconstruction for the compton camera. *Physics in Medicine and Biology*, 43 (4):887, 1998. URL http://stacks.iop.org/0031-9155/43/i=4/a=016.

[61] L.C. Parra. Reconstruction of cone-beam projections from compton scattered data. *Nuclear Science, IEEE Transactions on*, 47(4):1543–1550, 2000. ISSN 0018-9499. doi: 10.1109/23.873014.

[62] S Kaczmarz. Angenäherte auflösung von systemen linearer gleichungen. *Bulletin International de l'Académie Polonaise des Sciences et des Lettres. Classe des Sciences Mathématiques et Naturelles. Série A, Sciences Mathématique.*, 35:355–357, 1937.

[63] R. Gordon, R. Bender, and G. T. Herman. Algebraic reconstruction techniques (ART) for three-dimensional electron microscopy and x-ray photography. *Journal of Theoretical Biology*, 29(3):471 – 481, 1970. ISSN 0022-5193. doi: http://dx.doi.org/10.1016/0022-5193(70)90109-8. URL http://www.sciencedirect.com/science/article/pii/0022519370901098.

[64] A Sitek. Representation of photon limited data in emission tomography using origin ensembles. *Physics in Medicine and Biology*, 53(12):3201, 2008. URL http://stacks.iop.org/0031-9155/53/i=12/a=009.

[65] A. Andreyev, A. Sitek, and A. Celler. Stochastic image reconstruction method for compton camera. In *Nuclear Science Symposium Conference Record (NSS/MIC), 2009 IEEE*, pages 2985 –2988, 24 2009-nov. 1 2009. doi: 10.1109/NSSMIC.2009.5401592.

[66] A. Andreyev, A. Celler, and A. Sitek. Resolution recovery for compton camera using origin ensemble algorithm. In *Nuclear Science Symposium and Medical Imaging Conference (NSS/MIC), 2011 IEEE*, pages 2774–2778, 2011. doi: 10.1109/NSSMIC.2011.6153638.

[67] E. Mikhaylova, M. Kolstein, G. De Lorenzo, and M. Chmeissani. Optimization, evaluation, and comparison of standard algorithms for image reconstruction with the VIP-PET. *JINST, IWORID conf. record (2013) To be published.*, 2013.

[68] Y. Calderon et al. Modeling, simulation, and evaluation of a compton camera based on a pixelated solid-state detector. In *Nuclear Science Symposium and Medical*

Imaging Conference (NSS/MIC), 2011 IEEE, pages 2708 –2715, oct. 2011. doi: 10.1109/NSSMIC.2011.6152954.

[69] A. P. Dempster, N. M. Laird, and D. B. Rubin. Maximum likelihood from incomplete data via the em algorithm. *Journal of the Royal Statistical Society. Series B (Methodological)*, 39(1):pp. 1–38, 1977. ISSN 00359246. URL http://www.jstor.org/stable/2984875.

[70] L.A. Shepp and Y. Vardi. Maximum likelihood reconstruction for emission tomography. *Medical Imaging, IEEE Transactions on*, 1(2):113–122, 1982. ISSN 0278-0062. doi: 10.1109/TMI.1982.4307558.

[71] S.J. Wilderman, J.A. Fessler, N.H. Clinthorne, J.W. LeBlanc, and W.L. Rogers. Improved modeling of system response in list mode EM reconstruction of compton scatter camera images. *Nuclear Science, IEEE Transactions on*, 48(1):111–116, 2001. ISSN 0018-9499. doi: 10.1109/23.910840.

[72] H.M. Hudson and R.S. Larkin. Accelerated image reconstruction using ordered subsets of projection data. *Medical Imaging, IEEE Transactions on*, 13(4):601–609, 1994. ISSN 0278-0062. doi: 10.1109/42.363108.

[73] H.H. Barret, L.C. Parra, and T. White. List-mode likelihood. *J. Opt. Soc. Am.*, 14 (11):2914–2923, 1997.

[74] L. Parra and H.H. Barrett. List-mode likelihood: EM algorithm and image quality estimation demonstrated on 2-d PET. *Medical Imaging, IEEE Transactions on*, 17 (2):228–235, 1998. ISSN 0278-0062. doi: 10.1109/42.700734.

[75] S.J. Wilderman, N.H. Clinthorne, J.A. Fessler, and W.L. Rogers. List-mode maximum likelihood reconstruction of compton scatter camera images in nuclear medicine. In *Nuclear Science Symposium, 1998. Conference Record. 1998 IEEE*, volume 3, pages 1716–1720 vol.3, 1998. doi: 10.1109/NSSMIC.1998.773871.

[76] D. Uzun, M. Kolstein, G. De Lorenzo, and M. Chmeissani. Evaluation of a dedicated LM-OSEM algorithm for the reconstruction of images with the VIP-PEM system. *JINST, IWORID conf. record (2013) To be published.*, 2013.

[77] M. Kolstein, G. De Lorenzo, and M. Chmeissani. Evaluation of list-mode ordered subset expectation maximization image reconstruction for pixelated solid-state compton gamma camera with large number of channels. *JINST, IWORID conf. record (2013) To be published.*, 2013.

[78] NEMA standards publication NU 4-2008: Performance measurements for small animal positron emission tomographs. *Rosslyn, VA: National Electrical Manufaturers (2008)*, 2008.

[79] NEMA standards publication NU 4-2008: Performance measurements of gamma cameras. *Rosslyn, VA: National Electrical Manufaturers (2007)*, 2007.

[80] Andreas Zoglauer and Steven E. Boggs. Application of neural networks to the identification of the compton interaction sequence in compton imagers. In *Nuclear Science Symposium Conference Record, 2007. NSS '07. IEEE*, volume 6, pages 4436–4441, 2007. doi: 10.1109/NSSMIC.2007.4437096.

[81] C. X. Wang, W. E. Snyder, G. Bilbro, and P. Santago. Performance evaluation of filtered backprojection reconstruction and iterative reconstruction methods for PET images. *Comput. Biol. Med.*, 28(1):13–24, Jan 1998.

[82] Y. Calderón, M. Chmeissani, M. Kolstein, and G. De Lorenzo. Evaluation of compton gamma camera prototype based on pixelated CdTe detectors. *Journal of Instrumentation*, To be published in 2014.

[83] G. Ariño, G. De Lorenzo, and M. Chmeissani. Characterization of a module with pixelated CdTe detectors for possible PET, PEM and Compton camera applications. *JINST, IWORID conf. record (2013) To be published.*, 2013.